5. FUSION POWER CORE

Dai-Kai Sze
Laila A. El-Guebaly
Igor N. Sviatoslavsky
Xueren Wang

Contents

5. FUSION POWER CORE

5.1. INTRODUCTION

The performance and the safety characteristics of a power plant are usually determined by the selection of the structural material. This material has to be able to withstand high temperatures and resist severe radiation damage. After the structural material has been selected, other materials, such as breeding material and/or coolant, can be selected to be compatible with the structural material. The selection of the structural material has to take the following requirements into consideration: (1) High temperature capability, (2) High radiation damage resistance, (3) High heat flux capability, (4) Low near-term and long-term activation, (4) Low after heat, (5) Low unit cost, and (6) Ease of fabrication.

It can be seen that no structural material can fulfill all those requirements. Thus, the selection of the structural material is usually a compromise procedure trying to satisfy as many requirements as possible. Table 5.1-I outlines a comparison of the three possible candidates of the structural materials. The three materials selected are ferritic steels, V-alloy, and SiC composite. The score is from 1 to 3, with 3 being the best and 1 being the worst. The total score will indicate the attractiveness of each material for the fusion applications. The total score of V-alloy is 19, which is much higher than that of either SiC or ferritic steels. Thus, it is reasonable to select V-alloy as the structural material.

After V-alloy is selected as the structural material, the selection of the coolant and breeding material follows. One of the key issues associated with using V-alloy is that it is reactive to both hydrogen and oxygen. Lithium is one of the few materials which has an even stronger affinity for both hydrogen and oxygen than vanadium. Thus, if lithium is in contact with V-alloy, both hydrogen and oxygen will be preferentially dissolved in the lithium. This resolves a key problem associated with using V-alloy. Also, lithium has the following unique characteristics: (1) Low activation, (2) High temperature capability, (3) Good heat transfer characteristics, (4) Good tritium sink (tritium control is not an issue), (5) Low density.

In selecting lithium as the coolant and breeding material, the following concerns have to be resolved: (1) Lithium is chemically reactive with air, water, CO_2, concrete, *etc.* Thus, the design must prevent any potential lithium accident. (2) Lithium is an electric

Table 5.1-I.
Structural Material Compositions

	Ferritic steels	V-Alloy	SiC composite
High temperature capability	1	2	3
High radiation damage resistance	2	3	1[(a)]
High heat flux capability	1.5	3	1.5
Low near term activation	1	2	3
Low long term activation	1	3	2
Low after heat	1	2	3
Low unit cost	3	2	1
Ease of fabrication	3	2	1
Total score	13.5	19	15.5

(*a*) Almost no data on radiation damage on SiC composite.

conductor. Thus, the follow of lithium across the magnetic field will result in large MHD pressure drop. Any design has to take this MHD pressure drop into consideration. (3) Lithium is a good tritium sink. Thus tritium recovery from lithium is a concern. (4) Lithium can be corrosive to certain structural materials, such as SiC or stainless steel. However, the compatibility between lithium and V-alloy is not a major concern.

To reduce the MHD pressure drop, an insulating coating is required. This insulating coating has to be compatible with lithium at high temperatures, resistive to radiation damage and thermal cycling, and compatible to tritium recovery processes. It also has to be reliable over many years of operation. The most promising material for the insulating coating is CaO. The development of the insulating coating is still in an early stage, and many issues have to be resolved. The design of the fusion core, including MHD considerations, heat transfer, power conversion, and tritium recovery systems are discussed in Sec. 5.2.

Lithium is not a good shielding material, therefore, another material is required to provide this function. While V-alloy is acceptable for the shielding function, the cost of the V-alloy is high, and the volume of material required for shielding is large. Thus, it is not economically feasible to use V-alloy for shielding purposes. A low activation ferritic steel called tenelon was selected as the shielding material due to its good neutronics properties and low cost. The tenelon is inside a vanadium container and is not directly in contact with lithium. Also, the tenelon does not provide structural function. Thus, tenelon can operate at a temperature higher than that for structural purposes. The use of tenelon and its neutronics importance will be discussed in Section 5.3. The complicated geometry of stellarator fusion core, makes configuration and maintenance of the fusion core an essential element of the design (Sec. 5.4).

5.2. POWER CORE DESIGN

5.2.1. Configuration

For the SPPS power plant, a liquid metal blanket with electrically insulated coating on the walls is selected as the reference design. Such a choice is consistent with the philosophy of SPPS of opting for the most favorable yet creditable option available. The use of the insulating coating has major impacts on the configuration. It allows one to develop a very attractive first wall and blanket design by addressing mechanical, thermal hydraulic, and neutronics requirements in the most direct and simple way rather than by trying to minimize MHD pressure drop effects by utilizing more complex flow configurations. Even with an insulated wall, MHD effects associated with turbulence suppression on heat transfer are still present. Therefore, proper care must be taken when the configuration is defined to avoid configurations which create stagnation flow regions near high heat flux surfaces, negate the effect of the insulating coating by providing current closure paths through the liquid metal, or result in poor flow distribution. This can be done without compromising the simplicity or the performance of the blanket.

In choosing an insulated wall concept as the reference design, a number of challenging MHD-related issues are eliminated. On the other hand, the credibility of this design is based entirely on the integrity of the insulating coating in the blanket environment. Several candidate ceramic insulators [1–3] possess the necessary resistivities to satisfy the electrical insulating requirements. The primary candidate at this time is CaO [4]. The development of insulating coating is in the early stage. Therefore, the choice of the insulating coating material may change as new materials will be tested, and technical problems will be uncovered as the testing progresses.

The proposed design has an integrated first wall and blanket. The front part of the shield, which has a shorter life time than the design life of the power plant, is also an integrated part of the first wall and blanket. The back part of the shield is designed to be a permanent component. A blanket module is shown schematically in Fig. 5.2-1.

Coolant is brought into the blanket module assembly through the magnet coils by one 25-cm and one 20-cm diameter pipes at the bottom of the assembly. The 25-cm pipe empties into the first-wall/blanket manifold and the 20-cm pipe empties into the shield manifold. The tow manifolds, which have a combined cross section of 50 cm x 50 cm, extend along the entire toroidal length of the assembly. Coolant ducts emanate from the manifolds, run along the poloidal direction, and empty into identical manifolds

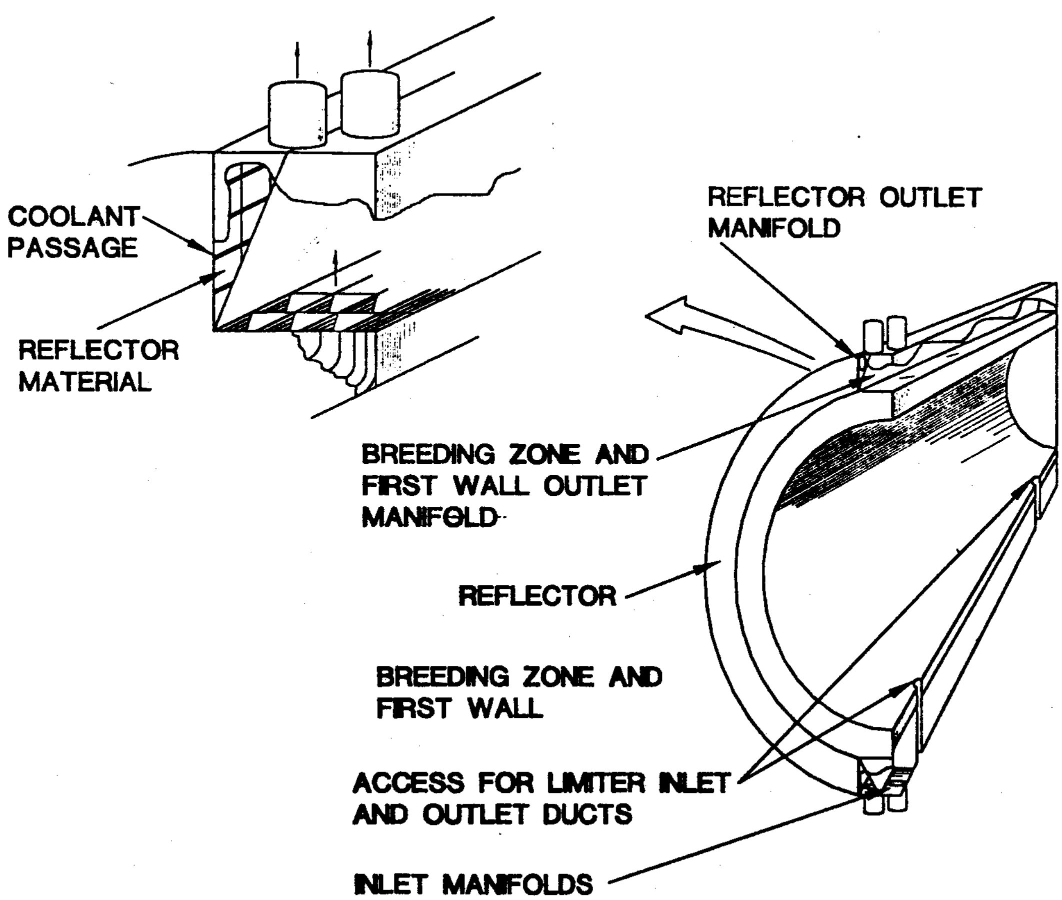

Figure 5.2-1. Blanket assembly for SPPS power plant.

symmetrically located at the top half of the assembly. Outlet pipes identical to the inlet pipes take the coolant out of the power plant.

Figure 5.2-2 shows a section of the blanket by a horizontal mid-plane of the torus. The first wall coolant channels are rectangular ducts with a 10-mm × 50-mm cross section. The first wall should be smooth both for ease of fabrication and because it has some MHD related advantages. The disadvantage of a flat wall is the fact that the maximum material stress is bending stress, which is usually considerably higher than a corresponding hoop stress. This limits either the maximum allowable coolant pressure, or the duct dimension along the toroidal direction. The first wall thickness of 2 mm is a compromise between lower thermal stress and lower bending stress. The 2 mm given here does not include any sacrificial layer required for erosion protection.

The radial direction of the first wall coolant channel must be made as small as possible because the high coolant velocity required at the first wall coolant channel must be made as small as possible. This is due to the fact that the high coolant velocity required at the first wall coolant channel results in lower average exit coolant temperature, unless the

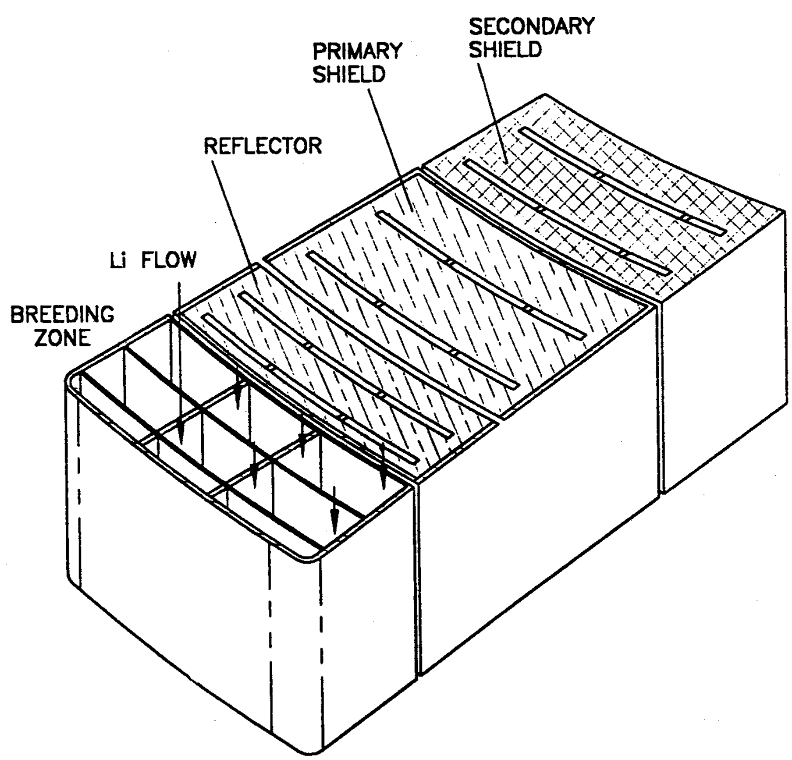

Figure 5.2-2. Cross-sectioned view of SPPS blanket.

radial dimension is made sufficiently small. Here, a dimension of 10 mm was thought to be a reasonable compromise between this requirement and the virtual elimination of any possibility of the first wall coolant channel plugging.

The coolant velocity in the blanket has to be carefully controlled. The design velocity in the reeding zone will decrease as the distance from the first wall increases. This is because the nuclear heat deposition rate reduces as the distance from the first wall increases. This is also to make the coolant exit temperature from all the coolant channel uniform, thus maximizing average coolant exit temperature and thermodynamic efficiency. The tailoring of the velocity to the local deposition rate can be accomplished with ducts whose radial dimension increases with distance from the first wall. If additional flow control is required, an orifice can be build into the loop to control the coolant flow. This "orifice" can be based on effects. A possible design is to insert a short metal inner sleeve at the inlet manifold/coolant duct junction. The wall thickness and the length of those inserts are adjusted to add different MHD pressure drops along the different parallel coolant paths.

With the configuration described here, the MHD, neutronics, and heat transfer calculations can be proceeded.

5.2.2. MHD Considerations

For a self-cooled liquid metal blanket for a Tokamak, a key design consideration, and often a design constraint, is the magnetohydrodynamic (MHD) pressure drop. Allowable blanket pressure is determined by the acceptable mechanical stress on the first wall, and/or other blanket structural components. The factors determining the MHD pressure drop include flow velocity, duct dimension, duct wall thickness, magnetic field strength, coolant flow path length, and the electrical conductivities of the liquid metal and the structural material. This MHD pressure drop is proportional to the wall thickness. Thus, increasing the wall thickness to withstand the high blanket pressure will increase the blanket pressure further. Therefore, it is very possible that the design of a self-cooled liquid metal blanket will not have an acceptable design window, with a condition consistent with the physics requirements [3].

To reduce the MHD pressure drop, one possible design approach is to disrupt the conducting path of the eddy current within the structural wall. Either a laminated wall with a thin wall facing the liquid metal flow, or an insulated coating, can enlarge the space of the design window. A design with an insulating coating will reduce the MHD pressure drop by a few orders of magnitude, while the laminated wall design will only reduce the MHD pressure drop by a factor of a few. Thus, a design with an insulated wall will be much more attractive. Therefore, the R/D effort follows [4]. In the US coating is developed which will be reliable within the blanket environment. This design, with an insulated wall, allows one to develop a very attractive first wall and blanket design by addressing mechanical, thermal hydraulic, and neutronics requirements in the most direct and simple way rather than trying to minimize adverse MHD pressure drop effects by utilizing more complex flow configurations.

To compare MHD pressure drop with a conducting wall and with an insulated wall, the following calculation clearly shows the big difference. For a conducting wall duct,

$$\frac{dp}{dx} = \frac{VB^2 t_w \sigma_w}{a}, \tag{5.2-1}$$

where V is the average velocity, B is the transverse magnetic field, t_w is the wall thickness, and σ_w is the wall electrical conductivity. For an insulated wall conduct,

$$\frac{dp}{dx} = \frac{\sigma V B^2}{M}, \tag{5.2-2}$$

where σ is the fluid electrical conductivity and $M = Ba(\sigma/\mu)^{1/2}$ is the Hartmann number.

Using the above expression with $a = 5$ cm, $t_w = 5$ mm, $B = 11$ T, $V = 1$ m/s, and $L = 1$ m (L is the flow path length), the pressure drops for a conducting wall case and insulated wall case are 12 MPa and 0.01 MPa, respectively. This calculation clearly shows the important effect of an insulated wall on the MHD pressure drop. Also, it shows the problem associated with MHD pressure drop with a conducting wall.

A feasible insulating coating must meet the following requirements: (1) Thermodynamically stable at the maximum blanket temperature, (2) Chemically compatible with lithium and the structural material, (3) Capable of fast in-situ self-healing, and (4) Sufficiently high electrical resistivity after irradiation.

Since all the insulator materials are not perfect insulators, and the electrical resistivity will increase after irradiation, it is important to evaluate the MHD pressure drop in a channel with a coating which has finite conductivity. The electrical insulation effectiveness of the coating depends both on the material properties and the design. The fully developed flow pressure gradient in a duct with insulator coating of uniform thickness t_c and be derived analytically is given by [5],

$$\frac{dp}{dx} = \frac{\sigma V B^2}{1 + \frac{\rho_c t_c M}{\rho_c t_c + 2b\rho M}} \tag{5.2-3}$$

where ρ_c is the electrical conductivity of the coating material, ρ is the electrical conductivity of the liquid metal, t_c is the coating thickness, $2b$ is the channel radial width, and M is the Hartmann number. Equation 5.2-3 shows that the key parameter is the ratio $(\rho_c t_c)/(2b\rho M)$. Figure 5.2-3 shows the dependence of pressure gradient on this parameter. Two dimensional numerical analysis of MHD flow in a rectangular duct [6] gives similar results. In general, $(\rho_c t_c)$ should be at least an order of magnitude higher than $(2b\rho M)$. For present design, the value of $\rho_c t_c > 0.001$.

There are a number of candidate materials which have the potential to be used as the insulating coating. If the coating thickness is 10 μm, the resistances of those materials are orders of magnitude higher than that required by fusion. Figure 5.2-4 shows the electrical resistance of some of the candidate materials, and the requirements for both ITER and commercial power plants. The leading candidate at this time is CaO. It can be seen that, at 600 °C, the resistance of the CaO coating is 7 orders of magnitude higher than that required by a commercial power plant. This provides a large margin to account for the degradation by the neutron irradiation.

Figure 5.2-5 shows the free energy of formation of CaO and Li_2O, with different oxygen concentration in lithium [7]. It can be seen that the CaO is much more stable than the Li_2O, with reasonable oxygen concentration inside lithium.

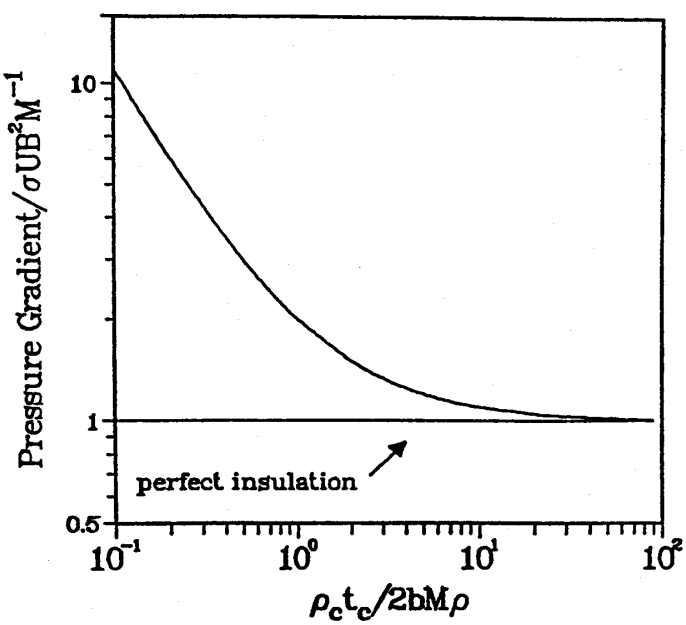

Figure 5.2-3. MHD Pressure drop for partially insulated wall.

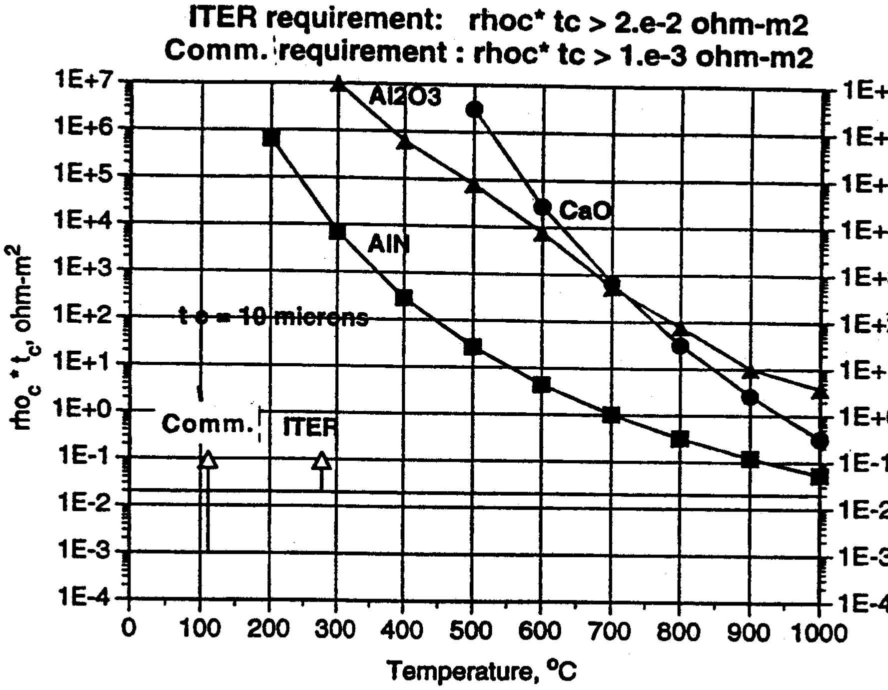

Figure 5.2-4. Resistance requirement for SPPS and ITER.

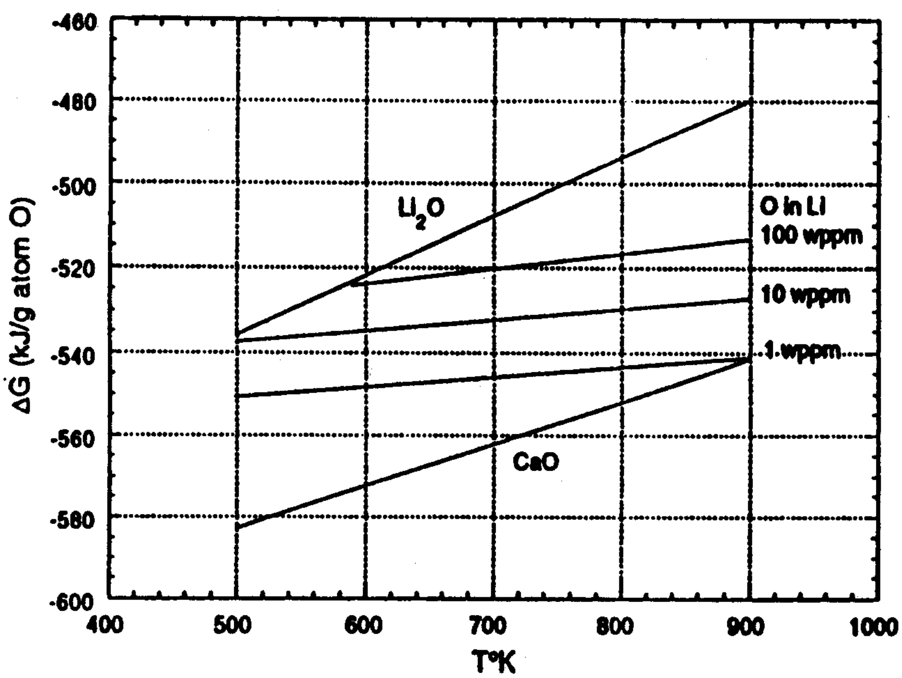

Figure 5.2-5. The standard free energy of formation of Li_2O and CaO compared with dilute solutions of oxygen in liquid lithium.

It is clear that the research of developing coating, and its impact to MHD pressure drop and flow distribution, is a critical R&D issue for a self-cooled liquid lithium blanket. The R&D effort on this subject is still in an early stage and many questions have to be answered. However, the purpose of this design study is to develop an attractive fusion core and then assess the R&D requirements to demonstrate this concept. Thus, a self-cooled lithium blanket with a CaO coating is selected as the reference design.

5.2.3. Heat Transfer

The heat transfer mechanism in a self-cooled liquid lithium blanket in a tokamak is dominated by conduction. Although the insulating coating reduces the MHD pressure drop, its impact on turbulence suppression is still sufficient to eliminate all turbulence. Although some recent development indicates that some form of turbulence can be initiated [8], its impact on heat transfer is not clear. If some turbulence does exist, the heat transfer mode here will get some more conservative results.

To do heat transfer calculations, a proper blanket configuration has to be defined. With this configuration and the heat and mass balance, the proper velocity distribution can be calculated. This velocity distribution, and the heat production rates, can then be used to calculate temperature distribution within the blanket. By assuming the maximum temperature in the blanket is the same as the maximum allowable temperature, the level of this temperature distribution can be adjusted to the proper level. This gives us the complete temperature profile of the blanket, as well as the entrance and exit coolant temperature, which will be used for power conversion system designs.

The blanket configuration has been described in Fig. 5.2-2 and the nuclear heating results will be discussed in Sec. 5.3. A three dimensional heat transfer code defines [9]) all the temperature in the blanket. The results of this calculation are summarized in Table 5.2-I.

5.2.4. Power Conversion

Fusion is capital intensive. Therefore, in order to reduce the cost of electricity (COE), an efficient power conversion is necessary. Also, fusion has rather high recirculation power fraction. This requires a high power conversion system to compensate for the additional power required for the plasma and magnets. For a Li/V design, a high coolant exit temperature is achievable. Therefore, a high efficiency power conversion system can be designed.

Table 5.2-I.
Thermal-hydraulic Parameters for the SPPS Power Plant

Total thermal power (MW)	2,292
Coolant inlet temperature (°C)	300
Coolant exit temperature (°C)	600
Maximum structure temperature (°C)	650
Average neutron wall loading (MW/m^2)	1.18
Average surface heat load (MW/m^2)	0.29
Coolant flow rate (m^3/s)	3.6
Coolant pressure drop (MPa)	1.4
Coolant pumping power (MW)	7
Gross thermal efficiency	46%
Total lithium volume (m^3)	600
Tritium inventory (g)	130

The limitation factor of the selection of the power conversion system is usually determined by the selection of the structural material. Based on the BCSS report [10], the maximum allowable temperature for vanadium alloy is ∼650–750 °C. With this temperature limit, the maximum achievable exit coolant temperature is about 600 °C. At this coolant temperature, the only power conversion system we may consider is an advance Rankine cycle.

The selection of a power conversion cycle is a compromise between performance and extrapolation of the existing technology. For the SPPS design, a sub-critical steam cycle, with two stage of reheat was selected. The parameters of this steam cycle are summarized in Table 5.2-II. The cycle efficiency is over 46% comparing to ∼35% for a PWR.

The schematic flow diagram of the temperature in the primary loop is shown in figure Fig. 5.2-6, and the detailed power cycle energy balance sheet is shown in Fig. 5.2-7.

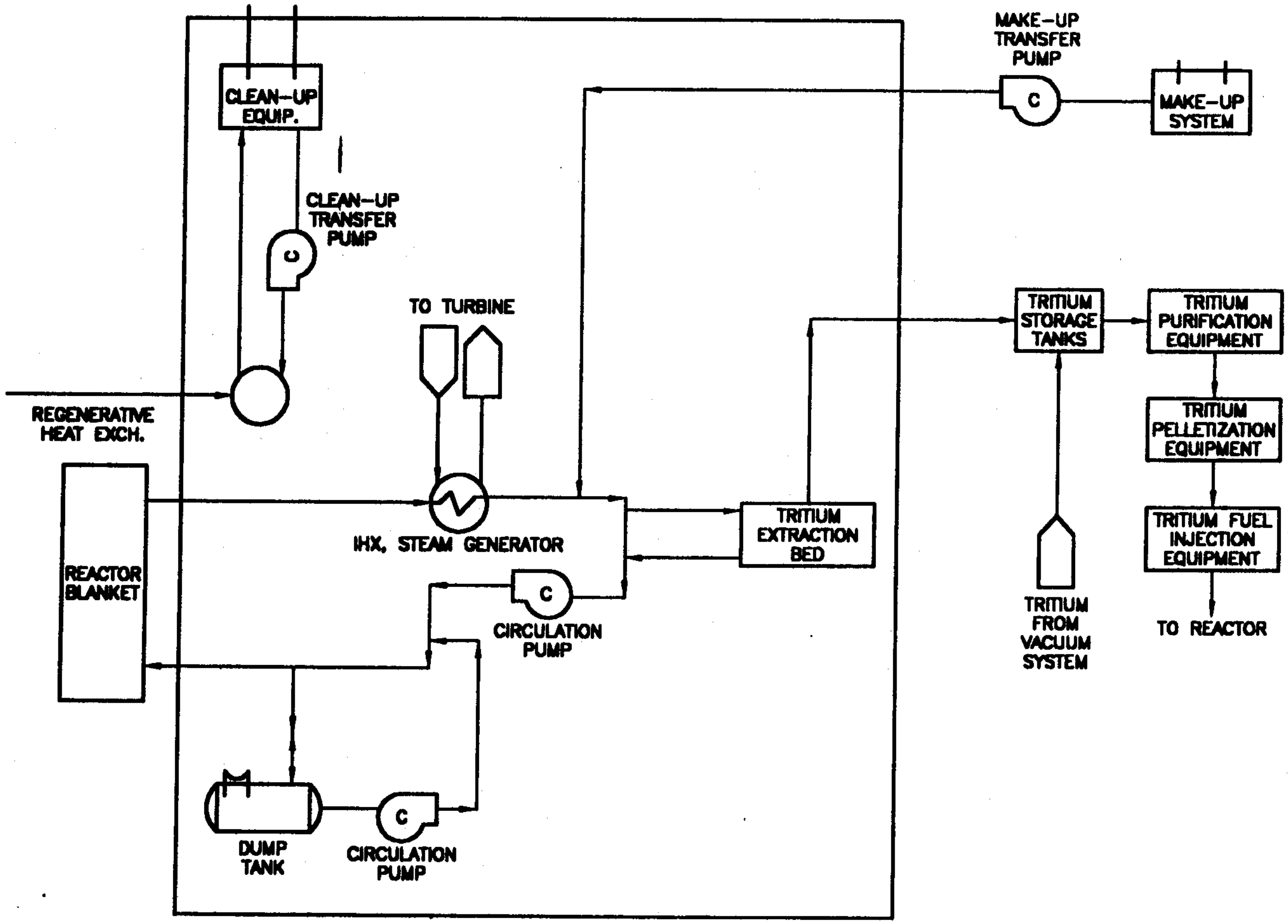

Figure 5.2-6. Primary coolant loop for the SPPS power plant.

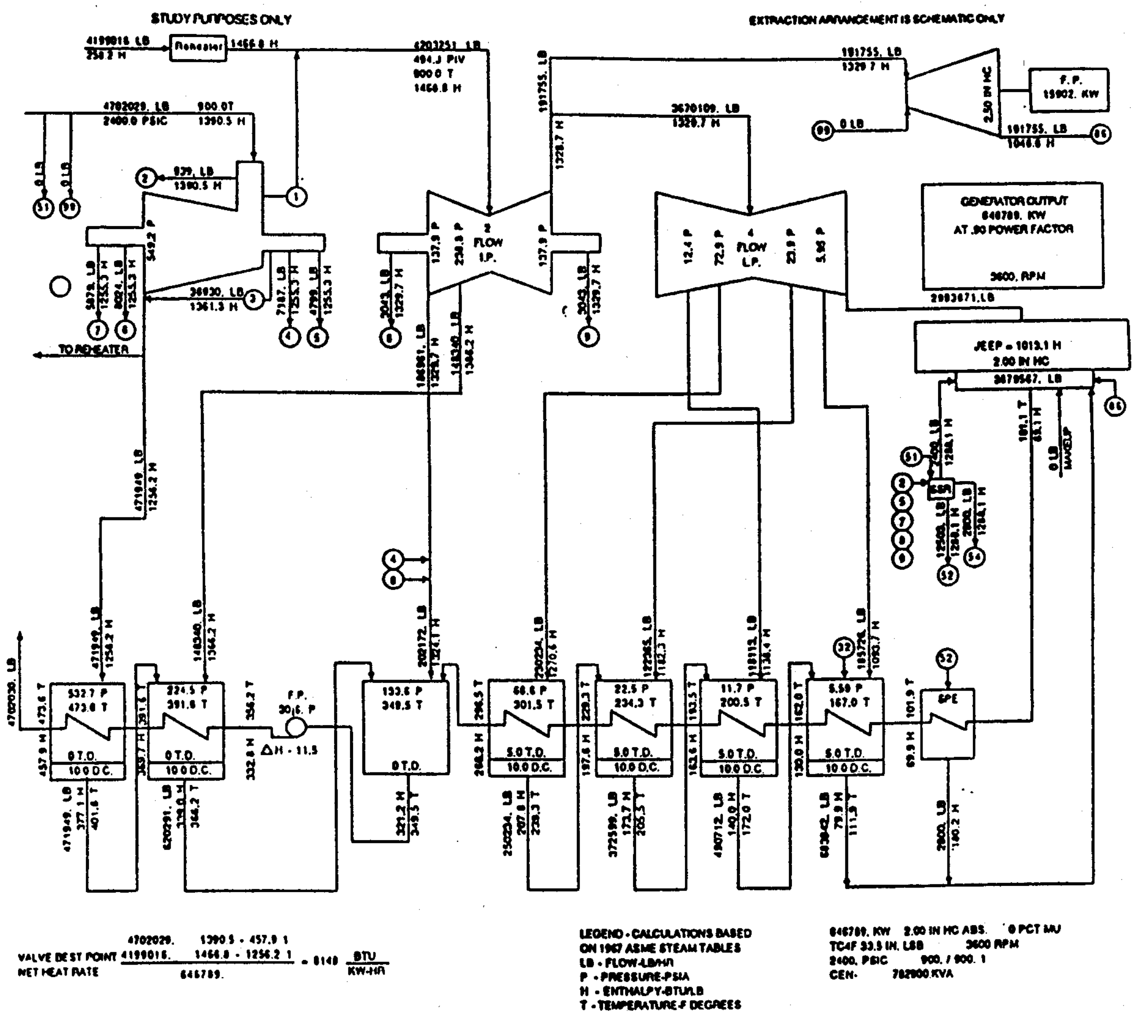

Figure 5.2-7. Turbine-generator cycle of the SPPS power plant.

Table 5.2-II.
Parameters of the SPPS Power Conversion System

Exit coolant temperature (°C)	610
Steam Temperature (°C)	566
Steam pressure (MPa)	31
Number of re-heat	2
Number of feed water heater	9
Cycle heating rate (kcal/kWh)	145
Cycle efficiency	46.6%

5.2.5. Tritium Recovery

Tritium recovery from lithium is a difficult technical issue. The key problem is that tritium has a very high solubility in lithium. The design goal is to reduce the tritium concentration in the lithium to ∼1 appm. This stringent design goal, and the high solubility, makes the recovery process very difficult. At 500 °C, and with a tritium concentration of 1 appm, the tritium partial pressure over lithium is only 10^{-10} torr. Thus, to recover tritium from vapor phase is almost impossible. The most logical way is to recover tritium from the liquid phase. Many different tritium recover processes have been proposed [11–13]. The only one which has demonstrated the possibility of recovery to the level of 1 appm is the molten salt recovery process [11]. However, in this process, lithium has to be mixed with a mixture of molten salts. This molten salt will be carried back to the blanket by the lithium. The potential problems associated with corrosion and the impact to the insulating coating are major concerns.

Recently, a cold trap process was developed by ITER design activities [14]. The concept is this process is to cool the lithium to ∼200 °C, and supersaturate the Li(H+T) in the lithium. A similar process was developed for the fast breeder applications to remove tritium from sodium. However, the hydrogen solubility in lithium is 440 appm at 200 °C, far higher than the design goal of 1 appm. This concept proposes to dissolve additional hydrogen into lithium to about 1,000 appm. Thus, although the tritium concentration is only 1 appm, the total hydrogen concentration would be more than 1,000 appm, and Li(H+T) becomes supersaturated. Thus, Li(H+T) will precipitate out. This concept is almost identical to that for the breeder program, which uses isotope effects to reduce the tritium partial pressure, while here we use the isotope effects to reduce the tritium concentration. Thus, the entire system was developed successfully for the fast breeder program, and there is a high degree of confidence this process will work as designed for fusion.

Figure 5.2-8 shows some early results for cold trap of hydrogen [15]. One can see that the cold trap concentration is almost identical to that of the saturation concentration. This result was used to reject cold trap as the tritium recovery process from lithium, because the concentration reachable is far higher than the design goal.

Figure 5.2-9 shows the cold trap process. As can be seen, protium is added to the lithium to a concentration of 1,300 appm. The lithium is than cooled to the cold trap temperature of 200 °C, at which time Li(H+T) will precipitate out. This Li(H+T) is heated up to 600 °C to decompose the Li(H+T) to Li and HT. A 200 °C cold trap is used to remove the lithium in the vapor phase caused by evaporation at 600 °C. After this, the hydrogen isotopes are fed to the isotope separation system to remove H from T.

Figure 5.2-10 shows the design of the Isotope Separation System (ISS) for ITER [16]. A careful ISS design study was made, and it was concluded that the addition protium in the blanket tritium stream has minor effects on both the tritium inventory in the ISS and the cryogenic power requirement.

5.3. BLANKET NEUTRONICS AND SHIELD DESIGN

5.3.1. Introduction

The neutronics activities for the SPPS study include the determination of the blanket dimensions that provide tritium self-sufficiency, radiation damage to the structural materials, lifetime of the in-vessel components, radiation level at the superconducting magnets, and shielding requirements for magnet protection. An essential input to the neutronics analysis is the neutron wall loading distribution. Section 5.3.2 presents the variation of the wall loading in both toroidal and poloidal directions for the nonuniform first wall shape of the SPPS design. The blanket is required to breed sufficient tritium to ensure the self-sustaining operation of the D-T fueled stellarator. The blanket utilizes the liquid lithium as a coolant and breeder and the low activation vanadium alloy V-5Cr-5Ti

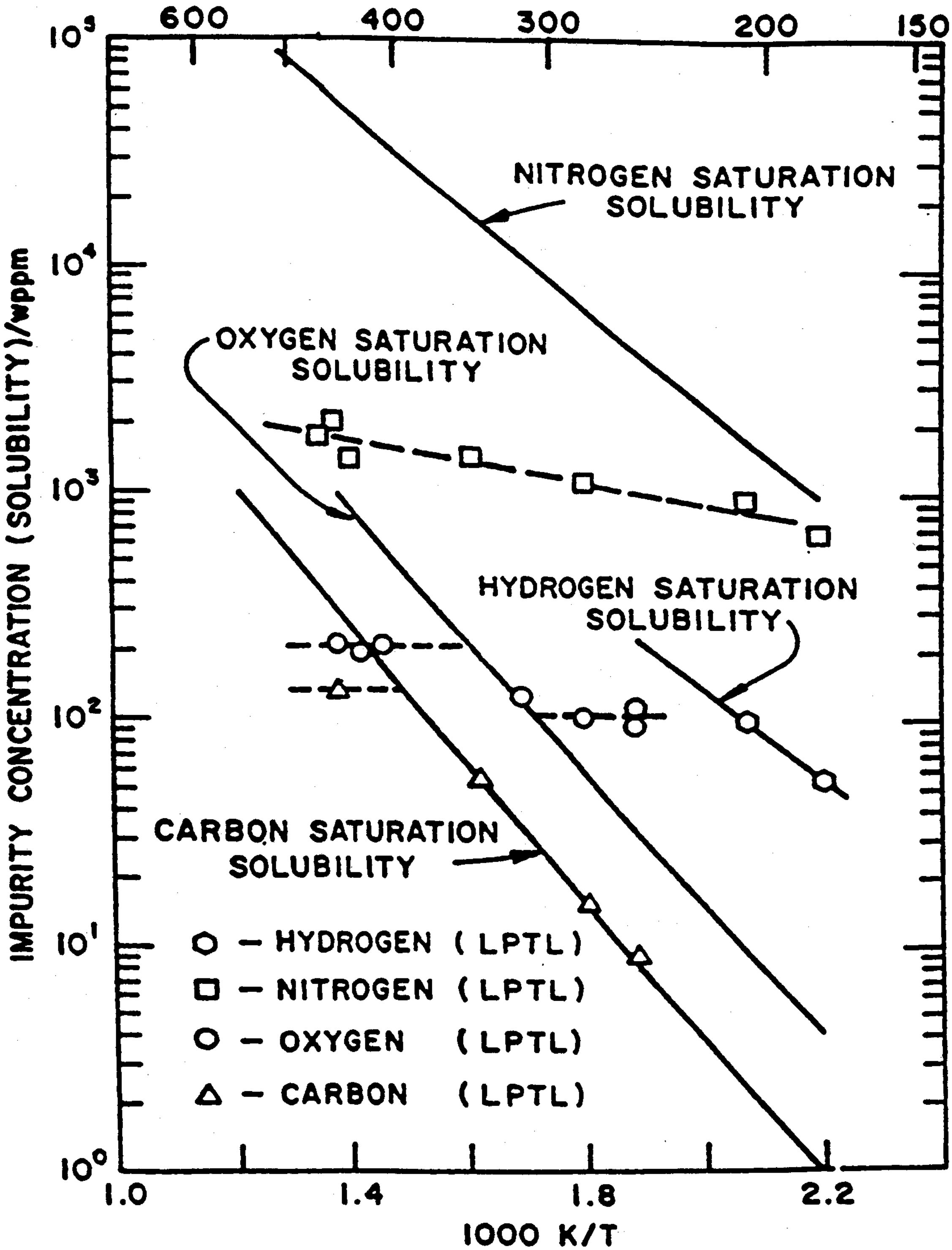

Figure 5.2-8. Cold trap of impurities from lithium.

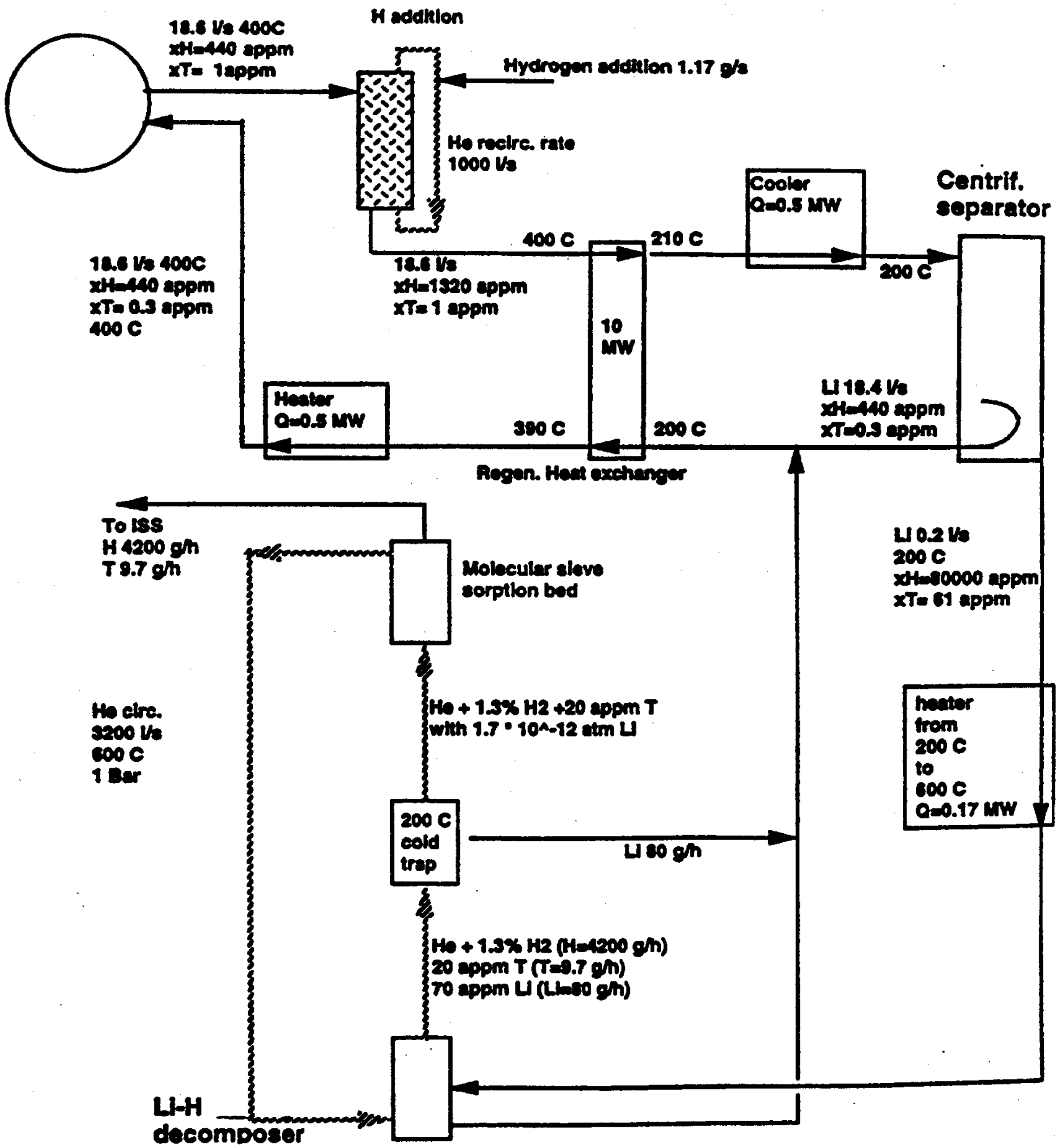

Figure 5.2-9. Cold trap of tritium from lithium.

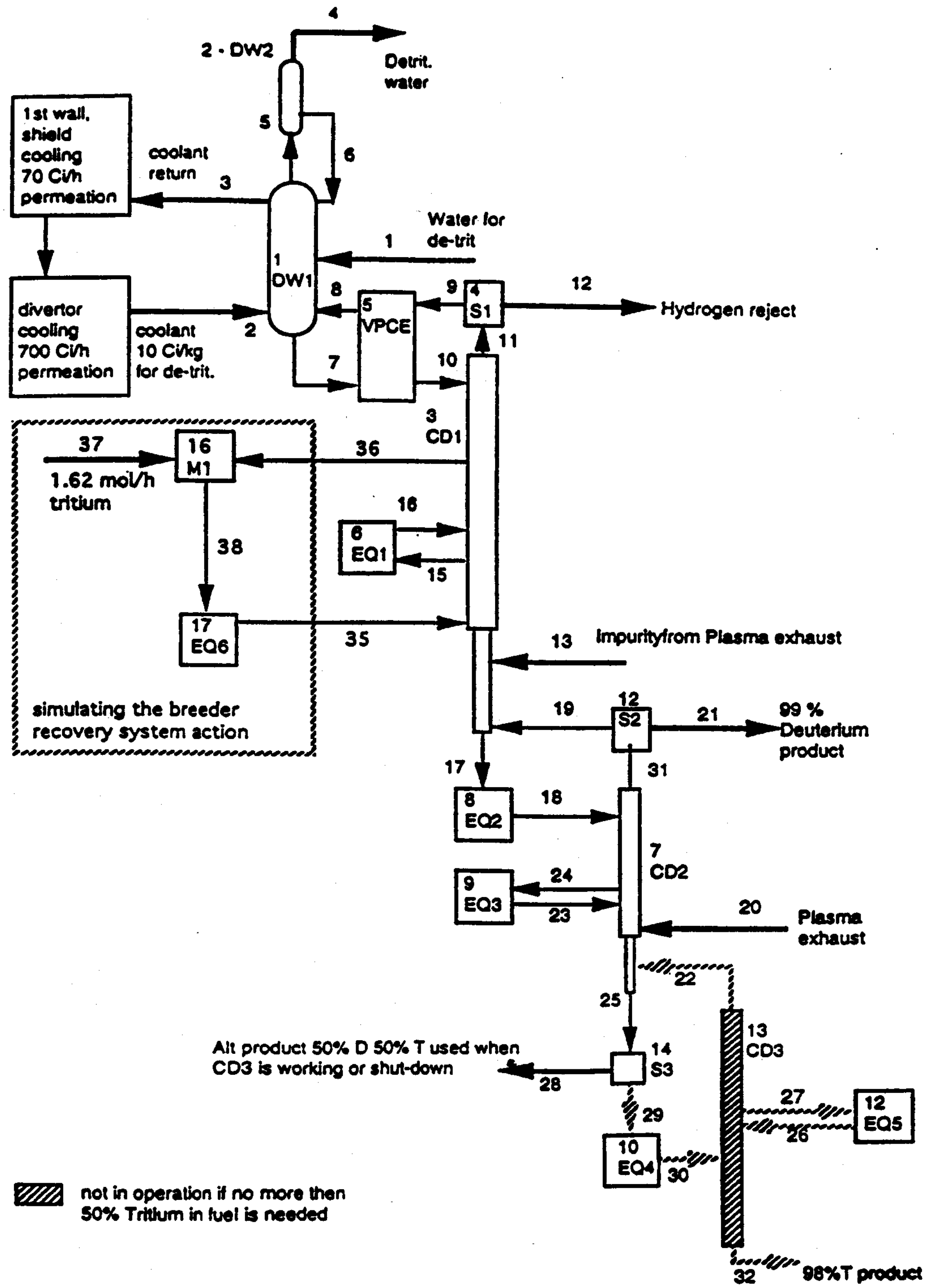

Figure 5.2-10. Isotope Separation System (ISS) arrangement.

as a structural material. Section 5.3.3 documents the details of the design requirements for tritium breeding and the optimal blanket parameters. The radiation damage to the V structure of the first wall, blanket and shield and the lifetime of the different components are covered in Section 5.3.4. The shield follows the blanket and is primarily used to protect the magnets against radiation. Since the dimensions of the shield directly affect the size and cost of the machine, an extensive analysis was performed to optimize the shield composition and performance, as explained in Section 5.3.5.

5.3.2. Neutron Wall Loading Distribution

The average neutron wall loading can simply be calculated by dividing the neutron power by the first wall surface area. However, the wall loading tends to peak at certain locations depending on the wall shape and plasma parameters. Identifying the peaking in the wall loading is of importance in estimating the peak radiation effect and designing an adequate radiation shield to protect the various components of the machine.

In SPPS, the neutron wall loading (Γ) varies in both poloidal and toroidal directions, unlike in tokamaks. This variation is mainly due to the toroidal change in the plasma shape. Figure 5.3-1 shows 4 plasma shapes at the beginning ($0°$) and middle ($45°$) of a field period and at two other locations (22.5 and $67.5°$). The inner surface represents the plasma boundary while the outer surface is the magnet centroid. The first wall follows the plasma contour and the scrape off layer is 15 cm thick. Note that the plasma centers change radially and vertically as one moves along the plasma axis. The plasma is symmetric around the equatorial plane at two locations only, 0 and $45°$. These locations represent two extreme cases as the lowest and highest wall loadings occur at the 0 and $45°$ cross sections, respectively. It should be mentioned that the wall loading at any location is mostly affected by the closely surrounding configuration up to a distance of 1-2 m. In fact, each field period extends toroidally for $\sim$ 22 m and at any location the shape of both plasma and wall do not change significantly over a range of 3-4 m. As such, a 3-D model for the wall loading distribution is not actually required and instead 2-D models at discrete cross sections seem to give reasonably accurate results for the SPPS conceptual design.

The neutron wall loading distribution for SPPS was determined using the NEWLIT code [17]. The code assumes toroidal symmetry with a symmetric plasma shape around the mid-plane. The first wall, however, can take any shape. Two sets of calculations were performed for the two symmetric locations at 0 and $45°$. The plasma boundary was fitted into a D-shape, neglecting the bean shape at $0°$ plasma. The magnetic shift is

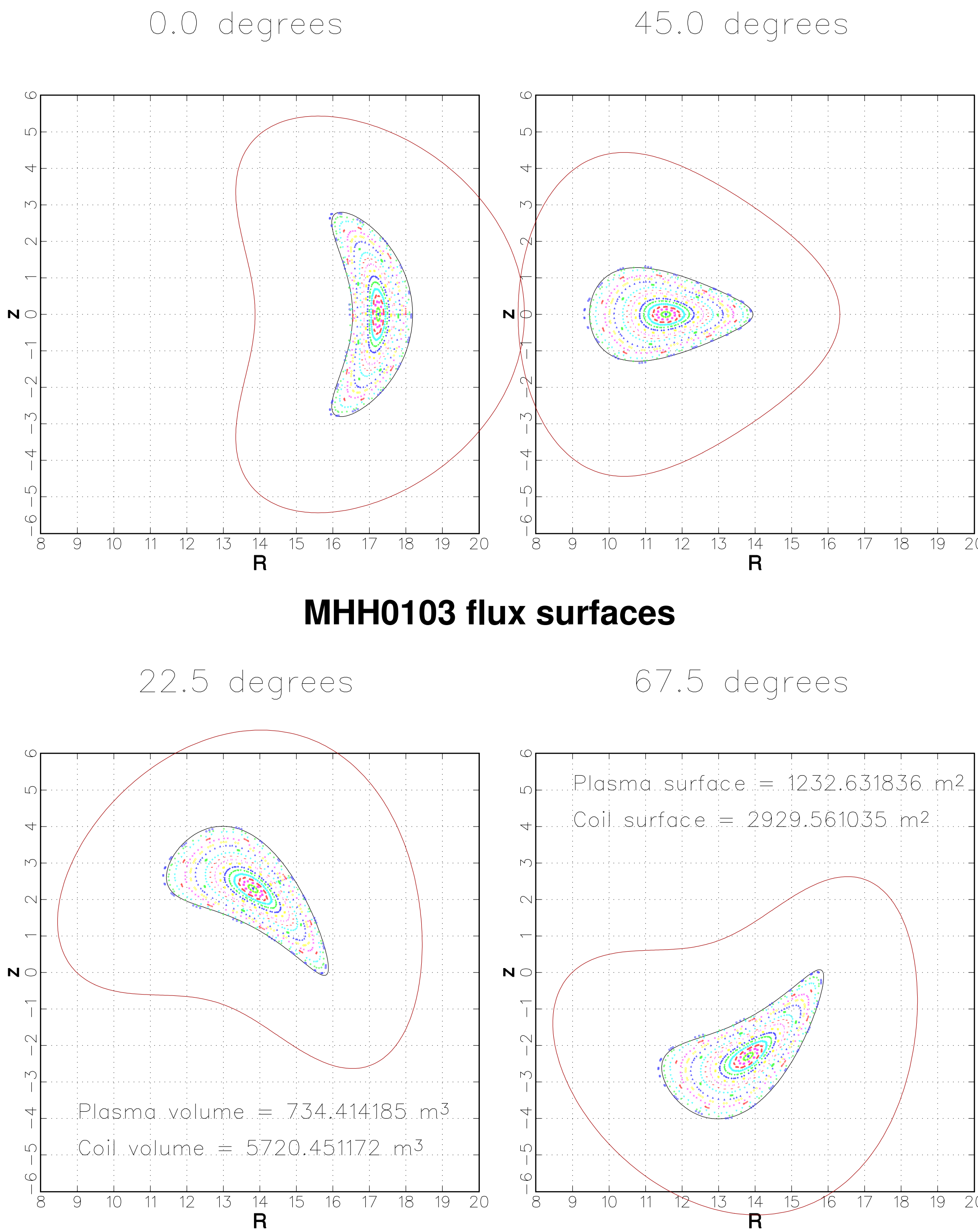

Figure 5.3-1. Cross sections of the SPPS plasma at four toroidal locations: $\phi = 0°$, 22.5°, 45°, and 67.5°. The angle is measured from the beginning of the field period.

small (< 10 cm) and the neutron source varies radially as $[1-(r/a)^2]^2$. The results are normalized to a fusion power of 1,850 MW. The plasma parameters for the two symmetric locations are listed in Table 5.3-I along with the key results from the calculations. The poloidal distributions of the neutron wall loading are illustrated in Figs. 5.3-2 and 5.3-3. The poloidal angle is measured from the outboard mid-plane. The results show that the peak neutron wall loading is 2 MW/m^2 and occurs at the middle of the field period. The minimum wall loading is 0.4 MW/m^2 and occurs at the beginning of the field period. The average wall loading is 1.3 MW/m^2 and thus the peaking factor is 1.5. It should be mentioned that the final results of the systems code indicated a slightly lower fusion power of 1,730 MW and an average wall loading of 1.2 MW/m^2 meaning that the neutronics calculations which are based on the NEWLIT results are slightly conservative.

Table 5.3-I.
Plasma Parameters for Two Cross Sections
(at the Beginning and Middle of a Field Period)

	0°	45°
R (m)	17.4	11.7
a (m)	0.8	2.2
Elongation	3.5	0.59
Triangularity	1.57	0.42
Neutron wall loading		
Average (MW/m^2)	1	1.6
Maximum (MW/m^2)	1.5	2.1
Minimum (MW/m^2)	0.4	1.0
Overall average (MW/m^2)	1.3	

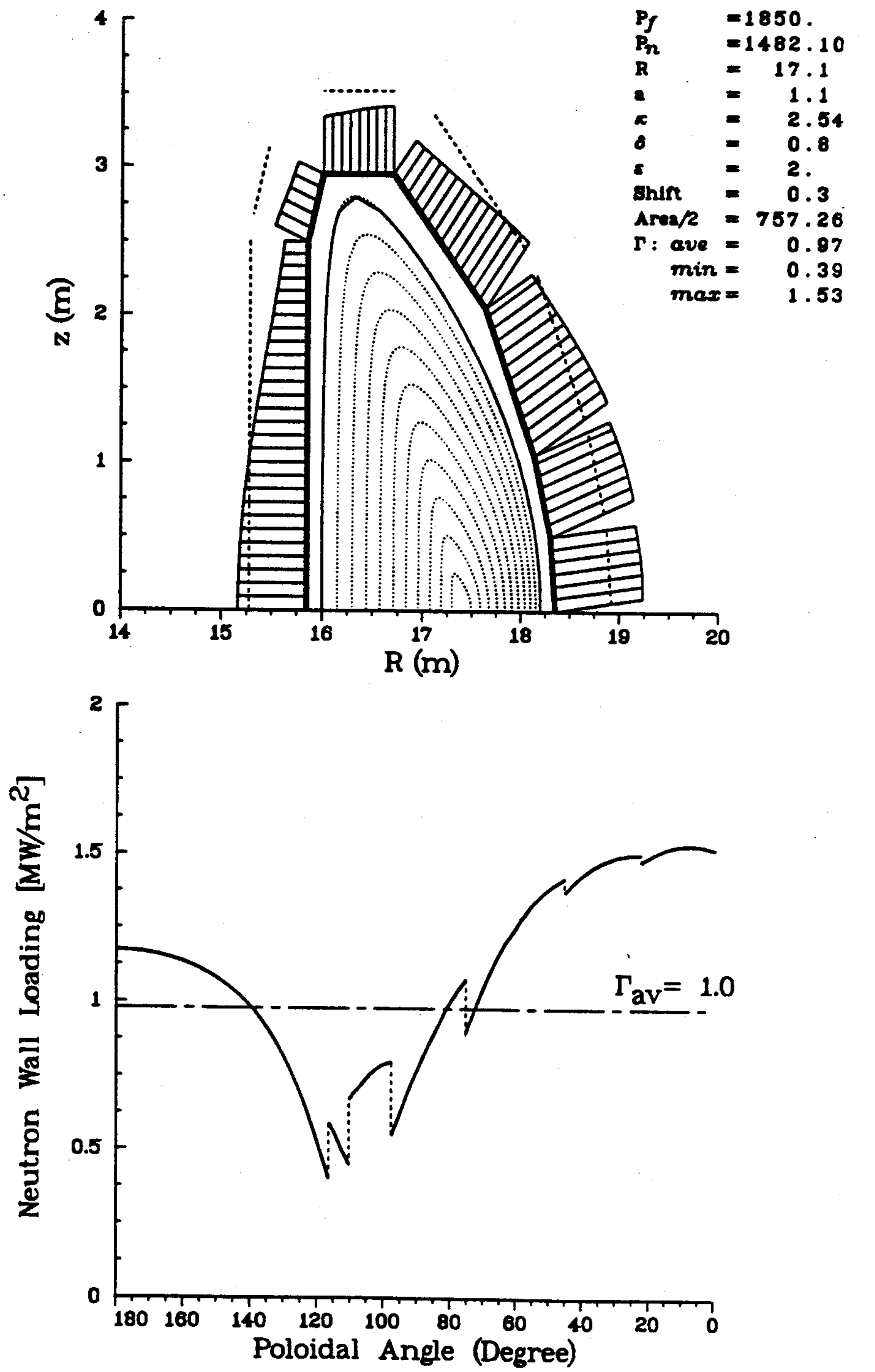

Figure 5.3-2. Approximate poloidal distribution of neutron wall loading at $\phi = 0°$. The 0° and 180° poloidal angles correspond to the outboard and inboard sides, respectively.

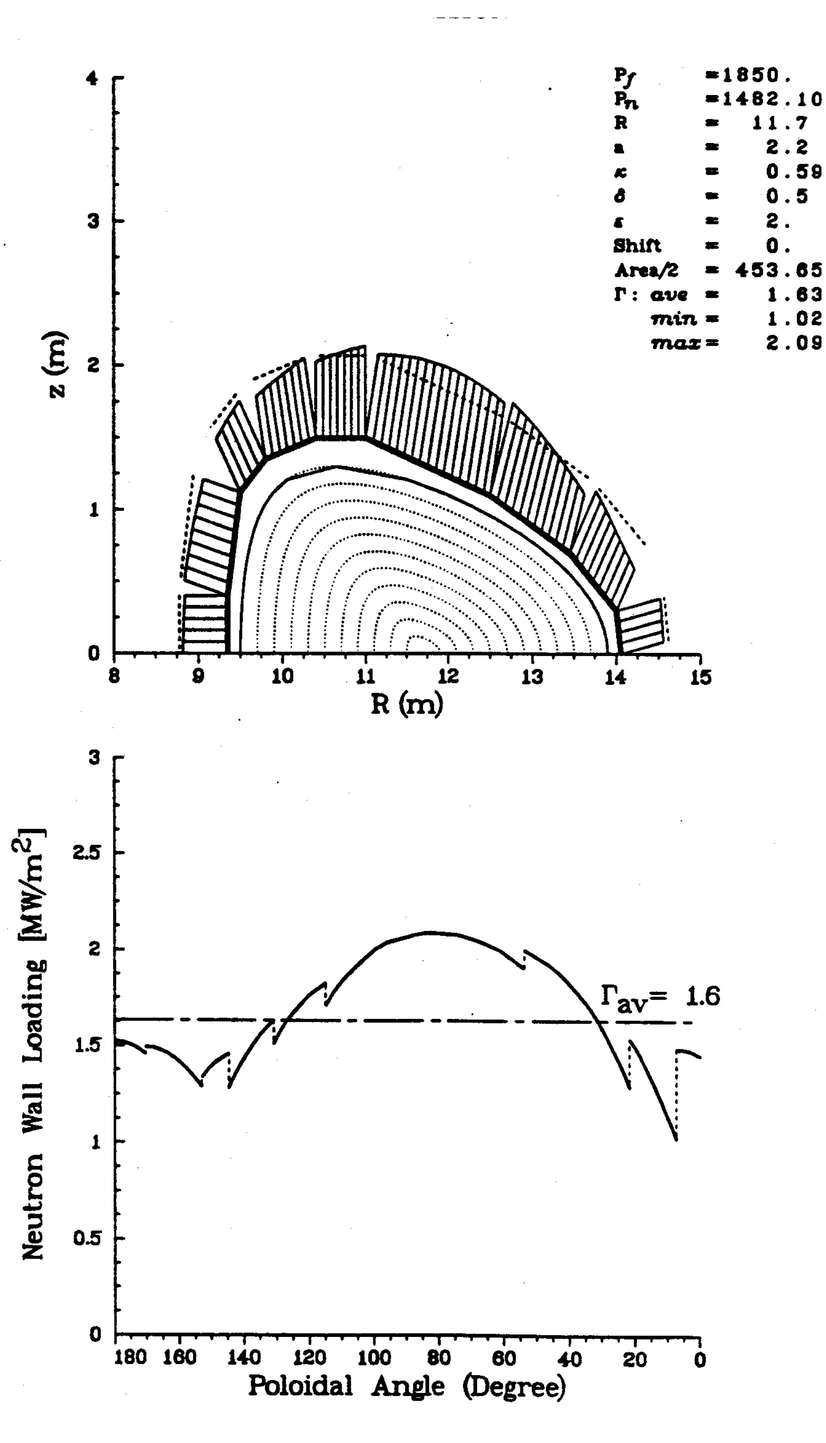

Figure 5.3-3. Approximate poloidal distribution of neutron wall loading at $\phi = 45°$. The 0° and 180° poloidal angles correspond to the outboard and inboard sides, respectively.

5.3.3. Blanket Neutronics

5.3.3.1. Tritium Breeding Requirements

The primary goal of the blanket design is to attain tritium self-sufficiency that ensures the self-sustaining operation of the plant. The requirements to achieve this goal depend on some plasma physics parameters, several uncertainties in the design, and the technical performance of specific fusion core components. To lower the breeding requirements, it is essential to increase the T burn-up in the plasma, ensure extremely low T losses, achieve low T inventory in all subsystems, and require high reliability and fix rate for the T processing systems. It appears that with the existing technology, a system with negligible T leak can be achieved to guarantee a safe and reliable design.

The tritium breeding ratio (defined as the amount of T generated in the blanket per fusion reaction) in a self-sustained power plant must exceed unity by a margin G_o. Thus, the required tritium breeding ratio (TBR) can be expressed as [18]:

$$\mathrm{TBR} \;\; \geq \;\; (1+G_o) + \sqrt{\Delta_G^2 + \Delta_p^2}\,, \tag{5.3-1}$$

where G_o is the breeding margin for the reference design, Δ_G is the uncertainty in estimating $(1+G_o)$, and Δ_p is the uncertainty due to nuclear data, calculational methods, and geometrical models. Here, it is assumed that the design is well defined and no more physics or engineering changes to the reference design are anticipated.

The breeding margin G_0 is necessary to mainly supply the inventory for startup of other fusion power plants, maintain the equilibrium hold-up inventory, provide adequate reserve storage inventory, and compensate for the radioactive decay of T between production and use. The T inventory depends largely on several system parameters such as T fractional burn-up in plasma, T thru-put to the plasma, number of days of reserve inventory, and doubling time. The latter is defined as the time at which the T inventory in the storage is equal to the sum of the initial T inventory required for starting a new power plant and the minimum T inventory that must be kept in storage for continued plant operation during interruption of any part of the tritium cycle. Several approaches were identified to minimize the T inventory in the fusion power core and on-site in the storage and plasma processing facilities. For instance, a high T burn-up fraction of ∼10% and a low T thru-put of 2.8 kg per full power day were considered in order to lower the T inventory in the plasma exhaust processing system. The low T thru-put to the plasma and the short repair time (<1 day) for the T processing system help reduce the reserve storage inventory to ∼0.5 kg. The equilibrium hold-up inventory in the fusion power core (first wall structure, divertor plates, and blanket) is estimated to be ∼2 kg. On this basis, the supply inventory to start a new power plant should be ∼2.5 kg. A doubling time of 5 y seems acceptable for the first-of-a-kind plants and it can be increased to 7–10 y for the tenth-of-a-kind plants.

To calculate the breeding margin G_o, a simple model was employed that accounts for the radioactive decay of T. In order to have a T inventory of 3 kg at the end of a 5 y period, the blanket production rate (P) for T can be calculated using the expression

$$N(t) = \frac{P}{\lambda}(1 - e^{-\lambda t}), \tag{5.3-2}$$

where $N(t)$ is the required T inventory (3 kg), λ is the T decay constant (0.0562 y^{-1}), and T is the doubling time (5 y). In this case, the blanket production rate necessary to supply other plants and provide adequate inventory is estimated to be 1.9 g/day. Using a T thru-put of 2.2 kg/day (@ 76% availability), the breeding margin G_o (P/thru-put × burn-up fraction) amounts to 0.01 for the SPPS reference design.

As noted, the quantity $(1 + G_o)$ is a function of several plasma and engineering components parameters that play a key role in the tritium cycle. Based on the analysis presented in Ref. [18], the uncertainty Δ_G associated with $(1 + G_o)$ for the SPPS parameters is estimated to be <4%. The calculated TBR is also subject to uncertainties (Δ_P) due to approximations and/or errors in the various elements of the calculations such as nuclear data, calculational method, and geometric representation. The uncertainties in the nuclear data include the uncertainties for the basic data, data processing and representation, and tritium production cross sections for lithium. The largest source of uncertainty in nuclear data is that for the basic nuclear data, which is ∼6% for the Li/V blanket [19, 20], and the other uncertainties are small (∼1%). The transport calculations and the 1-D modeling of the blanket involved some geometrical approximations and the associated error is estimated to be in the order of ∼3%. Hence, the uncertainties in the calculational elements total to 10% which is significant and will have a major impact on the breeding requirements.

In this regard, the SPPS design will attain fuel self-sufficiency if the calculated TBR is equal to or exceeds 1.12. It should be stressed that the TBR must be calculated for the reference design and the effects of the blanket coverage, Li burn-up, penetrations, assembly gaps and side walls should all be included in the computed TBR. Also, it is of importance to point out the potentials the blanket design might have to enhance the breeding capability because of the possible existence of uncovered uncertainties in the system definition.

5.3.3.2. Blanket Parameters

The configuration of the SPPS dictates that a simple one-dimensional (1-D) model is capable of handling the SPPS geometry due to the fact that each of the 4 field periods extends toroidally for ∼22 m. Therefore, a poloidal cylindrical model along the plasma axis can reasonably predict the neutronics parameters within a few percent. As mentioned earlier, provisions were made in the tritium breeding requirements for such uncertainties in the results.

To evaluate the impact of the blanket parameters on the tritium breeding ratio and neutron energy multiplication, a simple poloidal cylindrical model was developed for the ONEDANT code [21] where a 1.4 cm thick first wall was followed by a V/Li blanket of variable thickness and, then, a meter thick steel shield. In the analysis, natural Li was used and the blanket thickness was gradually increased from 10 to 80 cm while the V structural content was kept fixed at 10% by volume. The analysis showed that the breeding level can effectively be controlled by adjusting the thicknesses of the blanket. Figure 5.3-4 indicates that a 30-40 cm thick blanket should result in an acceptable TBR, depending on the actual coverage of the blanket.

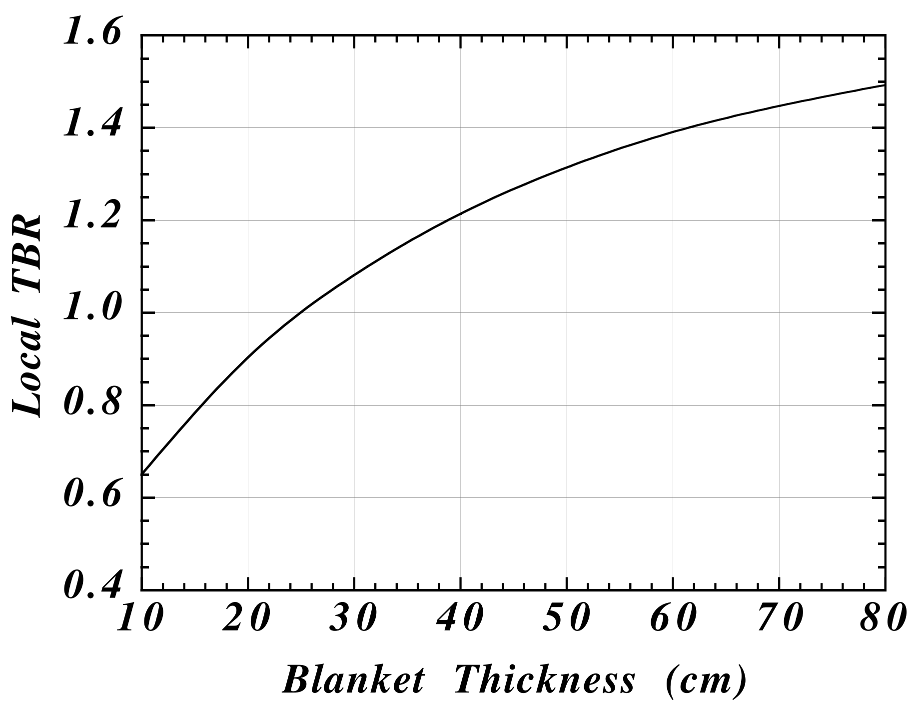

Figure 5.3-4. Variation of tritium breeding ratio (TBR) with blanket thickness.

The blanket surrounds the entire SPPS plasma except for the area occupied by a few penetrations needed for plasma fueling, heating, and control. These penetrations cover approximately 2% of the first wall area. Other components that degrade the breeding are the divertor plates/baffles and their support structures. They are ∼5 cm thick, cover 15% of the first wall area, and consist of 50% V structure, 20% Li coolant, and 30% void. Taking into account the penetrations and divertor effect, the neutronics analysis indicates that a 35 cm thick Li/V blanket will provide T self-sufficiency for the SPPS stellarator design. The contributions from the different components to the breeding are given in Table 5.3-II. The T bred in the 5% Li-cooled shield is small. Considering the 2% loss in breeding due to penetrations, the overall TBR amounts to 1.12. It should be mentioned that higher breeding can be achieved by thickening the blankets and/or enriching the Li to 15–20% ^{6}Li.

The neutron energy multiplication (M) accounts for the nuclear energy deposited in both blanket and shield. The shield design will be covered in detail later in Sec. 5.3.5. However, some changes made to the conventional shield designs are discussed here along with their impact on M and the rational for these changes. The economic analysis of a recent tokamak design [22] employing a Li/V system has indicated that the shield is one of the most expensive components of the machine. The shield contains 15% V structure which comprises more than half of the shield cost. The potential of using less costly materials in the shield while maintaining the safety features of the design was investigated for the SPPS. If the V structure (300 \$/kg) is replaced by a cheaper steel structure (35 \$/kg), the saving in the shield cost will be significant. This certainty will come at a cost in the power balance since V can operate at a higher temperature (700 °C)

Table 5.3-II.
Tritium Breeding in the SPPS Blanket and Shield

	first wall & Blanket	Divertor Region
First wall or divertor	0.04	0.007
Blanket	0.91	0.153
Shield	0.027	0.004

compared to steel (550 °C). An attractive solution is to divide the shield into two parts: the inner part following the blanket operates at a high temperature while the outer part operates at a relatively lower temperature (∼300 °C). The high temperature (HT) shield along with the first wall and blanket employs V structure whereas the low temperature (LT) shield utilizes stainless steel as the main structural material. As the nuclear energy deposited in the LT shield will not be recovered, the dividing boundary between the two shields will depend on how much power could be dumped as a low grade heat without affecting the power balance much (*e.g.,* 1–5%). It was decided to define the HT-LT shield boundary such that 1% of the total nuclear heating be deposited in the LT shield.

Several calculations were performed to estimate the amount of nuclear power deposited in the shield. The results indicated that the 1.4 cm first wall and the 35 cm blanket contain 62% of the nuclear heating while the shield carries the balance. Figure 5.3-5 demonstrates the cumulative heating within the shield. The first wall, blanket, and 45 cm thick shield contain 99% of the nuclear heating and the rest of the shield contains 1% of the heating. The overall energy multiplication is estimated to be 1.4, excluding the 1% heating in the LT shield. The radial distribution of the nuclear heating needed for the thermal hydraulic analysis is illustrated in Fig. 5.3-6 for the reference blanket and shield design. The peak and average heatings are listed in Table 5.3-III for the different components.

Table 5.3-III.
Nuclear Heating in the SPPS first wall, Blanket, and Shield

	Peak$^{(a)}$	Average$^{(b)}$
1.4 cm first wall	11$^{(c)}$	5.2
35 cm blanket	6.7	2.7
45 cm HT shield	6.4	1.1
35 cm LT B-SS shield	0.16	0.02

(a) For 2 MW/m^2 peak neutron wall loading.

(b) For 1.3 MW/m^2 average neutron wall loading.

(c) In V structure.

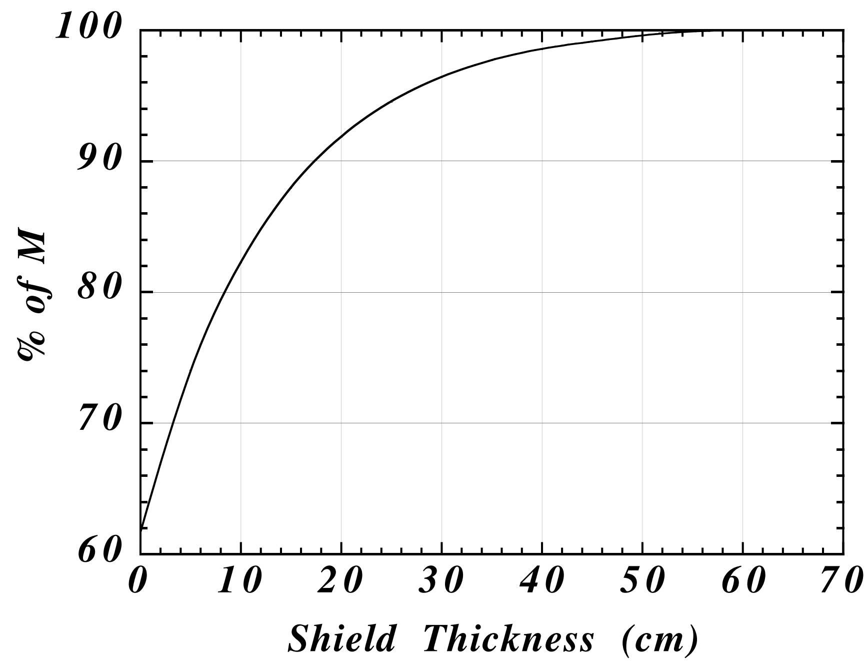

Figure 5.3-5. Cumulative neutron energy multiplication for the 36.4 cm thick first wall and blanket and various layers of the shield.

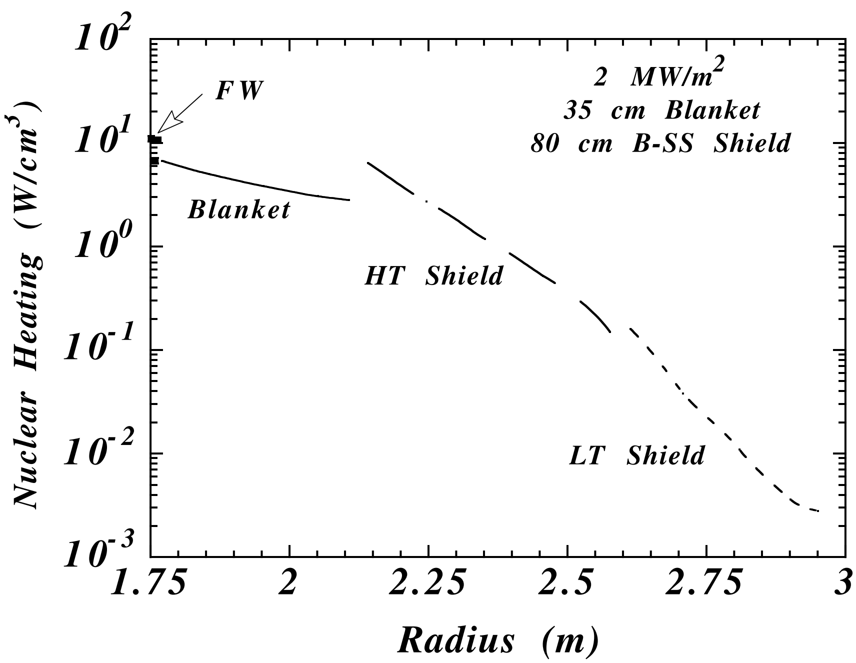

Figure 5.3-6. Radial variation of nuclear heating in first wall, blanket, and shield for the 2 MW/m^2 peak wall loading.

5.3.4. Radiation Damage and Lifetime of V Structure

The 40 y planned operation of the SPPS with 2 MW/m^2 peak neutron wall loading places some constraints on the first wall and blanket systems. The V structure will require frequent replacement during operation. From the radiation damage viewpoint, the lifetime of the V structure of the first wall, blanket, and shield is determined by the level of swelling and embrittlement attainable during plant operation. The atomic displacement level has the most impact on these neutron-induced effects in the V alloys. The V-5Cr-5Ti alloy is the candidate structural material for the stellarator design. This alloy seems to possess high radiation resistance to fusion neutron damage.

The lifetime of V is determined by the dpa level attainable during operation. The criterion adopted in this study is that no more than 200 dpa is desirable. For a peak wall loading of 2 MW/m^2 and a system availability of 76%, the 200 dpa limit implies that the first wall and blanket should be replaced every 11 y and the corresponding end-of-life (EOL) fluence is 16.4 MWy/m^2. The blanket provides lifetime protection for the shield. At the end of the plant life (40 y), the atomic displacement at the V structure of the shield is 170 dpa which is below 200 dpa limit. On this basis, the shield is considered a lifetime component and does not need replacement due to radiation damage.

5.3.5. Shield Design

The main function of the shield is to protect the superconducting magnets and keep the radiation level below the allowable limits. In fact, these limits have a strong impact on the characteristics of the shield, in terms of thickness and composition. In order to reduce the radial standoff of the SPPS, it was essential to optimize the shield in order to reduce the overall dimensions of the machine. As such, a serious effort was made to optimize the shield and the impact of the shield performance on the design was assessed with a view to cost, complexity, and safety.

5.3.5.1. Magnet Radiation Limits

As the radiation adds many problems to the magnet design, sufficient shield should be placed between the blanket and magnet to keep the radiation effects below certain limits. These limits are set by the magnet designers to insure the proper performance of the TF coils. For instance, at the end of 30 full power years (FPY) of operation, the fast neutron fluence ($E_n > 0.1$ MeV) should not exceed 10^{23} n/m^2 to avoid degradation of the critical properties of the Nb_3Sn superconductor material. It is undesirable to subject the magnets to a total nuclear heating above 50 kW to avoid excessively high cryogenic load to the cryoplant. A limit of 2 kW/m^3 is imposed on the peak nuclear heating in the winding pack. The end-of-life dose to the glass-fiber-filled (GFF) polyimide is limited to 10^{11} rads to ascertain the mechanical and electrical integrity of the insulator. The neutron-induced atomic displacement in the Cu stabilizer should not exceed 6×10^{-3} dpa to avoid high increase in the Cu electric resistivity. It should be mentioned that the fluence and dose limits are at least a factor of 2-3 lower than the experimental values at which degradation of properties was observed. Our neutronics calculations indicate that the predominant magnet radiation limits are the EOL fast neutron fluence and the nuclear heat load to the magnets. Hence, the shield is optimized to primarily minimize these effects.

5.3.5.2. Optimization Analysis

An extensive optimization analysis was performed to design a cost-effective high performance shield to protect the magnet against radiation. The optimization study involved the selection of the shielding materials, assessment of the shielding capability of the various candidate materials, optimization of the composition of the shield, and determination of the thickness of the shield required to keep the radiation damage at the magnet below the permissible level.

The analysis employed the 1-D transport code ONEDANT with the P_3 Legendre expansion for the scattering cross section and the S_8 angular quadrature set. The associated 46 neutron and 21 gamma group cross section library was derived from the ENDF/B-V evaluation. The different components were modeled in poloidal cylindrical geometry around the plasma axis. All the in-vessel components are Li cooled. The vacuum vessel is located outside the magnets which are enclosed in a common cryostat. The 75.5 cm winding pack of the magnet includes Incoloy structure, Nb_3Sn superconductor and conduit, Cu stabilizer, GFF polyimide insulator, and liquid He coolant at 25%, 15%, 20%, 25%, and 15% (by volume), respectively. The cryostat consists of 1 cm stainless steel dewar, 5 cm thermal insulator, 7.5 cm coil case, and 1.25 cm electrical insulator. The optimization analysis was carried out for an arbitrary 2.05 m radial standoff measured from the plasma boundary to the magnet centroid. Leaving 15 cm for the scrape-off layer (SOL), 1.4 cm first wall, 35 cm blanket, 2 cm blanket-shield gap, 1.5 cm shield-magnet gap, and 14.75 cm cryostat, the space available for the shield is 97.6 cm. The circularized plasma radius is 1.6 m and the neutron source strength is normalized to the 2 MW/m^2 peak wall loading.

The optimization analysis has focused on optimizing the major factors that influence the shield performance. These factors are the composition of the shield and the arrangement of materials within the shield. A variety of shield options was examined and the ability of various materials to protect the magnets was assessed. Besides V and steel, many materials have the potential to protect the magnets. Each material has some merits and drawbacks. The behavior of the shielding material may limit its use in the shield, particularly in high radiation zones. For example, the tungsten is known as the best shielding material but its high decay heat and the production of the ^{187}W isotope cause some safety problems. The hydrogen compounds (like titanium hydride, zirconium hydride, boron hydride, organic coolant, water, and polyethylene) are superior in slowing down the fast neutrons. Nevertheless, all hydrides decompose at high temperatures and the dissociated hydrogen jeopardizes the integrity of the shield. An ideal situation from the shielding point of view is to use water, borated water (B-H_2O), or organic coolant (OC) to cool the shield. However, this would complicate the cooling system due to the requirement for two independent primary cooling circuits. Moreover, water should be avoided in Li cooled systems for safety reasons. Organic coolants may decompose under irradiation and elevated temperatures. Borated materials (such as boron carbide, boron hydride, boronized carbon, and borated water) possess remarkably high neutron absorption cross sections particularly for low energy neutrons, a property of great importance in magnet shielding. Among these borides, boron carbide is the best for having the combined features of excellent shielding capability, stability under irradiation, and ease of fabrication. One concern regarding the borides is the tritium generated in the boron. To decrease the in-shield tritium inventory, the borides should be situated close to the back of the shield. This constraint turned out to be beneficial since the neutron spectrum therein is relatively soft and the neutron absorption capability of boron is high. The lead has been known for its good ability to reduce magnet heating by absorbing the gamma radiation. However, lead has a few drawbacks of which one should be aware. Lead increases the neutron fluence (compared to steel) as it multiplies the neutrons, starts to deform at $\sim$220 °C and, thus, has to be canned in a structural material, and generates polonium, which is a safety concern.

The first set of calculations demonstrates the shielding performance of several low activation steels. Vanadium alloy is the primary structural material in all shielding components and 15 vol% structure is foreseen enough to support the shield. The option of using steel filler was investigated. At the present time, there is no structural role envisioned for the filler materials in the shield and, therefore, a substantial cost reduction will result from the use of such less costly fillers. There are a few low activation steels that are readily available to be used in fusion plants. These are Tenelon and modified HT-9 (MHT-9). The analysis indicates that Tenelon has the best shielding capability as it gives the lowest magnet damage. Furthermore, it results in the highest neutron energy multiplication since it contains a substantial amount of manganese (14.5 wt%). It is anticipated that the combined effect of the good shielding properties, low unit cost, and high M will have a positive economic impact on the overall design. It should be mentioned that Tenelon has a slightly higher decay heat compared to MHT-9, but this does not seem to present a problem even in the event of a loss of coolant accident.

In the second set of calculations, the composition of the LT shield was optimized to further reduce the radiation damage at the magnet. As mentioned in Sec. 5.3.3.2, the 35 cm thick blanket is followed by a 45 cm thick HT shield then a LT shield. The Tenelon filler in the LT shield was traded for boron carbide, borated water, organic coolant, zirconium hydride, or tungsten carbide. The total HT and LT shield thickness was kept fixed at 97.6 cm. The impact on the magnet damage is illustrated in Figs. 5.3-7 and 5.3-8 . As indicated earlier, the fast neutron fluence and the peak nuclear heating, which is an indicative for the total heating in the magnets, are the most demanding radiation limits. Although water is not compatible with Li, B-H_2O is included in the analysis to illustrate the shielding performance of the selected materials relative to water. As is evident, the hydrides and WC are more effective than B_4C in reducing the magnet damage. In all cases, the damage level at the magnet is well below the fluence and heating limits of 10^{23} n/m^2 and 2 mW/cm^3, respectively. This means the 97.6 cm thick shield over-protects the magnet and a thinner shield is actually needed. Keeping the optimum composition of the various shields, the thickness was reduced from 97.6 cm to 60 cm. Figures 5.3-9 and 5.3-10 indicate that 63–96 cm thick shield is needed to meet the magnet radiation limits, depending on the shield type. Note that the shield thickness required to meet the fluence limit also satisfy the heating limit except for the OC shield where the outer 1–2 cm should be replaced by Pb shield to reduce the heating.

Table 5.3-IV summarizes the required shield to protect the magnet for the various options. The shield of the ARIES-II tokamak design [22] is listed for comparison. The compositions of the different shields are given in Table 5.3-V. It should be noticed that the HT shield contains only Tenelon filler while the use of other materials is limited to the LT shield where the radiation environment is less severe. Borated Tenelon (B-SS; 3 wt% B) is more effective than Tenelon in reducing magnet damage. Even though zirconium hydride and organic coolant are better shielding materials than WC and borides, the

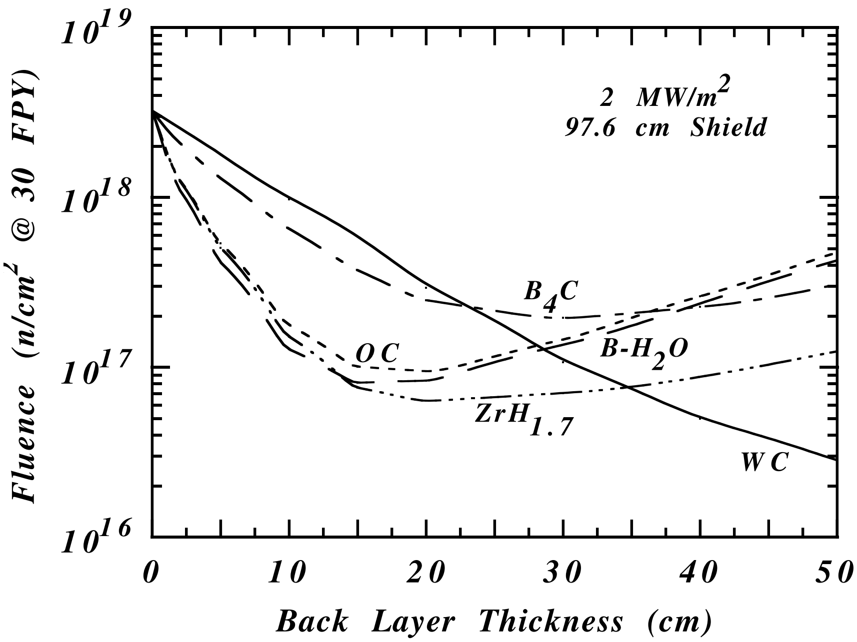

Figure 5.3-7. Effect on fast neutron fluence at magnet of replacing the back layer of the steel shield by more efficient shielding materials.

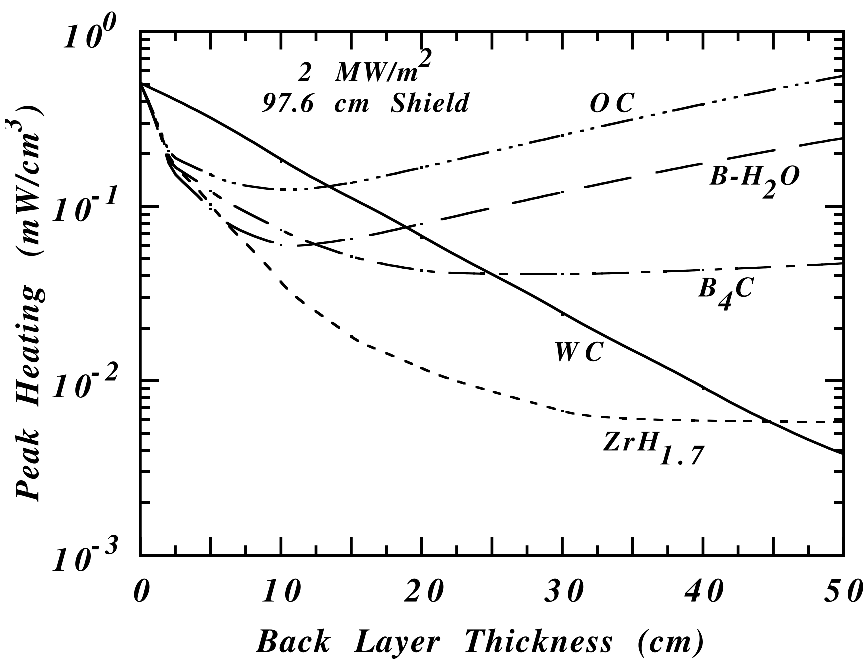

Figure 5.3-8. Effect on peak nuclear heating at magnet of replacing the back layer of the steel shield by more efficient shielding materials.

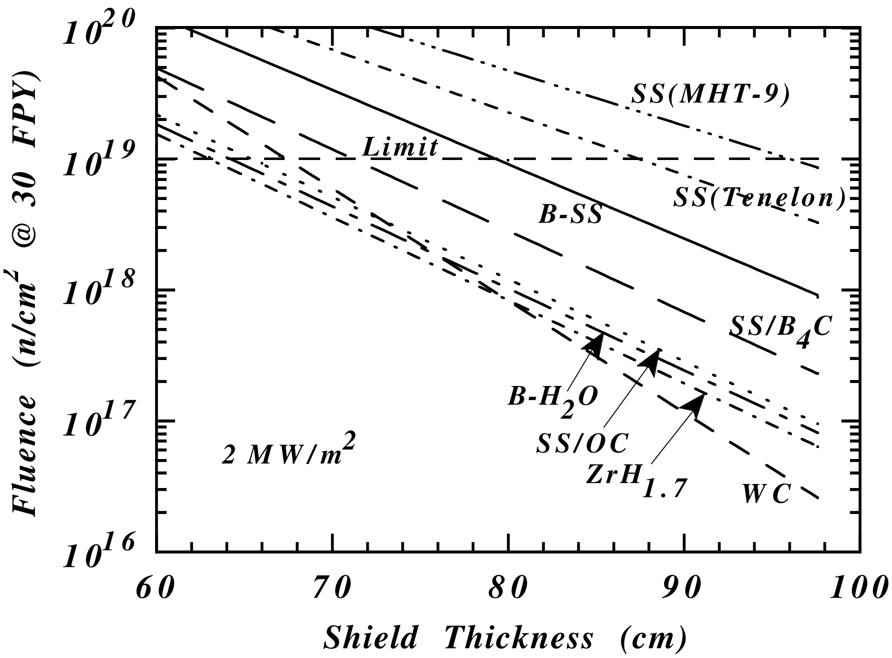

Figure 5.3-9. Variation of fast neutron fluence at magnet with thicknesses of various shields.

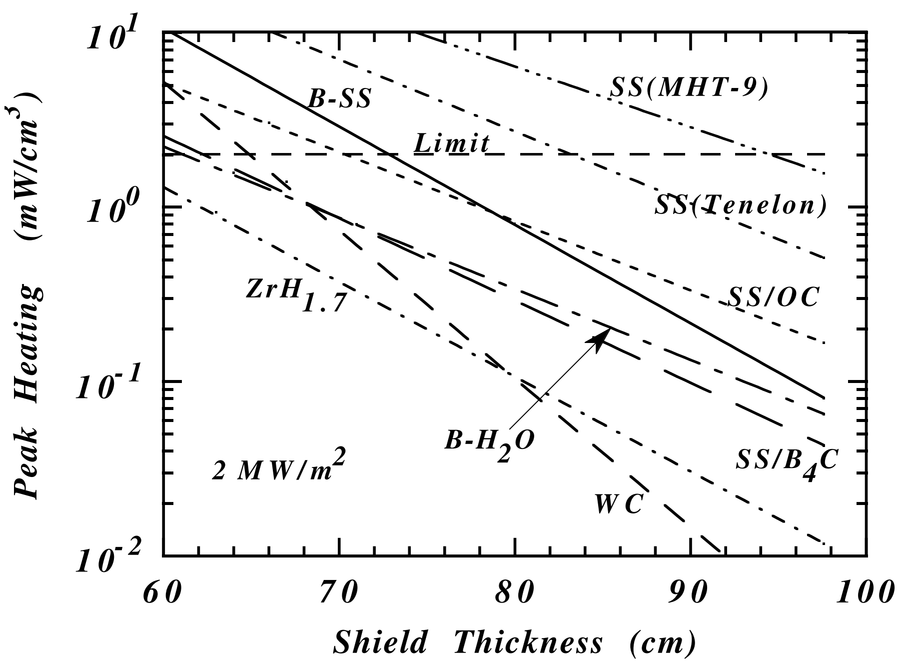

Figure 5.3-10. Variation of peak nuclear heating at magnet with thicknesses of various shields.

Table 5.3-IV.
Radial Thicknesses (cm) of Different Shield Options

	ARIES-II(a)	SPPS					
Shield Type	B_4C	SS	**B-SS**(b)	B_4C	WC	OC	$ZrH_{1.7}$
First wall	1.4	1.4	1.4	1.4	1.4	1.4	1.4
Blanket	20	35	35	35	35	35	35
Reflector	15	—	—	—	—	—	—
HT Shield(c)	47	45	45	45	45	45	45
LT Shields:							
SS/Li	—	42	—	11	—	6.3	5
B-SS/Li	—	—	35	—	—	—	—
B_4C/SS/Li	23(d)	—	—	15	—	—	—
WC/SS/Li	—	—	—	—	22	—	—
OC/SS	—	—	—	—	—	13.2	—
Pb/SS/OC	—	—	—	—	—	1.5	—
$ZrH_{1.7}$/SS/Li	—	—	—	—	—	—	13
Vacuum Vessel	10	—	—	—	—	—	—
Coil Case	2	8.5	8.5	8.5	8.5	8.5	8.5
Total(d)	118	132	125	116	112	111	108

(a) Inboard components operating at 3.2 MW/m^2.

(b) Reference Case.

(c) A SS/Li/V high-temperature shield.

(d) High-temperature shield.

(e) Excluding gaps.

Table 5.3-V.
Materials Composition[a] for Different Shield Options

First Wall	30% V structure, 70% Li coolant
Li/V Blanket	10% V structure, 90% Li coolant/breeder
HT SS/Li/V Shield	15% V structure, 5% Li coolant, 80% Tenelon filler
LT SS-Based Shield:	
SS/Li	15% Tenelon structure, 5% Li coolant, 80% Tenelon filler
LT B-SS-Based Shield:	
B-SS/Li	15% Tenelon structure, 5% Li coolant, 80% B-Tenelon filler
LT B_4C-Based Shield:	
SS/Li	15% Tenelon structure, 5% Li coolant, 80% Tenelon filler
B_4C/SS/Li	15% Tenelon structure, 5% Li coolant, 80% B_4C filler
LT WC-Based Shield:	
WC/SS/Li	15% Tenelon structure, 5% Li coolant, 80% WC filler
LT OC-Based Shield:	
SS/OC	15% Tenelon structure, 5% organic coolant, 80% Tenelon filler
OC/SS	10% Tenelon structure, 90% organic coolant
Pb/SS/OC	15% Tenelon structure, 5% organic coolant, 80% Pb filler
LT $ZrH_{1.7}$-Based Shield:	
SS/Li	15% Tenelon structure, 5% Li coolant, 80% Tenelon filler
$ZrH_{1.7}$/SS/Li	15% Tenelon structure 5% Li coolant, 80% $ZrH_{1.7}$ filler

(*a*) Fillers are in the form of bricks.

safety related issues associated with these materials limited their use in the SPPS design. For instance, $ZrH_{1.7}$, which is more stable than ZrH_2, will decompose at elevated temperatures ($> 600\,°C$). Although the shield temperature can be controlled during operation to remain below 500 °C, the temperature in case of a loss of coolant accident (LOCA) will rise and certainly exceed 600 °C causing dissociation of hydrogen and jeopardizing the integrity of the shield.

The organic coolant (a kerosene product commercially known as therminol 66 or HB-40) decomposes under irradiation and elevated temperatures. To mitigate the decomposition problem, the OC is used only in the LT shield where the temperature and radiation levels are low. Nevertheless, the decomposition rate is quite high. The radiolytic decomposition rate (R_r in kg/h) and pyrolytic decomposition rate (R_p in kg/h per kg of OC) can be expressed as

$$R_r = 0.0131 \left[\frac{100 - HB}{100 - 30}\right]^2 D \,, \tag{5.3-3}$$

$$R_p = \left[\frac{100 - HB}{100 - 30}\right]^2 e^{(25.73 - 180.98/\mathrm{RT})} \,, \tag{5.3-4}$$

where HB is the high boiler content in wt% (40 wt%), D is the radiation absorbed dose in kW, R is the gas constant (0.00831 kJ/K), and T is the temperature in K. Table 5.3-VI summarizes the decomposition rates in the various zones of the LT shield. The radiolytic decomposition rate is high whereas the pyrolytic decomposition rate is manageable at the 100 °C operating temperature. However, in the worst accident case of a LOCA in the blanket and LOFA in the shield, the temperature may exceed 600 °C leading to excessive decomposition of $> 10^6$ kg/h. Even though the OC is confined to the low radiation outer zone, the decomposition rates are still excessive and this excluded the use of OC in the SPPS.

5.3.5.3. Reference Shield Design

The optimization analysis has indicated that borated steel and tungsten carbide are the most promising shielding materials. A decision was made to employ the 80 cm thick borated steel to protect the magnets of the present design ($R = 14$ m). It was found that the minimum radial distance between the plasma and the magnet centroid is 196.2 cm and occurs at the middle of each field period, as indicated in Fig. 5.3-11. This space is actually more than what is needed for the SOL, blanket, shield, and magnet. The shield-magnet gap is, therefore, 8 cm wide for the reference B-SS as indicated by the

Table 5.3-VI.
Decomposition Rates for the Organic-Coolant Shield Option

Low-temperature Shield	SS/OC	OC/SS	Pb/SS/OC
Volume Content	95%/5%	90%/10%	80%/15%/5%
Thickness (cm)	6.3	13.2	1.5
In-vessel OC volume$^{(a)}$ (m^3)	4.6	180	1.2
In-vessel OC mass$^{(a)}$ (tonnes)	5	200	1.3
Absorbed dose (kW)	172	2,400	5
Radiolytic decomposition rate:			
(kg/FPH)	1.7	23	0.05
(kg/h)$^{(b)}$	1.3	18	0.04
Pyrolytic decomposition rate @100 °C (kg/h)	6×10^{-11}	2×10^{-9}	2×10^{-11}

(a) Outer loop contains the same amount.

(b) Assuming 76% availability.

radial build shown in Fig. 5.3-12. This gap gets wider as one moves in the toroidal and/or poloidal directions reaching 1.3 m at some locations. It should be mentioned that the B-SS is employed in the LT shield only in order to reduce the in-shield tritium inventory. Although a 4 cm reduction in thickness is feasible upon employing B-SS in both HT and LT shields, the excessive in-shield T produced at the end of the plant life (1.080 kg) excluded this option. The level of radiation damage at the magnet is compiled in Table 5.3-VII for the various shield options. All magnet radiation limits are met and the reference B-SS shield results in the lowest heat load to the magnet. The 32 magnets of SPPS cover $\sim$ 20% of the space. For an average wall loading of 1.3 MW/m^2, the nuclear heating deposited in the coil cases and winding packs amounts to 37 kW and will be removed at a cryoplant efficiency of 310 W/W. The cryoplant load is thus 11 MW. This corresponds to $\sim$1% of the output power, which is acceptable. The radial distribution of the nuclear heating in the magnet is shown in Fig. 5.3-13 for the reference B-SS shield design.

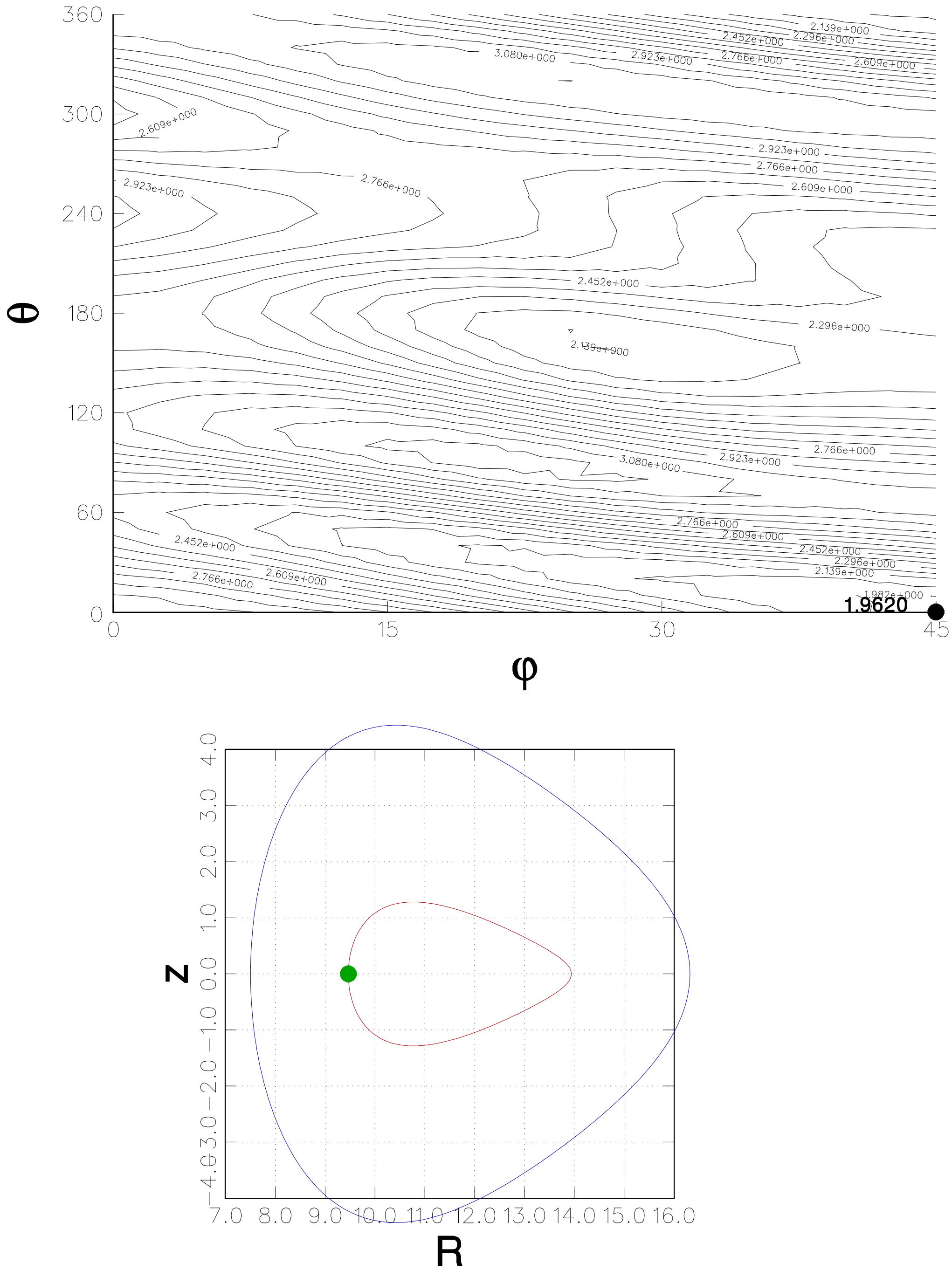

Figure 5.3-11. A contour plot of the distance between the SPPS plasma boundary and coil centroid in the $\theta - \phi$ (poloidal angle-toroidal angle) plane. The lower part of the picture shows the point (•) where the spacing is smallest (at the inboard side of the torus).

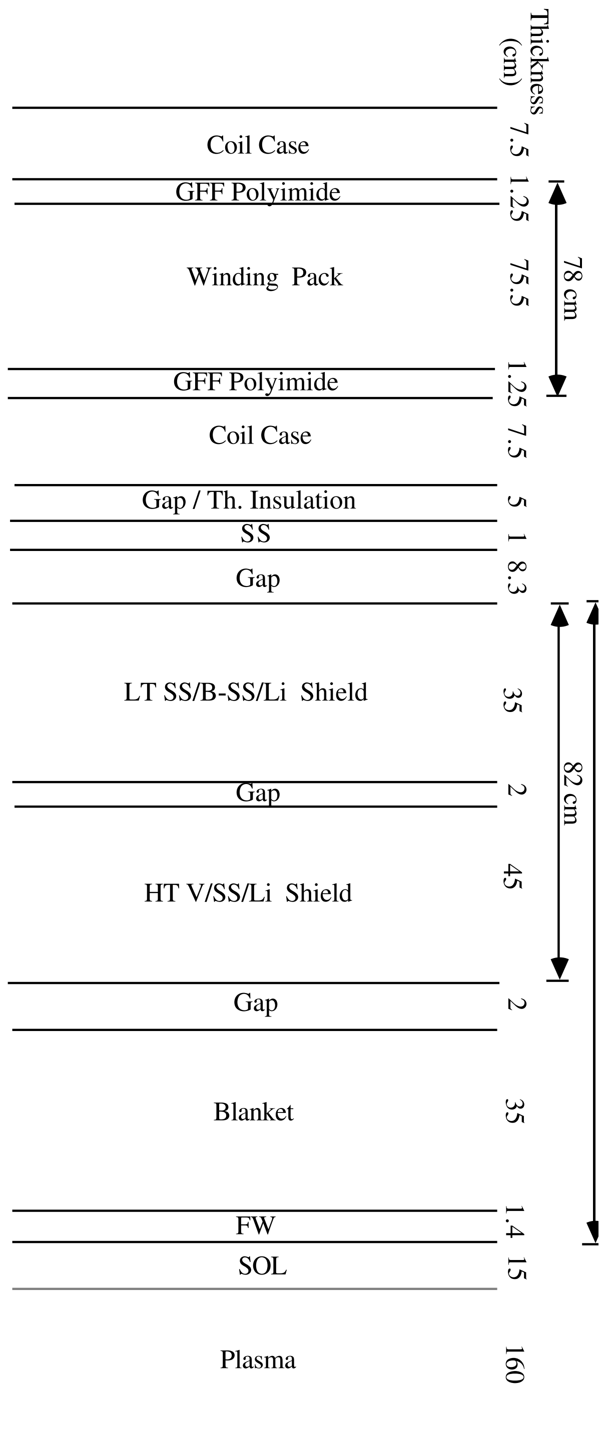

Figure 5.3-12. Schematic of SPPS blanket, shield, and magnet.

Table 5.3-VII.
Radiation Level at Magnet for the Various Shield Options

Shield Type	SS	**B-SS**[(a)]	B_4C	WC	OC	$ZrH_{1.7}$
Shield thickness (cm)	87	80	71	67	66	63
Total thickness[(b)] (cm)	127	120	111	107	106	103
Minimum shield-magnet gap (cm)	2	8	17	21	23	26
Peak fast n fluence to Nb_3Sn (10^{19} n/cm^2@30 FPY)	1	1	1	1	1	1
Peak nuclear heating in Winding Pack (MW/m^3)	1.5	0.8	0.8	1.4	1.9	0.9
Peak dose to insulator (10^{10} rads@30 FPY)	2.4	1.4	1.6	2.3	3.4	1.9
Peak dpa in Cu stabilizer (10^{-3} dpa@30 FPY)	4.5	4.0	4.8	5.0	5.8	6.2
Total nuclear heating (kW):						
Coil case	38	17	35	34	153	56
Winding Pack	34	20	19	33	32	20
Total	72	37	54	67	185	76
Cryogenic load (MW):						
Coil case	12	5	11	11	47	17
Winding Pack	10	6	6	10	10	6
Total	22	11	17	21	57	23

(*a*) Reference Case.

(*b*) Including First wall, blanket, high- and low-temperature shields and gaps.

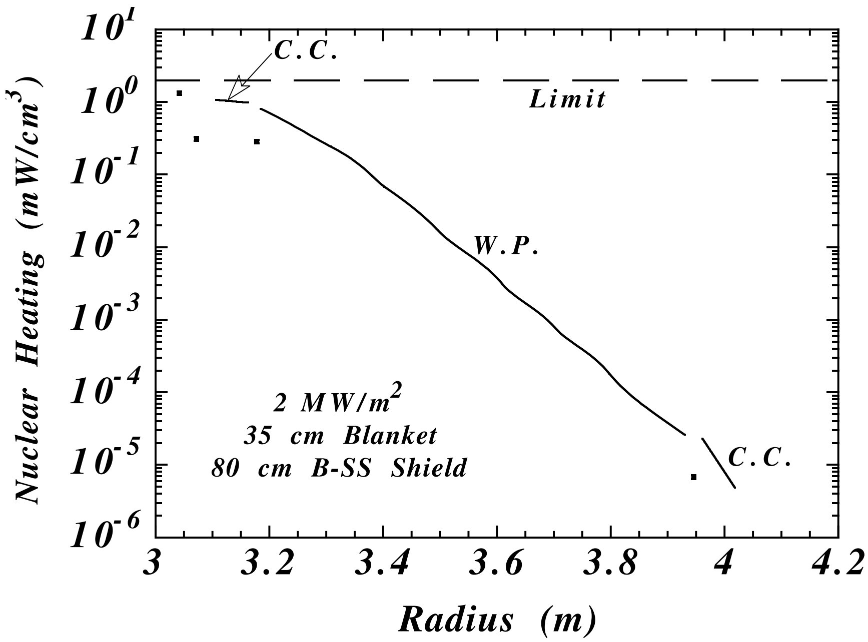

Figure 5.3-13. Radial distribution of nuclear heating in the magnet for the 2 MW/m^2 peak wall loading.

A potential improvement to the present design is to employ a more efficient shield in order to reduce the radial standoff and thus the overall dimension of the machine. The most efficient shielding material is the tungsten carbide. However, WC is heavy and expensive (65 \$/kg) and should be used only in the critical area where the space is constrained. As mentioned before, there is a single critical area at the middle of each field period where the shielding space is limited. Utilizing WC in this region, which cover only 1% of the area, will allow the radial standoff to be reduced by 19 cm. The corresponding reduction in the major radius is estimated to be in the order of 1.5 m. It should be stressed that the WC used in the LT shield is subject to a relatively low radiation level implying that the afterheat generated by W is low and will not cause any problem in case of an accident.

5.3.5.4. Thermal Analysis

The thermal analysis has been performed for the HT shield to determine the size of the Tenelon bricks used in the various layers of the shield. The thickness of the steel filler is needed for the safety analysis to estimate the release fraction from the steel in case of an accident. The HT shield is configured in 3 steel layers sandwiched between coolant channels, as illustrated in Fig. 5.3-14. The V structure, steel filler, and coolant contents amount to 15%, 80%, and 5% by volume, respectively. The V coolant channel wall is 0.6 cm thick. The front and back V plates of the shield are 1 cm thick each.

The temperature distribution was calculated for a two-dimensional $(r-\theta)$ sector of the HT shield using the finite element ANSYS code [23]. The inner and outer radii of the shield are 213 cm and 258 cm, respectively. The coolant is fed at the back of the shield at 350 °C and collected at the front at 600 °C. The front of the shield is assumed to radiate to the back of the blanket which operates at an average temperature of 400 °C. A perfect thermal contact between the different parts of the shield is assumed. The radial distribution of the nuclear heating in the HT shield, shown in Fig. 5.3-6, was renormalized to an average wall loading of 1.3 MW/m^2. The temperature distribution generated by the ANSYS code is shown in Fig. 5.3-14. The analysis indicates that the thickness of the first steel layer is 9.1 cm which could be manufactured in two pieces, 4.55 cm each. The second and third layers are 16.8 and 11.6 cm thick, respectively. The maximum temperature in the first layer of the shield reaches 655 °C which is below the allowable limit (< 700 °C) for the Tenelon filler. The temperature of the V structure does not exceed the 700 °C limit.

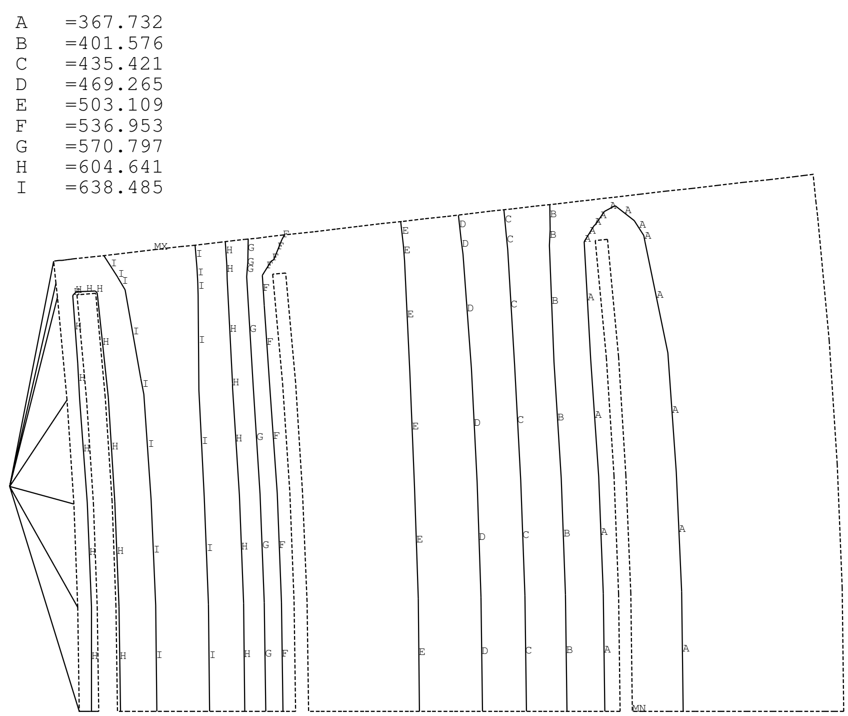

Figure 5.3-14. Temperature distribution in the HT shield.

5.4. CONFIGURATION AND MAINTENANCE

5.4.1. Introduction

This section describes the configuration and layout of the SPPS fusion power core, the surrounding structure and its interfacing with the magnets, the cryostats which contain the magnets, the vacuum chamber, and the maintenance procedures for both blankets, divertors and magnets.

Modular stellarator coils differ from tokamak coils in many ways, not only in configuration, but also in force magnitude and distribution as well. Whereas the toroidal field coils in tokamaks have net centering forces which are reacted with a structural center post, the net force on the various stellarator coils point in different directions. These forces have both horizontal and vertical components, which means that they have to be surrounded with structure on all sides. This cocoon of structure must be arranged in such a way as to provide access to the coils for maintenance operations.

There are also differences in blanket and divertor maintenance procedures between tokamaks and modular stellarators. Traditionally, blanket maintenance in tokamaks invoked radial module extraction between toroidal field (TF) coils, or vertical extraction through access ports at the top of the vacuum chamber [24–26]. Although, there have been proposals for maintaining tokamak blankets by moving TF coils [27], these have since been abandoned. Whereas the tokamak has the luxury of several possible blanket maintenance schemes, the modular stellarator of the SPPS configuration must have at least some of the coils moved to provide access for blanket maintenance. There simply is not enough access space between coils for the capability of blanket module extraction without coil movement, unless the blanket is divided into very small segments, which makes it impractical.

Fortuitously, maintaining the divertor segments will not require coil movement. This is important, particularly if the lifetime of the divertor will be shorter than that of the blankets. The divertor modules are concentrated in four locations within the plasma chamber. These are the four corners of the near square shape of the coil assembly, when viewed from the top. At these corners, the legs of the coils on the outboard side are sufficiently separated as to allow access between them for reaching the divertor segments. It is planned to have a large rectangular access port to be located on the outboard side of the corner cryostat which contains the four corner coils. Removing the blanket and shield segments in front of the access port uncovers a large opening through which remote manipulators can disengage and remover divertor segments.

Finally, any power-plant design must have contingency plans for replacing coils in the event of a failure. Since blanket maintenance requires the extraction of 16 of the 32 coils in the SPPS system, the remaining 16 coils must also be provided with replacement capability. This has been provided for and will be covered in the sections that follow.

5.4.2. Overall Configuration

The SPPS modular stellarator power plant consists of 32 twisted coils assembled in a near square geometry when viewed from the top as shown in Fig. 5.4-1. There are four field periods in the system, each consisting of eight coils, however, only four of the coils have different geometries and the other four are identical, but flipped 180° about a radial horizontal axis. Each of the four different geometries will be duplicated eight times, making fabrication simpler by virtue of a learning curve. The eight coils in a field period occupy one leg of the near square assembly of the coils. Figure 5.4-2 is a view of a field period as seen from the outside looking toward the center of the fusion core. Note

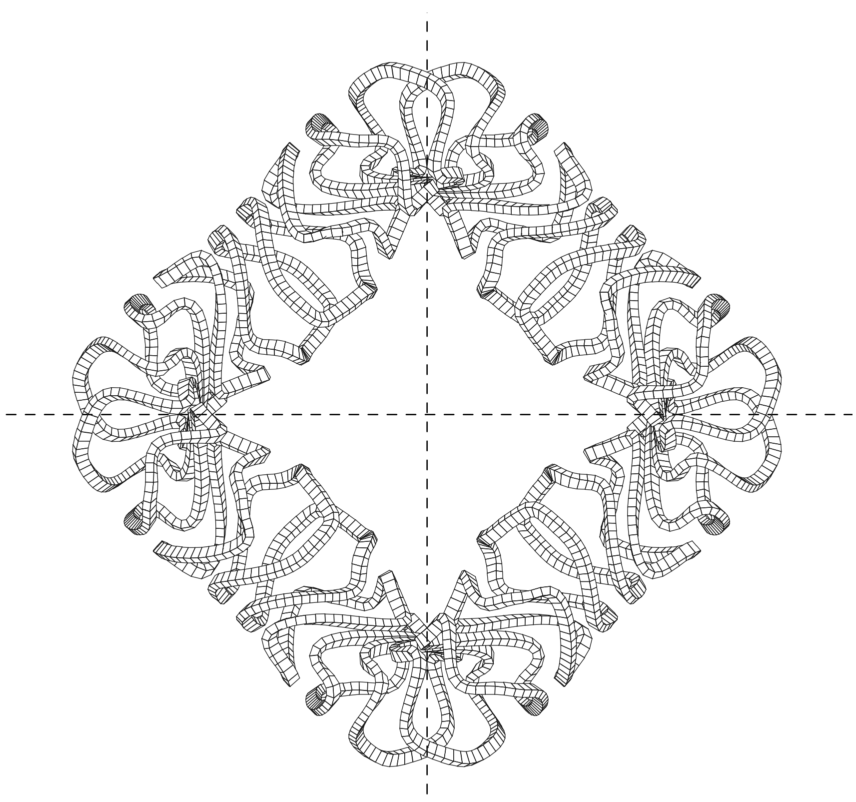

Figure 5.4-1. Plan view of SPPS coil set.

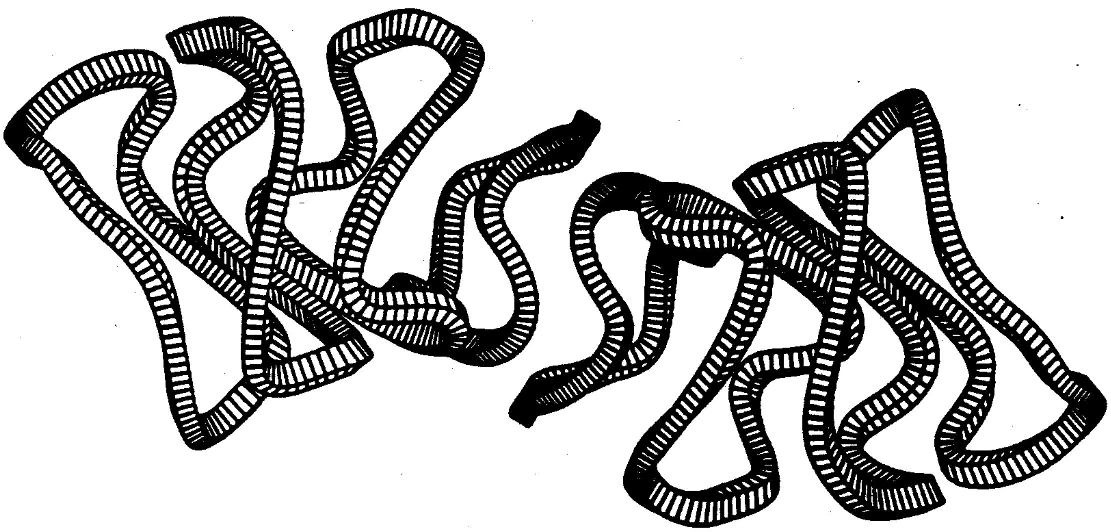

Figure 5.4-2. Side view of SPPS coil field period as viewed from outside.

that the coils are not centered on the same plane, but have different elevation within one field period. The same geometry and coil placement repeats itself in the succeeding field periods.

The magnets are housed in 12 cryostats. The number of cryostats and the division of coils per cryostat was arrived at from maintenance considerations and will be discussed in a future section. Each cryostat will have its own vacuum system. The magnets will be superinsulated and structural gravity supports or reactive local supports will have intercepts at 77 K (liquid N_2) to minimize heat leaks. Intercoil supports, where the loads are transferred from one cryostat to an adjacent one, thus going through a cold/warm/cold interface, will also have 77 K intercepts. The cryostats are contained within a doughnut shaped vacuum chamber which has a nominal outer radius of 21 m and an inner radius of 5 m, and is $\sim$18 m high. The vacuum chamber has four access ports located in line with the corner cryostats as shown in Fig. 5.4-3 which is a top view of the vacuum chamber with the roof and over-the-top structure removed. It will be shown later, that by moving out the corner cryostats radially through the access ports, makes it possible to maintain the internal components of the plasma chamber.

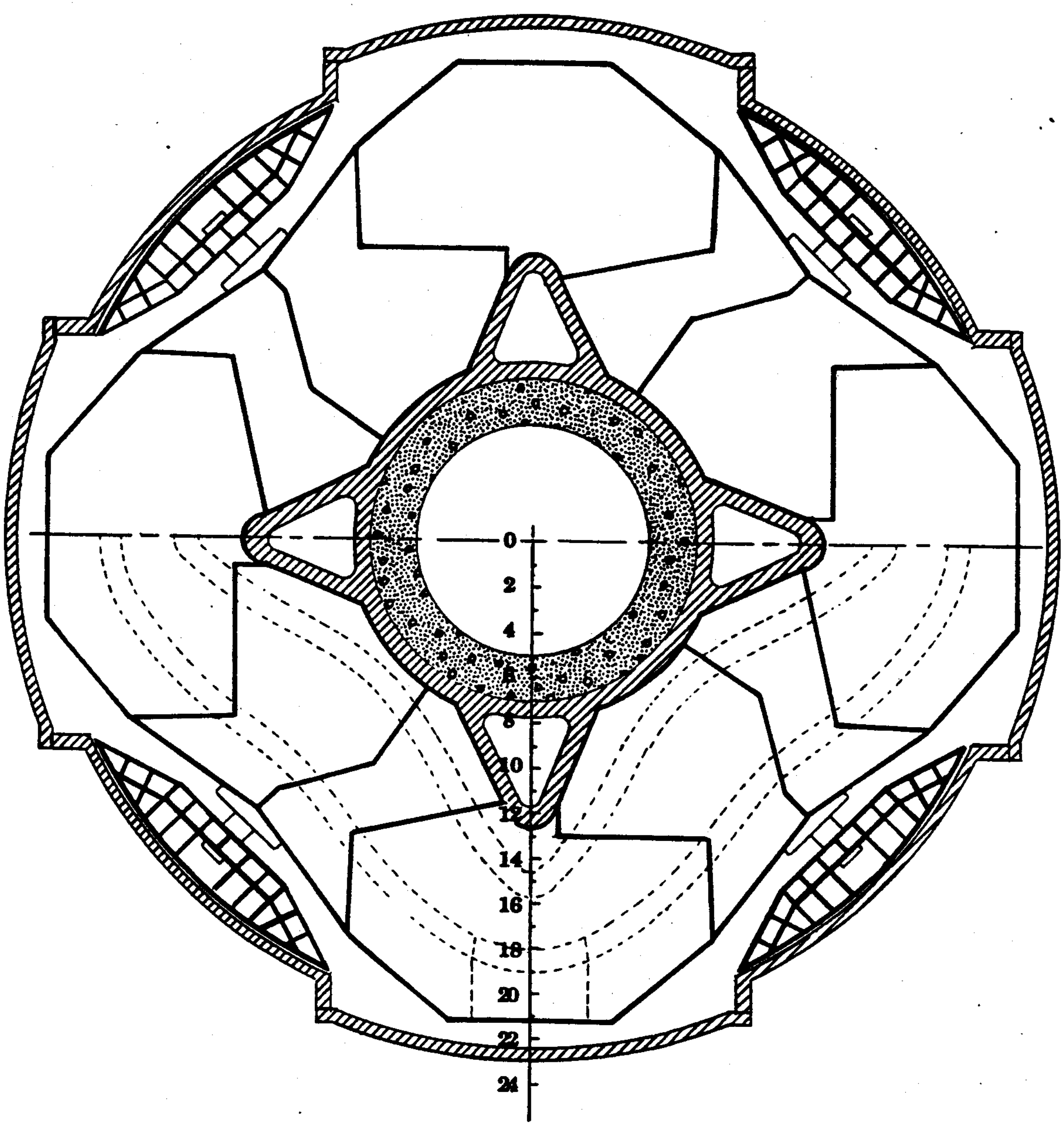

Figure 5.4-3. View of SPPS vacuum chamber with roof and over-the-top structure removed.

The shape of the plasma in this stellarator changes in one field period from a crescent with rounded ends to a horizontal tear drop in the middle of the period, and then back to a crescent. Further, the elevation of the plasma also changes from one end of a field period to the other. Because it was so difficult to visualize the plasma in 3D, a model of one field period was constructed. Coils are shown as planar, simply to show the boundary around the plasma chamber. Plastic plates assembled in a radiating fashion from a central hub hold wires strung out through them to show the shape of the plasma. Two photographs of the model are shown in Fig. 5.4-4. A top view and a side view of the model show the variations in the shape and location of the plasma within a single period. The same configuration then repeats itself within each period.

The plasma chamber fits within the bore of the coils which means, each cryostat has a hole going through it from one side to the other. When all the cryostats are assembled within the vacuum chamber, there is a continuous channel going around the torus. This channel contains the radiation shield, the breeding blanket, the plasma and the divertor modules. The shape of this channel somewhat conforms to the shape of the plasma. Since the magnets constitute a large fraction of the cost of the fusion core, their size must be minimized, and this can be accomplished by making the blanket/shield conform to the plasma shape. Although this saves on the cost of the coils, it makes it more difficult to change out blanket modules. The cryostats butt against each other but are not sealed to each other. This means that the plasma chamber will communicate with the vacuum chamber through assembly gaps between the blankets, shields and cryostats. Similar schemes are used in tokamak designs, although the total pumped surface area is smaller in tokamaks, due to the smaller size of the vacuum chamber. Aside from the fact that it would be difficult to make seals between adjacent cryostats, there is one more reason which would preclude such a step, and it has to do with safety related loss of coolant accidents (LOCA). When a LOCA occurs, the afterheat generated within the blanket and shield must be conducted, convected or radiated to other cooler surrounding components. Since in this stellarator, the plasma chamber is entirely surrounded by cryostat walls, there are no places where this energy can be radiated to, and conduction by itself is not sufficient to dissipate the energy. For this reason, holes through the cryostats will be located at strategic places which will allow afterheat energy to be radiated to surrounding structures from the back of the shield. These holes will exist in places where there are sufficiently large spaces between the coils within the cryostats and will extend from the inner plasma channel wall to the outer cryostat perimeter. Naturally, the holes will be self enclosed, preserving the separate vacuum environment of the cryostats. Nevertheless, this makes seals between adjacent cryostats superfluous.

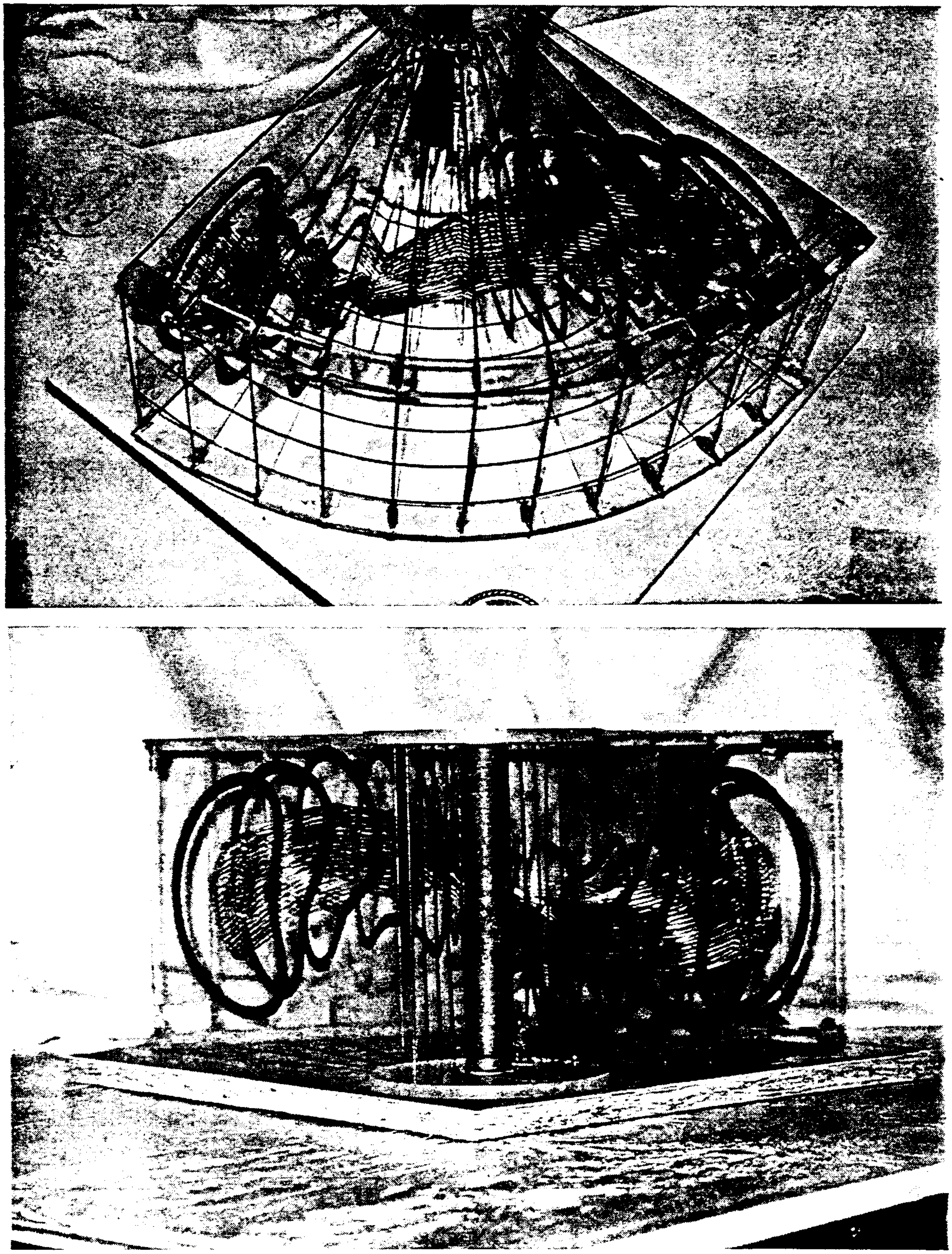

Figure 5.4-4. Photographs of the SPPS plasma model.

5.4.3. Blanket and Shield Configuration

It was mentioned in the previous section that the blanket and shield in this stellarator conform to the contours of the plasma. This means that the shape of the plasma chamber is continuously changing from one toroidal location to the next. Figure 5.4-5 is a plot of the first wall circumference as a function of toroidal angle within one field period. It shows the circumference changing from 14.5 m at $\phi = 0$ to 12.2 m at $\phi = 45°$ and back to 14.5 at $\phi = 90°$, a variation of 16%. This variation is due to the change in the plasma shape from a vertical crescent with rounded ends at $\phi = 0$ and 90°, to a horizontal tear drop shape at $\phi = 45°$. These contours are shown in Fig. 5.4-6 at intervals of 8.2° from $\phi = 0$ to $\phi = 40.9°$. Note that the plasma shape (dotted lines) spirals counter-clockwise around the nominal major radius of the machine at $R = 13.9$ m and $Z = 0$. The last solid line in these pictures represents the centerline of the coil at that location. Figure 5.4-7 is a CAD generated picture of the plasma surrounded by the blanket/shield, and Fig. 5.4-8 shows the same picture within the bore of the coils.

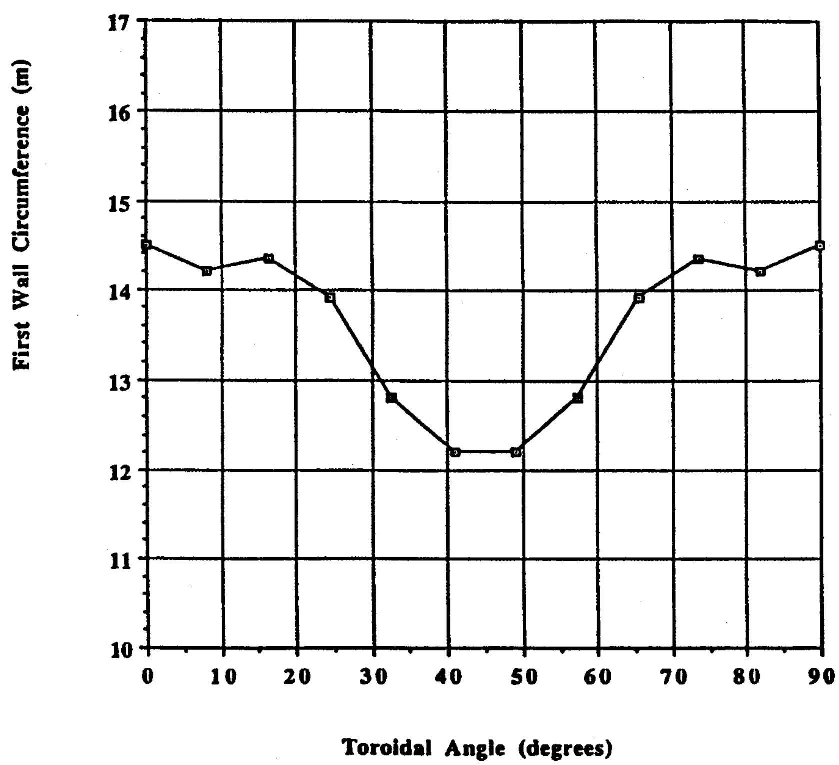

Figure 5.4-5. Plot of the SPPS first wall circumference as a function of toroidal angle within one field period.

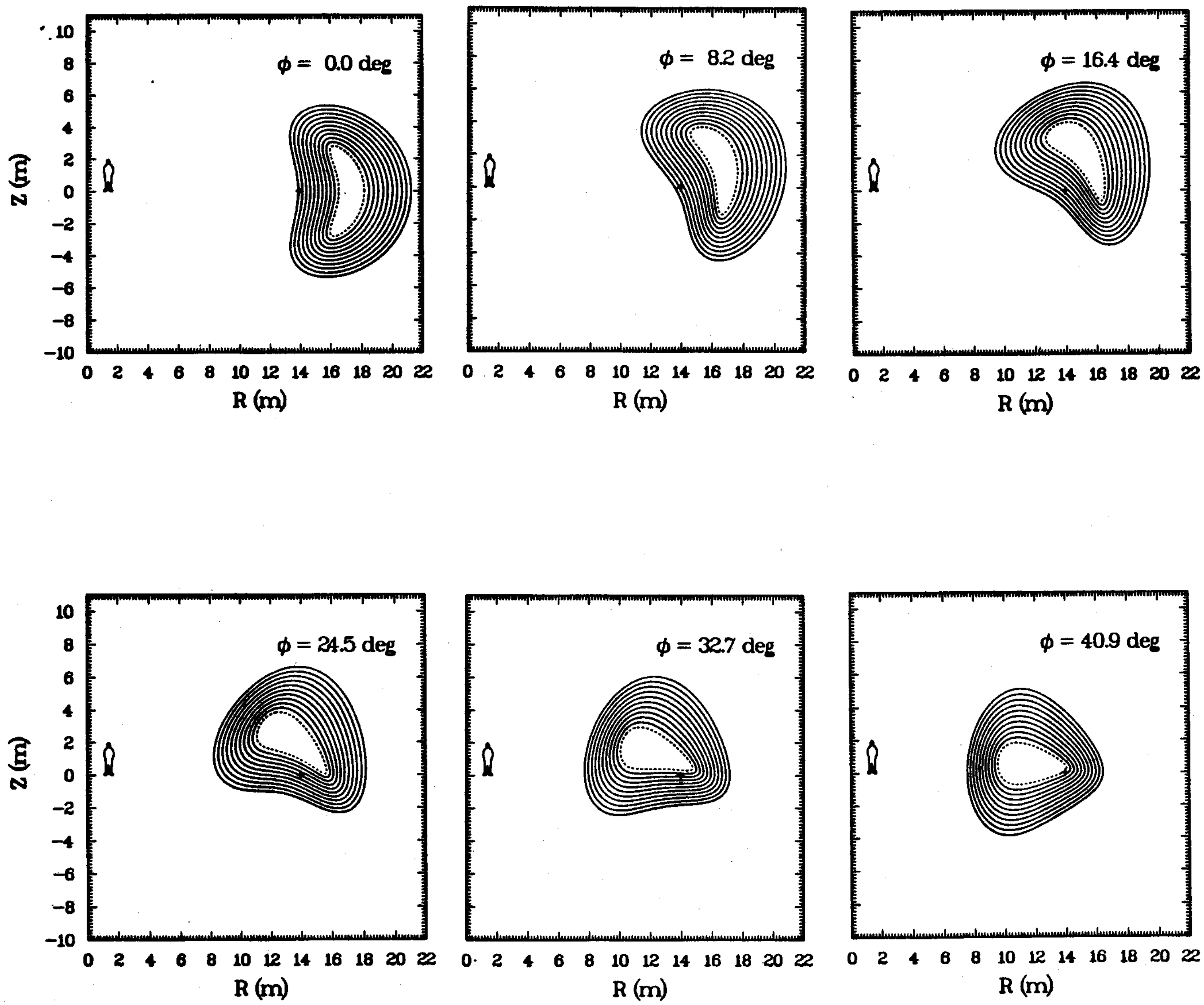

Figure 5.4-6. SPPS plasma contours at different toroidal angles.

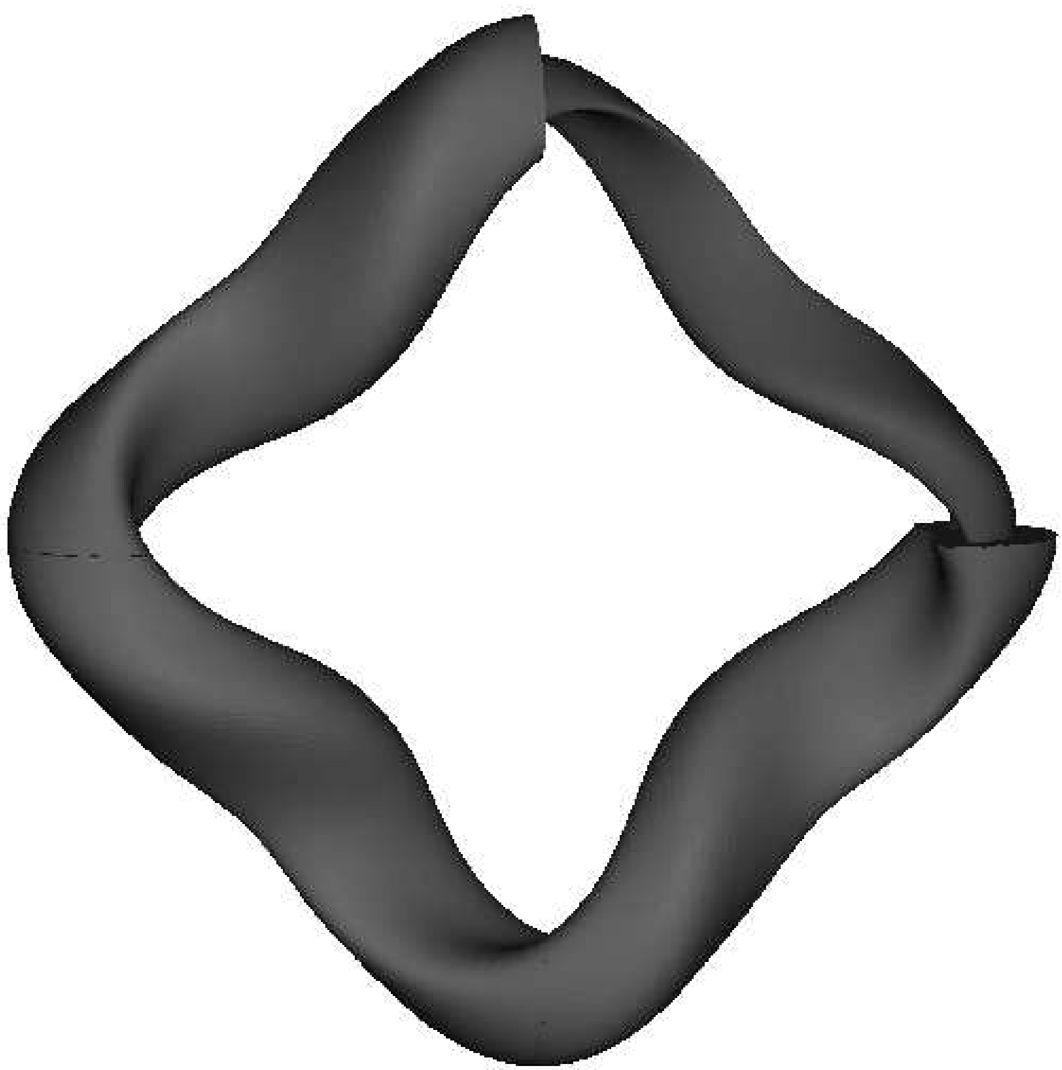

Figure 5.4-7. View of the SPPS plasma surrounded by the blanket and shield.

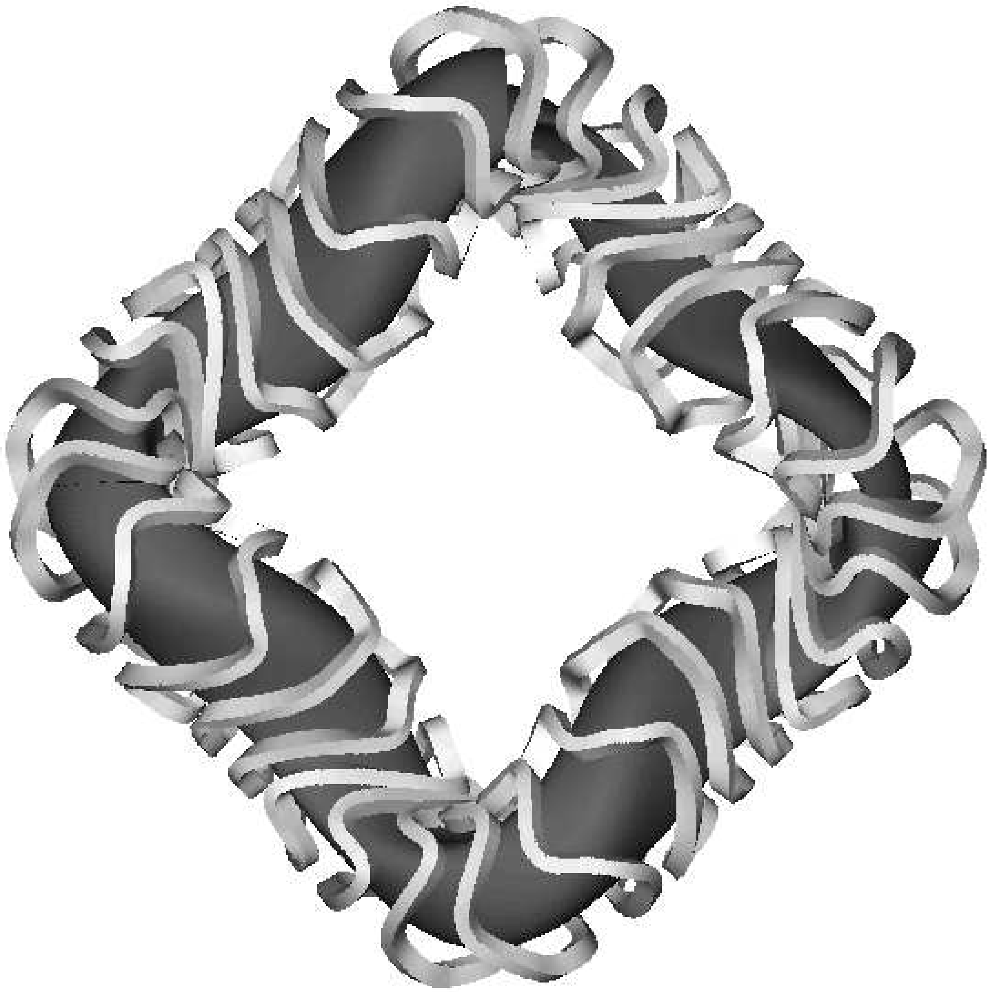

Figure 5.4-8. View of the SPPS plasma surrounded by the blanket, shield, and coils.

To facilitate the maintenance of blanket/shield components, they were subdivided every 8.2°, making up 44 modules altogether. Each corner cryostat will house six modules for a total of 24, and the remaining 20 modules are distributed, five modules each, in the four straight legs of the torus. The modules consisting of the blanket and hot shield are subdivided each 8.2°, to make it easier for removing them from the ends of the cryostats. Figure 5.4-9 is a top view of the stellarator core with the top cover of the vacuum chamber and the over the top structure removed. There are 12 cryostats, four corner cryostats and eight others, two in each straight leg of the torus. The dotted lines define the outer limits of the blanket/shield in two field periods. Modular subdivision is shown in one field period with the modules numbered from 1-11 or from $\phi = 0°$ to $\phi = 90°$. The first corner cryostat will house modules 42, 43, 44, 1, 2 and 3. Note that modules 2 and 3 and on the other side, 42 and 43, actually protrude from the corner cryostat into the adjacent ones. This is purposely done to aid in their replacement during maintenance, and in no way will interfere with the radial extraction of the corner cryostat through the access port. Figure 5.4-10 gives the top and side views of the blanket/removable shield of modules 1, 2 and 3 as numerated in Fig. 5.4-9. The top view shows the relative location of each module with respect to the line going through the center of a corner cryostat which is also the start of a field period. On the other side of the center of the corner cryostat (*i.e.,* modules 42, 43 and 44) the shapes of the modules will be the same as modules 1, 2 and 3 except that they would spiral in the opposite direction. Modules 4, 5 and 6 would complete the half period and their shapes would progress to a horizontal tear shape with the blunt end pointing toward the center of the machine.

5.4.3.1. Location of Divertors within the Blanket/Shield

A detailed design of the divertor plates is not within the scope of this study. Studies on where particles leave confinement after having been launched at different places around the plasma have been made and are reported elsewhere in this report. This section describes where the divertor plates must be located and, in a later section, how they will be maintained.

Figure 5.4-11 shows one half of the SPPS coil set, the plasma contours at -26.5°, 0.0° and +22.5° respectively, and a 3D front view of the plasma last MHD stable flux surface. The divertor plates' and baffles' locations are shown covering the pointed extremities of the plasma contours as is also evident from the volumetric plasma picture between the limits of ±26.5°. Figure 5.4-12 is a top view of the fusion core showing the extent of divertor plate coverage for the upper and the lower divertors. Note that the upper divertor

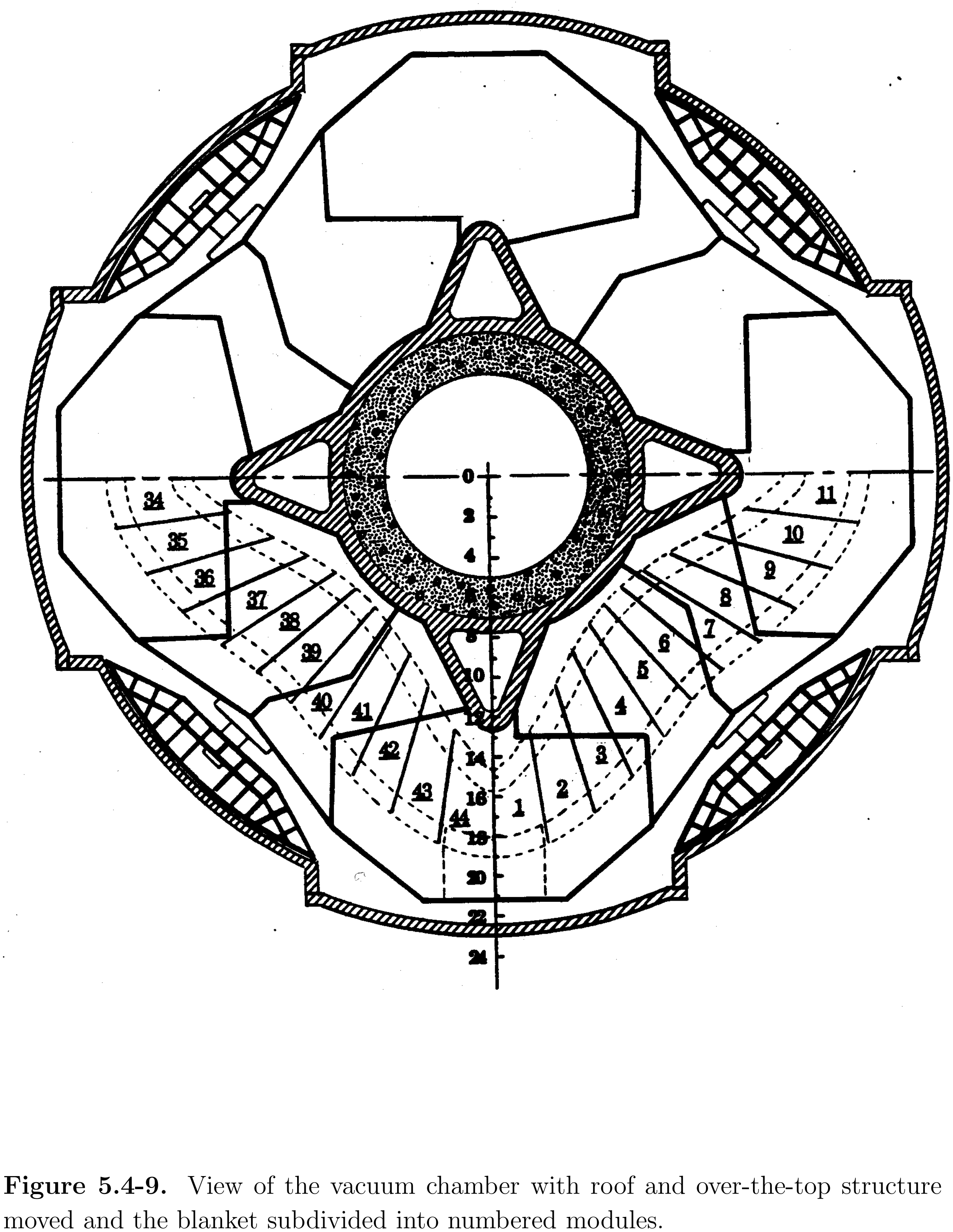

Figure 5.4-9. View of the vacuum chamber with roof and over-the-top structure removed and the blanket subdivided into numbered modules.

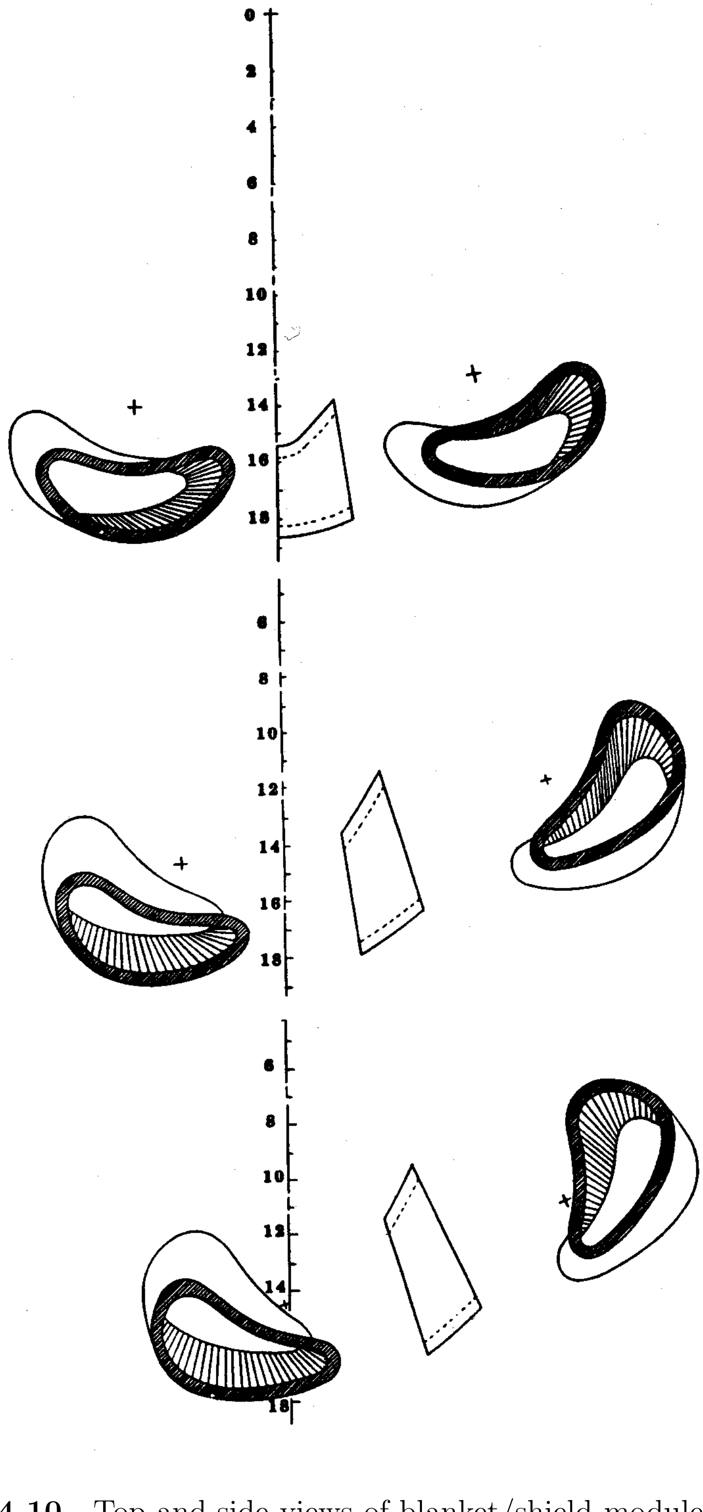

Figure 5.4-10. Top and side views of blanket/shield modules 1, 2 and 3.

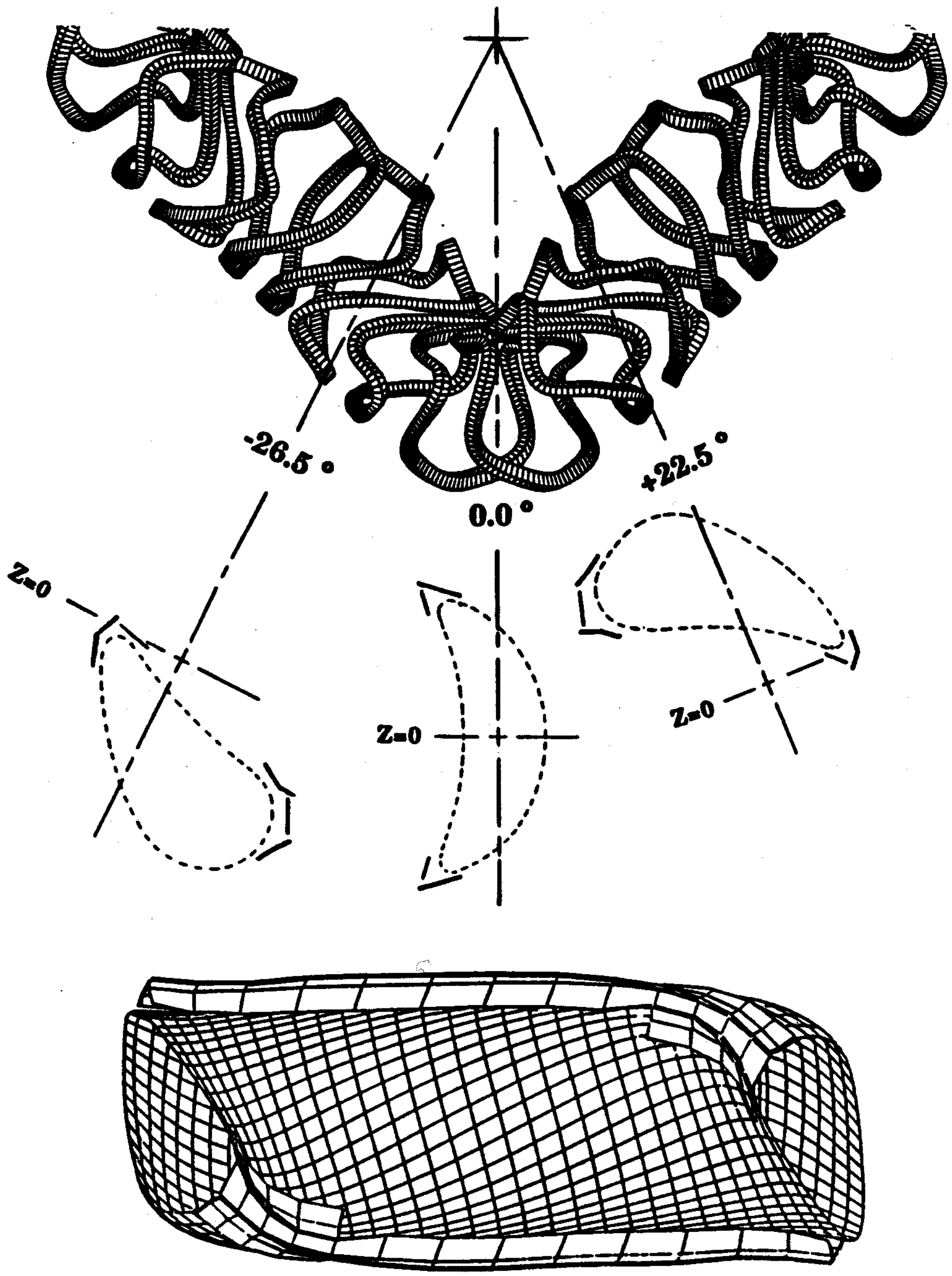

Figure 5.4-11. View of one half of the SPPS coil set, the plasma contours at -26.5°, 0° and +22.5°, and a 3D front view of the last MHD stable flux surface showing location of divertor plates.

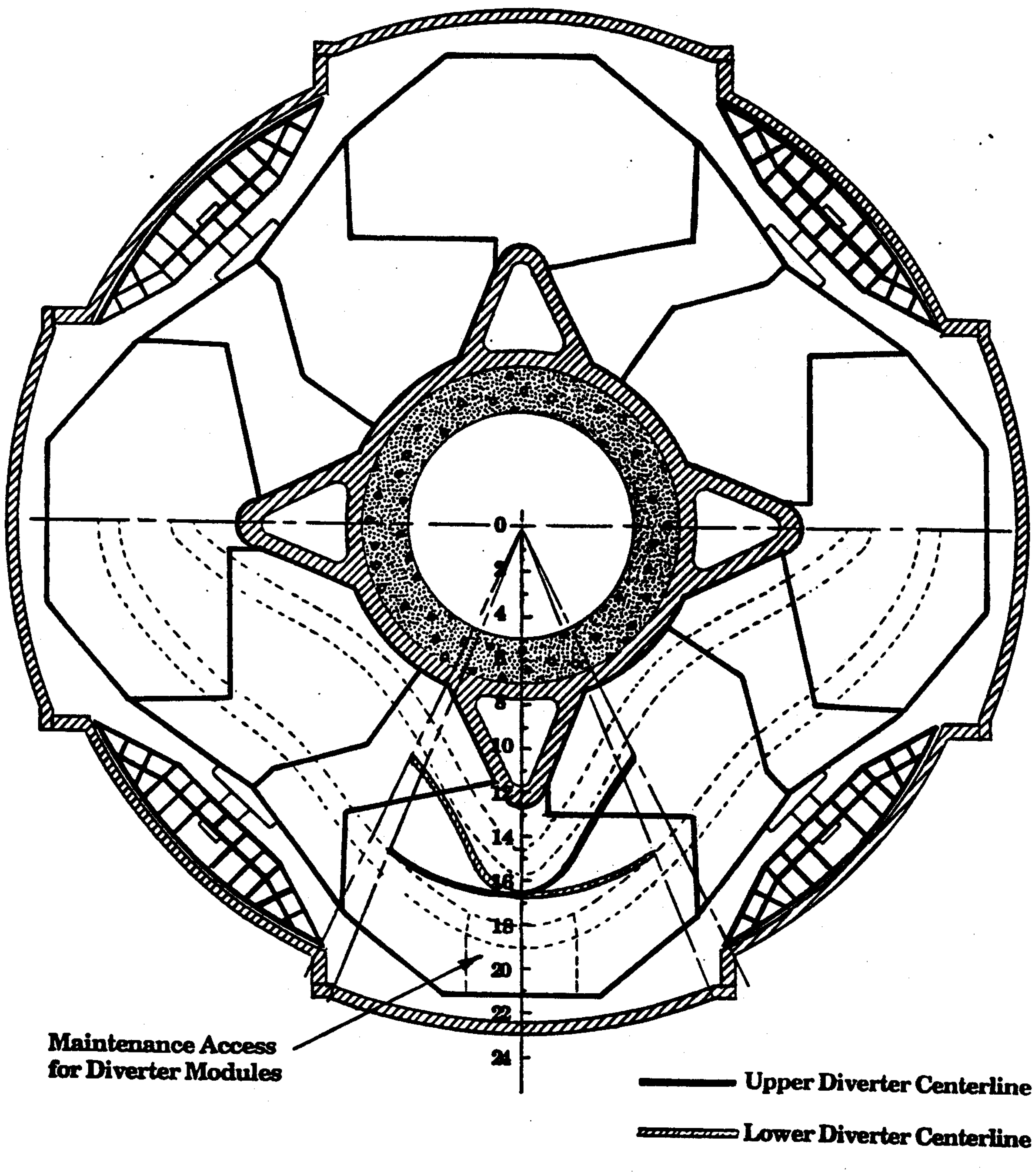

Figure 5.4-12. Top view of the SPPS showing the extent of divertor plate coverage.

extends from -22.5° to +26.5° while the lower divertor from -26.5° to +22.5°. What is immediately evident from these figures is that the divertor is entirely located inside the blanket modules which are within the corner cryostat. This is very fortunate, in that the divertors can be replaced simultaneously with the blanket modules. Alternatively, if the lifetime of the divertor plates is shorter than that of the first wall and blanket, then another scheme has been devised for their maintenance, as described in Sec. 5.4.6.2.

5.4.4. Cryostats Configuration

The cryostats insure that the superconducting coils are maintained near liquid He temperature and create the barrier between the cold coils and the hot blanket/shield components. The coils themselves are cooled with liquid He which is pumped through passages in the conductors. On the outside of the coil cases, aluminized mylar multi-layer superinsulation is wrapped which cuts down on radiative losses, while conductive and convective losses are eliminated by evacuating the cryostats. The walls of the cryostats have to be able to withstand one atmosphere of pressure during the testing phase. Inside the vacuum chamber during plant operation, there is no atmospheric load on the walls. However, the cryostat walls must be capable of transmitting forces from the coils to external structure located in the vacuum chamber. To minimize the heat conducted through this structure, there will be liquid N_2 cooled intercepts located on the supports. Thus, the only heat conducted to the coils would be that driven by the temperature difference of 77 K to 4.2 K along the supports.

As mentioned above, the stellarator coils are distributed in the various cryostats unevenly. There are four coils in each corner cryostat and two coils each in the remaining cryostats (seeFigure 5.4-13). Note that some of the coils appear to be sharing adjacent cryostats. That is not the case at all. The heavy lines outline the upper cryostat surfaces, however, these lines do not connect the top and bottom cryostat surfaces with vertical surfaces, but are inclined to accommodate some of the coils' excursions. These excursions entail a coil part going over an adjacent coil or conversely, going beneath an adjacent coil part. The inter-cryostat surfaces follow these excursions such that the coils are always within their designated cryostat. For this reason, if Fig. 5.4-13 was viewed from the bottom, the outline of the two cryostats between the corner cryostats would switch places. The one important aspect of the cryostats design, is that the inter-cryostat surfaces will not prevent maintenance of the fusion core by moving cryostats. Thus, corner cryostats can be taken out radially through the vacuum chamber ports, and the cryostats adjacent to them, can be taken out diagonally through the same ports.

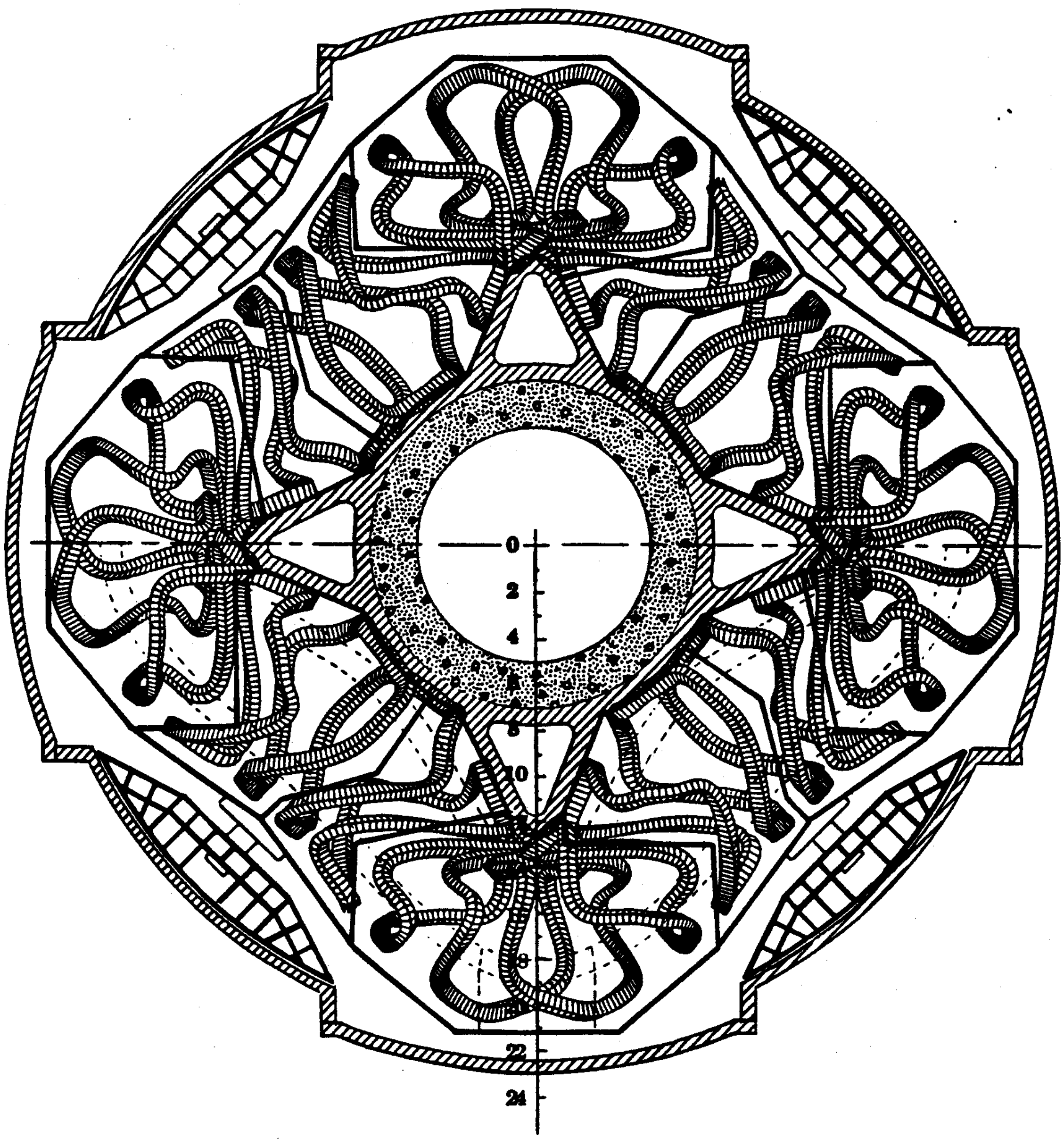

Figure 5.4-13. Top view of the SPPS showing coil locations in the cryostats.

5.4.5. Structural Distribution

This is a brief discussion of the structure distribution in the fusion power core. It should be made clear that this is not a structural analysis by any means, rather it is an attempt to determine where structure will be needed; get a first order appreciation for how much is needed: finally, to determine if the structure can be placed in such a way that it will not interfere with normal maintenance of the fusion core.

Figure 5.4-14 is a top view of one half of the fusion core with an overlay of the force vectors in the $X-Y$ plane as applied to the centroid of each coil. This is the resultant of the integrated forces around the coil in the $X-Y$ plane. The coils are numbered from 25–32 and from 1–8. Figure 5.4-14 also gives the integrated vertical force vectors for each coil. Note that the largest forces in the $X--Y$ plane are on coils 25, 32, 1 and 8, which are corner coils. The protrusions from the center-post at these locations are intended to react these forces. Some components of these forces will be reacted with intercoil support structure. The next largest $X-Y$ forces are on coils 26, 31, 2 and 7, which are also corner coils. Here again the main thrust will be against the center-post protrusions with small intercoil components. The $X-Y$ forces on coils 27–30 and 3–6 have no radial components and, therefore, will not be reacted by the center-post. Rather, these vectors will have force components which will have to be reacted with intercoil structure and structure on the outboard side. This outboard side structure is shown in Figs. 5.4-13 and 5.4-14 as filling the space between access ports in the vacuum chamber. A piston is shown as bridging the space between the structure and the cryostat, implying an adjustable mechanism. Such a mechanism is needed for two reasons: the mechanism must be capable of being retracted to make room for the extraction of these cryostats should that become necessary, and adjustments will be needed for coil location and force reaction when the coils are energized.

Figure 5.4-14 also shows the vertical force vectors on the coils. These forces will be reacted with over-the-top and under-the-bottom structure connecting with the outboard side structure and the center-port structure. The over-the-top and under-the-bottom structure also will need adjustable piston type mechanisms for the same reasons as the outboard side structure.

The picture which emerges is that of a set of coils encased in a cocoon of structure on all sides with the exception of the area in front of the access ports. Figure 5.4-15 is a CAD generated picture of this cocoon of structure with the fusion core removed altogether. What appears to be a double roof is a structure which derives stiffness from an H-beam type of configuration. Table 5.4-I gives the magnitude of the integrated force

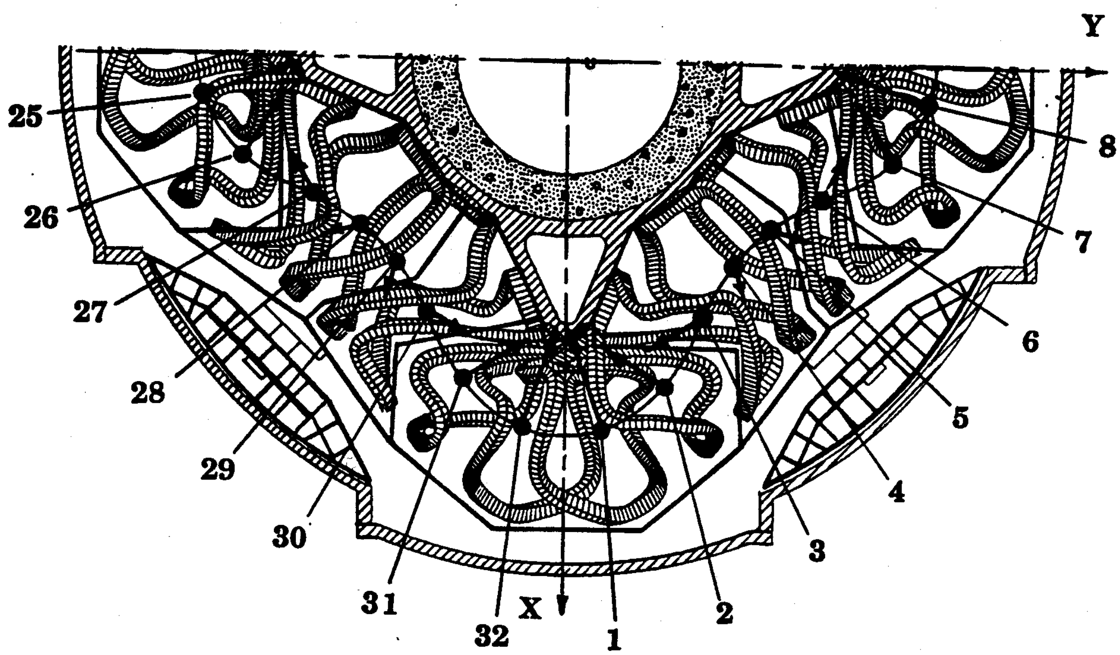

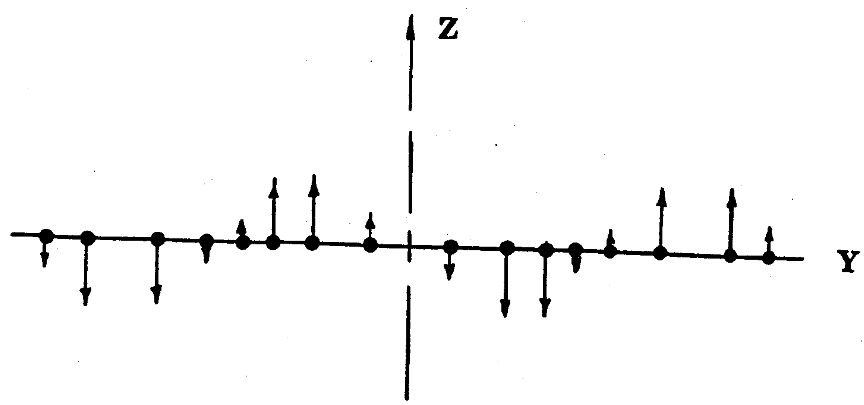

Figure 5.4-14. Top view of one half of the SPPS showing the X and Y force vectors integrated around the circumference and applied at the near coil centroids. Integrated vertical force (Z) vectors from coils are also shown.

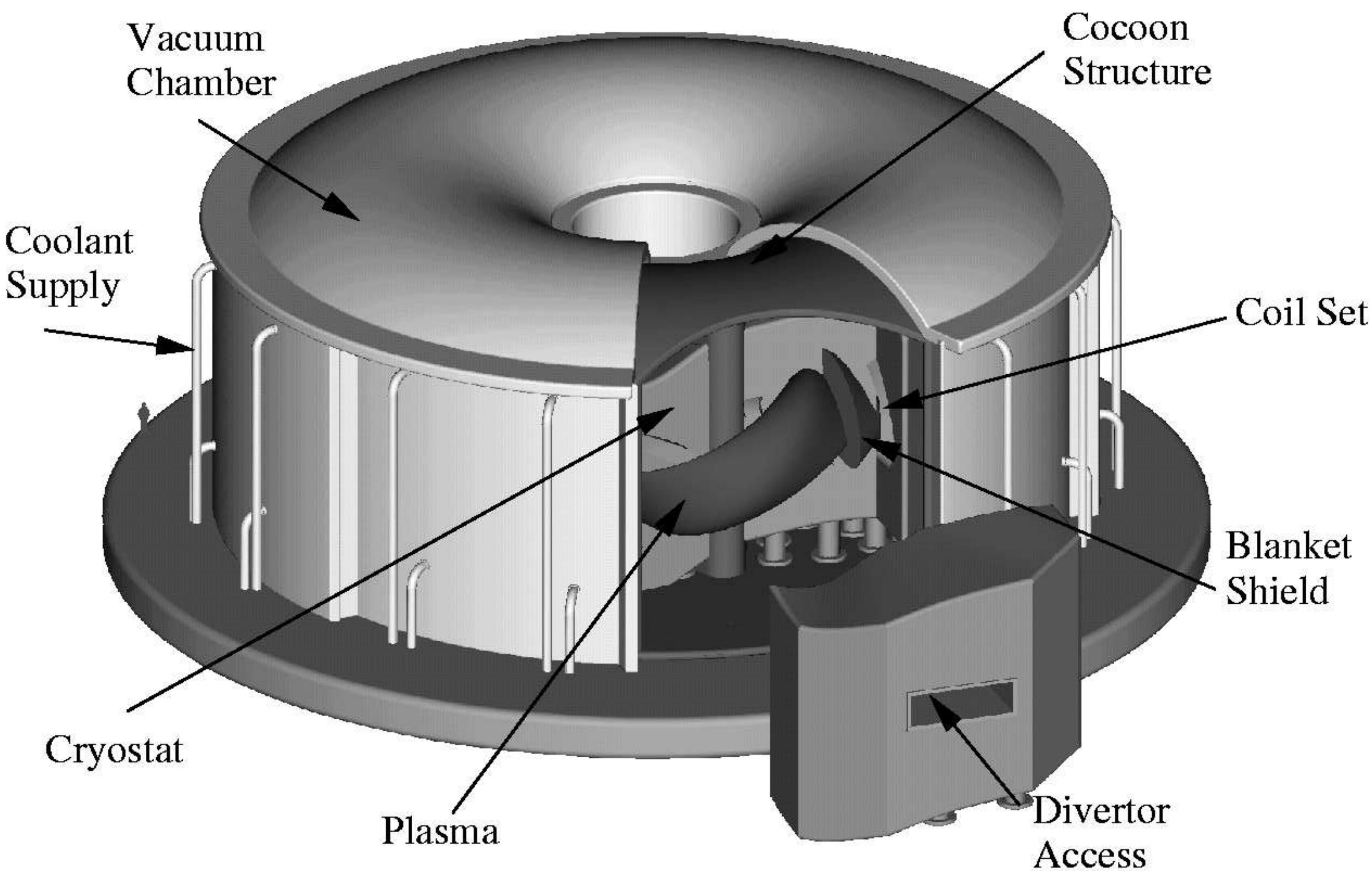

Figure 5.4-15. Isometric view of the SPPS Fusion Power Core showing the structural cocoon.

Table 5.4-I.
Force Vectors on SPPS Coils

Coil	F_X (MN)	F_Y (MN)	F_Z (MN)	F_{XY} (MN)	Angle	F_{Res} (MN)
25	-109.9	316.6	-103.3	335.2	109°	350
26	-205.9	129.7	-225.3	243.4	149°	332
27	-133.9	-79.9	-212.5	156.0	-149°	264
28	34.3	-128.0	-68.9	132.5	-75°	149
29	128.0	-34.3	68.9	132.5	-15°	149
30	79.9	133.9	212.5	156.0	59°	264
31	-129.7	205.9	225.3	243.4	122°	332
32	-316.6	109.9	103.3	335.2	161°	350
1	-316.6	-109.9	-103.3	335.2	-161°	350
2	-129.7	-205.9	-225.3	243.4	-122°	332
3	79.9	-133.9	-212.5	156.0	-59°	264
4	128.0	34.3	-68.9	132.5	15°	149
5	34.3	128.0	68.9	132.5	75°	149
6	-133.9	79.9	212.5	156.0	149°	264
7	-205.9	-129.7	225.3	243.4	-149°	332
8	-109.9	-316.6	103.3	335.2	-109°	350

vector components for the coils shown in Fig. 5.4-14. The angles of the $X-Y$ vectors are measured counter clockwise from the vertical line parallel to the X-axis going through the centroid of each coil, with 0° taken on the outboard side. A negative angle indicates a clockwise measurement. The vectors F_X, F_Y and $F(Z)$ change signs from 25–32 and 1–8, and F_X and F_Y sometimes alternate both sign and magnitude. However F_{XY} remains the same for similar coils, and the resultant force F_{Res}, which is the vector summation of F_{XY} and F_Z is also the same for similar coils.

Material properties used in support structure calculations are given in Table 5.4-II. Most of the support structure in the coils cocoon will be at a temperature below 473 K and for this reason the yield strength for 20% cold worked 316 SS at 473 K is used. The design stress is taken as 2/3 of the yield strength, or 446 MPa. No distinction is made between structure at 473 K or at 20 K, and since stainless steel becomes stronger at cryogenic temperatures, these estimates of mass of the structure will be conservative.

Table 5.4-II.
Material Properties Used in Support Structure Calculations

Material	316 SS cold worked
Average ultimate strength	745 MPa at 473 K
Average yield strength	670 MPa at 473 K
Modulus of elasticity	1.94×10^5 MPa
Poisson's ratio	0.3
Design stress	446 MPa at 473 K

5.4.5.1. Center post structure

The formula for a ring under several equal radial forces, equally spaced, is used for calculating the amount of structure in the center post. The bending moments for this case are [28]:

$$M(+) = \frac{WR}{2}\left(\frac{1}{S} - \frac{1}{\theta}\right), \tag{5.4-1}$$

$$M_{\max}(-) = -\frac{WR}{2}\left(\frac{1}{\theta} - \frac{C}{S}\right), \tag{5.4-2}$$

where W is the applied load, R the radius, θ is the half angle between loads, S the sine of θ and C the cosine of θ. In this case $W = 893$ MN, $R = 7.5$ m, $\theta = 45°$, $S = 0.707$ and $C = 0.707$.

The maximum bending moment occurs at the point of load application and is equal to 916 MNm, while the bending moment between loads is 470 MNm. For maintaining a stress of ∼440 MPa, the specific moment of inertia is 0.285 m^4/m which is equivalent to two tier depths of 0.76 m × 0.38 m H beams. The height of the center post over which the radial forces are applied is 4.56 m, thus requiring 12 levels of stacked beams. The total length of beams is 1,030 m at a weight of 254 kg/m, for a total mass of 262 tonnes.

In addition to the radial load, the center-post is subjected to a vertical tensile load from the F_Z forces on the coils. This load of 2,440 MN is shared between the center-post structure and the outboard structure, thus requiring an area of steel in tension of 2.65 m^2. The cumulative thickness of the flanges in the two tiers of H beams exceeds this area by more than a factor of two. The remaining part of the center-post, which amounts to another 9 m needs 2.65 m^2 in tension, requiring an additional mass of 179 tonnes. This makes the total mass of the center-post equal to 441 tonnes.

5.4.5.2. Outboard structure

Coils 28, 29 and 4, 5 have outward radial force components equal to $132.5\cos(15°) =$ 128 MN each. Assuming a build up of the same H beams used in the center-post, over a height of 14 m and a width of 6 m, the needed moment of inertia is 1.0 m^4. It is interesting to note that the mid-plane deflection of the structural assembly is 1.8 cm which can be corrected with the adjustable piston mechanism. The total outboard structural mass at all four locations is 488 tonnes.

5.4.5.3. Over the top and bottom structure

Figure 5.4-14 shows the vertical forces F_Z on the coils. The sum of the forces in each cycle, for example on coils 29–32, is 610 MN, and they are cyclic. Using the same methodology as in the previous section, the moments of inertia needed over a span of 11.0 m for coils 29, 30, 31 and 32 are 0.12 m^4, 0.71 m^4, 0.78 m^4 and 0.24 m^4 respectively, and the total amount of structure is 44 tonnes, 78 tonnes, 80 tonnes and 57 tonnes respectively. The deflections are from 1.2–1.8 cm. The total amount of structure to react the vertical force vectors is 4,144 tonnes.

5.4.5.4. Intercoil structure

Lacking the time or resources to perform an accurate determination of the intercoil support structure, it was necessary to resort to simplifying assumptions which were:

1. The coil cases for coils 31, 32, 1 and 2 overlap on the inboard mid-plane, requiring them to be integrated together at that point with no intercoil supports.
2. Intercoil supports are spaced at 2 m intervals along the whole circumference of the coils to react the force component vectors along the locus of the coil centroids, as shown in Fig. 5.4-14.
3. Check for buckling of support structure at points where the coils legs are far apart.
4. Assume that the intercoil supports will be adjustable in length.

It is important to insure that the coil deflection between supports spaced at 2 m will not be excessive. From Fig. 5.4-14 and Table 5.4-I, it can be seen that the largest intercoil force occurs between coils 30 and 31, and others of the same configuration around the torus. The force component directed along the locus of the coils' centroid for coil 30 is 125 MN. Typically, the magnetic force density from the front to the back of the coils varies by a factor of three, and it is safe to assume that the intercoil forces would do the same. This means that the force on the coil will vary from 10 MN/m at the front to 3.3 MN/m at the back. The coil case thickness in this design is 7.5 cm, the conductor bundle 0.51 m $\times$ 0.789 m, therefore the coil case outer dimensions are 0.66 m $\times$ 0.93 m. The moment of inertia of the coil case by itself is 0.0137 m^4 for bending about an axis parallel to the large dimension. To calculate the coil leg deflection between supports spaced at 2 m, a built-in beam of the above moment of inertial loaded uniformly with 10 MN/m is assumed. The equation is [28]:

$$y = \frac{W\ell^4}{384\,E\,I}\,, \tag{5.4-3}$$

where y is the deflection, W is the load per unit length, ℓ the distance between supports, E the modulus of elasticity and I the moment of inertia. The deflection is 1.5×10^{-4} m or 150μm, a negligible value. The shortening of the intercoil support structure itself under load must also be taken into account. Because the distances between coil legs are sometimes as long as 8 m, the structure provided in compression will become shorter even under very low stress. For example, if the stress is only 50 MPa, an 8 m long support rod will be reduced in length by 2.0 mm, and at a more reasonable stress of 500 MPa it will be reduced by 2 cm. If the accuracy of the conductor bundle location must be maintained to 10^{-4} m/m, this means that the deflection of an 8 m long support can not be more than 0.8 mm implying that the stress in the support rod can only be 20 MPa, requiring an inordinately large amount of structure. This is clearly unreasonable. Furthermore, the shrinkage of steel from room to cryogenic temperatures must also be reckoned with, exacerbating the problem even more. An obvious solution would be to make these long intercoil support rods adjustable. There are several ways for accomplishing this, but will not be a part of this study. For the present, these long intercoil supports are assumed to be adjustable. Using the method described above for spacing intercoil structure, it has been estimated that 7.7 tonnes will be required between each coil in the corner cryostats. Using a 30% safety factor the total amount of structure in the corner cryostats is 30 tonnes. Similarly, the total amount of intercoil structure is determined to be 240 tonnes.

Table 5.4-III summarizes the estimated structure which supports the magnetic forces on the coils. This structural evaluation can be compared with other estimates made for similar coil systems by using the virial stress, which very simply is the ratio of the stored energy to the volume of structure used to contain it. If one obtains the virial stress for the conductor volume alone, using the stored energy of 78 GJ and a volume of 400 m^3, it is 195 MPa. This value for some of the Helias design designated HSR58 [29] varies from 110–130 MPa. The virial stress for the case where all the structure is included is 59 MPa for SPPS and varies from 41–44 MPa for the HSR58 systems. It is interesting to note that if the assumption of adjustable intercoil supports was not made, the added structure would have brought the virial stress closer to the values for the HSR58 system.

Table 5.4-III.
Mass of SPPS Magnets Support Structures (tonnes)

Coil cases	1,651
Center-post	441
Top and bottom	4,144
Outboard	488
Intercoil	240
Total	5313

5.4.6. Fusion-Core Maintenance

As mentioned in the introduction, this report will deal with three aspects of fusion-core maintenance, namely the blanket/shield, the divertor elements and the coils. Further, this treatise will be rudimentary in the sense that it cannot go into great detail. Rather, a gross assessment of the feasibility is made consistent with the scope of the study.

The maintenance of the SPPS components depends on the capability to move the corner cryostats containing the four corner coils. For this reason the vacuum chamber was designed to have access ports behind the corner cryostats. Further, the support structure has been arranged in such a way as to leave the access ports unobstructed. In the following sections the maintenance procedures for the blanket/shield components, the divertor components, and the coils is described.

5.4.6.1. Maintenance of the Blanket/Shield Components

Radiation damage in the first wall and blanket components necessitates their periodic replacement. The peak neutron wall loading is 2 MW/m^2 which means the maximum first wall fluence will reach 15 MW a/m^2 in 7.7 full power years (FPY) or, at 70% availability, 11 calendar years. This means that the first wall, blanket and replaceable shield will be replaced on an 11 year schedule. One possible scenario is to replace 25% of these components every 33 months. Such a scheme would work out very well, since 25% of the components can be replaced by moving one of the corner cryostats.

Figure 5.4-16 is a top view of the fusion core with a corner cryostat extracted through a vacuum vessel access port and Fig. 5.4-17 shows several views of a free standing corner cryostat. There are six blanket/shield modules that come out with the corner cryostat. According to the numeration in Fig. 5.4-9 they are modules 42–44 and 1–3. These modules are now accessible for extraction through the open ends of the cryostat. Further, the modules adjacent to the corner cryostat, namely 39–41 and 4–6 are also accessible through the openings in the cryostats which are still in the vacuum vessel. Thus, 25% of the blanket/shield modules become accessible for replacement by virtue of the extraction of one corner cryostat. It is well and good to say the modules become accessible for extraction, but how they can be extracted is still an issue. This will be addressed in the next sections.

Figure 5.4-10 shows the top and side views of modules 1, 2 and 3. The complimentary modules 42, 43 and 44 are identical but are twisting in the opposite direction. Modules 42, 43, 2 and 3 protrude from the corner cryostat, and thus are not contained on their total perimeter. Extracting them should be fairly straight forward. On the other hand, modules 44 and 1 are contained around their perimeter and extracting them through a somewhat changing aperture of the cryostat will be difficult. Fortunately, the divertor access port located at the outboard mid-plane of the corner cryostat as shown in Fig. 5.4-9 will help out in this case. As shown in the figure, the outboard mid-plane portions of the blanket/shield of modules 44 and 1 are attached to the access port and can be withdrawn radially from the cryostat. This relieves the rear constraint on these modules and makes it possible for them to be extracted. The effect on modules 44 and 1 is that their outboard mid-plane segment is missing as shown in Fig. 5.4-18. However, assembled in the fusion core with the divertor access port in place, these modules are reconstituted.

Turning to modules 4, 5, 6 and 39, 40, 41, which are within the adjacent cryostats still inside the vacuum chamber, it can be seen that modules 4 and 41 protrude from the cryostats somewhat and are contained over a small fraction of their outboard perimeter. From a cursory inspection it appears that they can be extracted with a minimum amount of manipulation. The remaining modules 5, 6, 39 and 40 are trapped well within their respective cryostats and cannot be extracted easily. There are three solutions to this problem:

1. Provide a larger gap between the replaceable blanket/shield for all the modules within these adjacent cryostats.

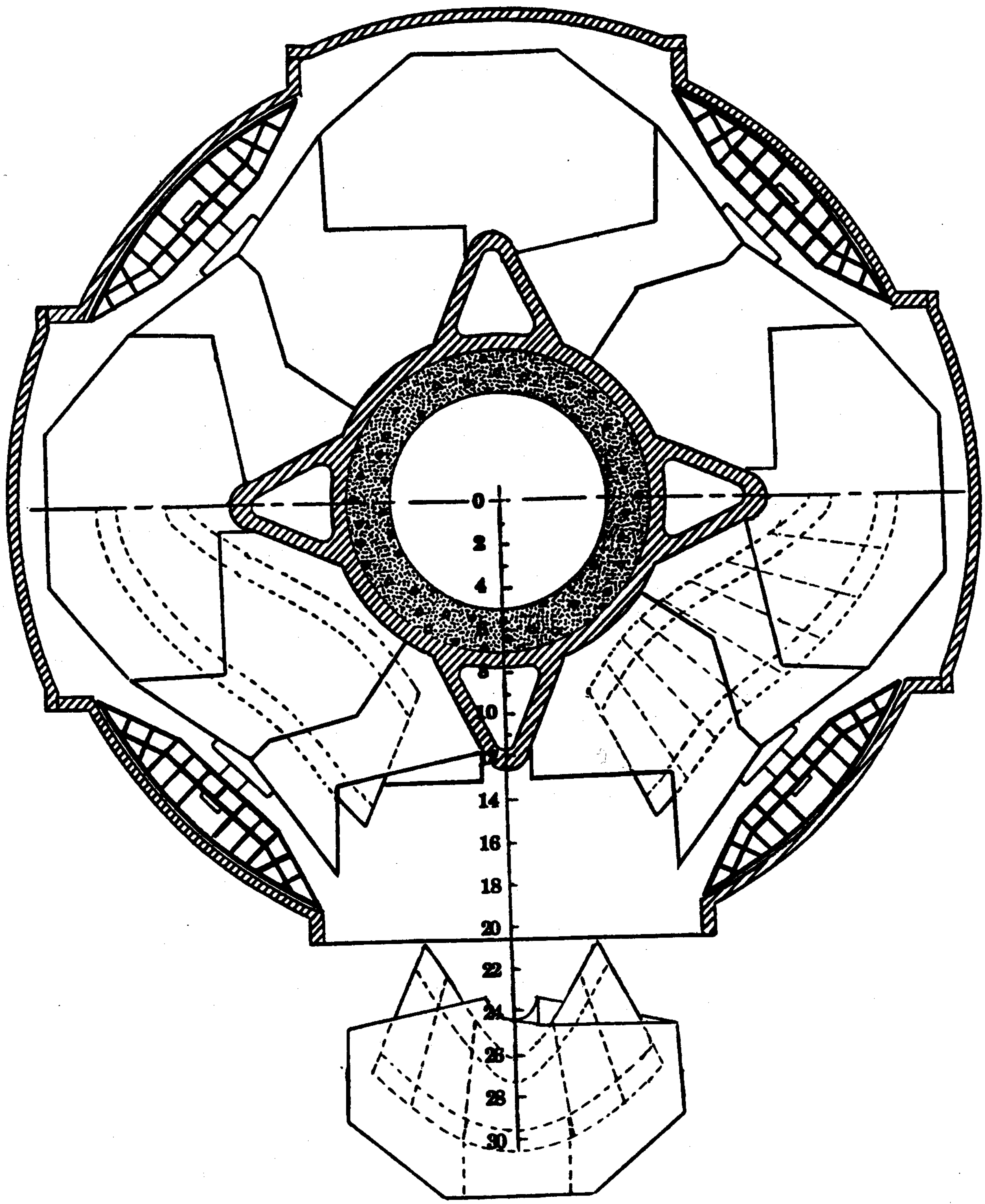

Figure 5.4-16. Corner cryostat shown extracted from vacuum vessel.

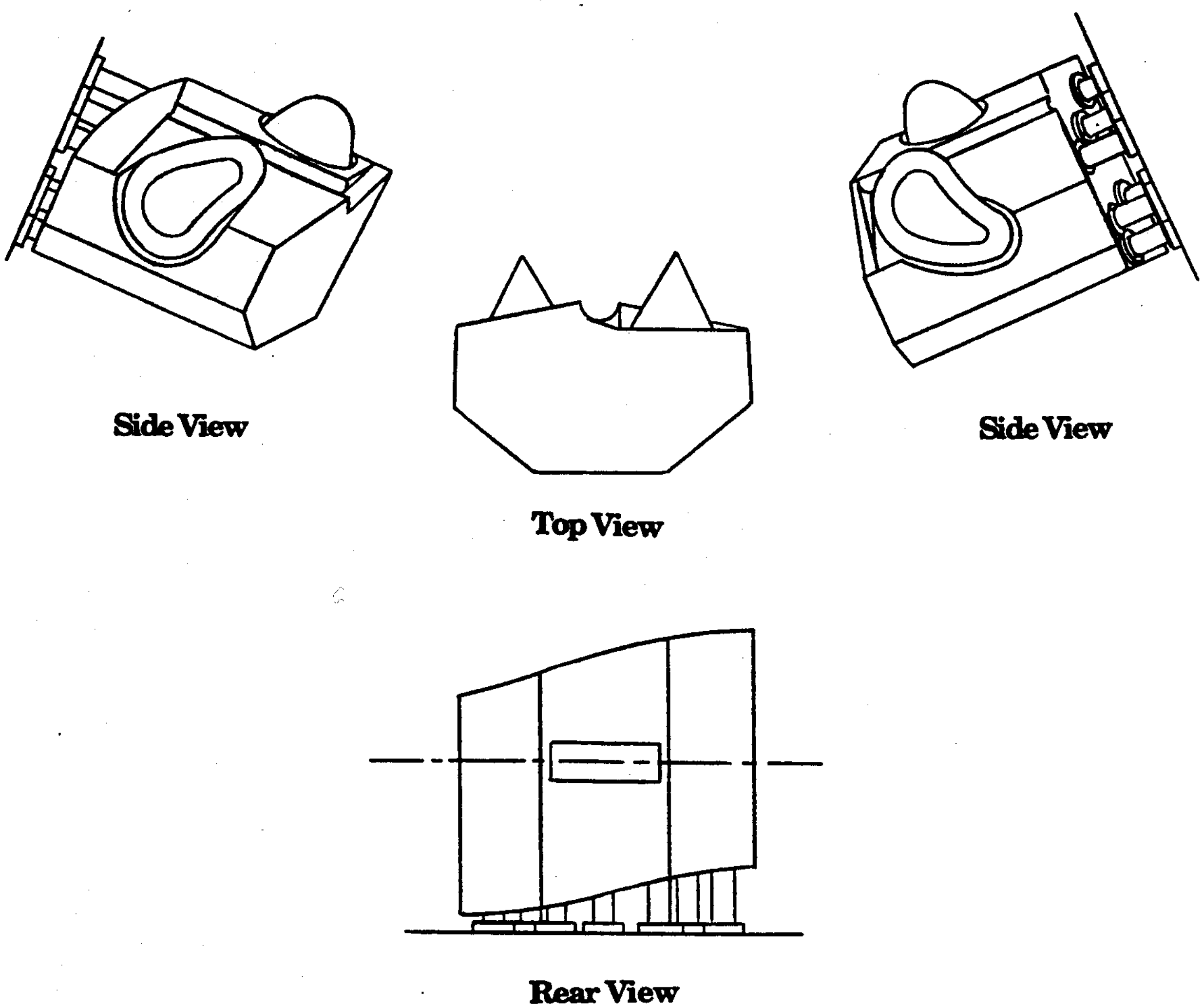

Figure 5.4-17. Several views of a free standing corner cryostat.

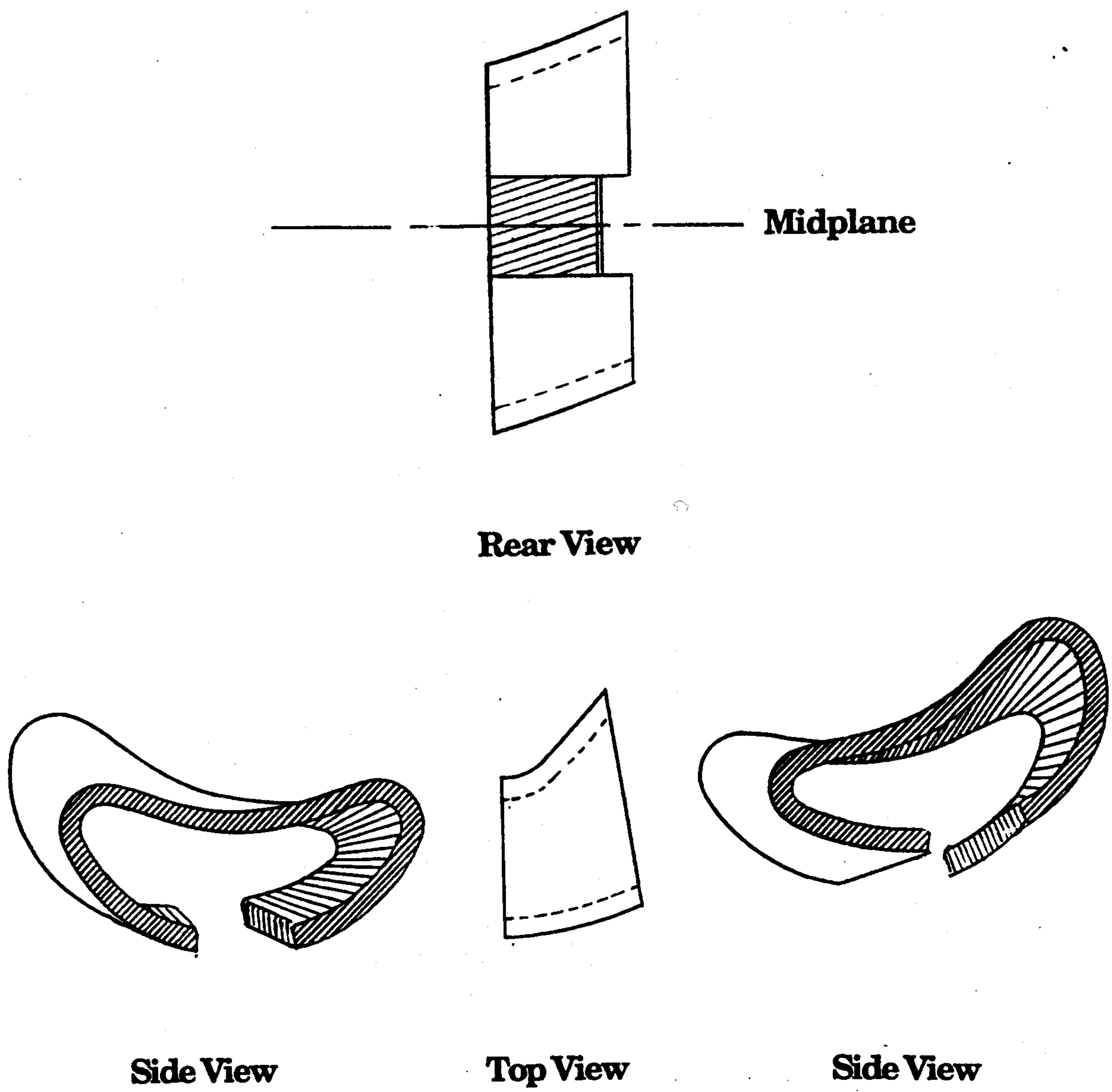

Figure 5.4-18. Blanket/shield module no. 1 shown with outer mid-plane part removed.

2. Move the adjacent cryostats out of the vacuum chamber.
3. Divide modules 5, 6, 39 and 40 into two parts along an inclined plane passing vertically through them.

The first option compromises shielding and will require a redesign of the fusion core with larger coils; not a desirable solution. The second option is certainly possible, since the fusion-core design has provided for the capability of extracting these adjacent cryostats from the vacuum vessel. However, moving cryostats is a slow and tedious operation to be resorted to only if all other options fail. The last option is the least intrusive and will require the least amount of modification. Dividing these modules into two halves by passing vertical planes inclined several degrees from the centerline through them will make it possible to extract each half separately. The major penalty is that an additional set of coolant lines needs to be disconnected, and seems to be a small price to pay for this convenience.

Thus far, the overall processes needed for blanket/shield replacement have been summarized. In this section a step-by-step description of the tasks will be given. The initial conditions are that the plasma has been shut down, and the coolant continued to be circulated for a period of time to dissipate the afterheat generated by the short term activation products. The subsequent steps are as follows:

1. The magnets are de-energized but maintained cold by not despoiling the vacuum within the cryostats.
2. The lithium coolant is drained into dump tanks.
3. The vacuum chamber is brought up to one atmosphere of pressure with dry air. Alternatively, if the containment building in which the vacuum vessel is situated is capable of being sealed, then the cover gas could be He or dry N_2.
4. The designated access port to the vacuum vessel is unbolted and the door removed.
5. Any over-the-top and under-the-bottom load activators designated for the particular corner cryostat in question are de-energized.
6. Coolant connections joining the blanket/shield modules to external headers are disconnected.
7. Cryogenic coolant lines are disconnected and capped off, and electric bus-bars are disconnected.

8. Rails or guided runners for gas pads are located through the access port and fixed to the floor.

9. Compressors for activating the gas pads are connected and turned on.

10. A mobile robot is attached to the undercarriage of the corner cryostat which pulls out the cryostat on guided runways radially from the vacuum vessel. The cryostat is moved a sufficient distance as to allow roving remote handling machines to service the blanket/shield modules both within the corner cryostat and within the vacuum vessel.

After the old blanket/shield modules are replaced with new ones, and are checked for leak tightness, the process is reversed, the fusion core reassembled and prepared for start-up.

As mentioned before, moving the corner cryostat is no trivial task. Aside from its mass, which is ~2,215 tonnes, this is a very delicate and precise operation. Returning the cryostat back into the vacuum vessel is even more crucial, since the location of the coils must be within a tolerance of 10^{-4} m/m. This is the reason that adjustable support structure both intercoil and otherwise is necessary. Precise mechanical location can be performed with the use of fiducial marks and advanced optical measuring instruments. However, final adjustments must be made after the system is evacuated and the coils energized. Fortunately, in stellarators, vacuum fields can be established and precisely measured, before a plasma is launched.

Table 5.4-IV lists the masses in corner cryostats and Table 5.4-V gives the physical parameters of the blanket/shields as numbered from 1–6. Please note that module 7 is identical to 5 and 8 identical to 4, *etc.* There are volume and mass values for the so called "hot shield" which is replaced along with the blanket, and there are values for the "cold shield" which is a lifetime component. The masses given for the first wall, blanket and shield are with the lithium coolant drained out.

During blanket replacement it is the masses of the first wall, blanket and the hot shield which are replaced. For modules 1, 2 and 3 this is 155.6 tonnes, 151.3 tonnes and 135.3 tonnes respectively. However, since module 1 has ~ 15% of it removed with the divertor access port, this makes its mass 132.3 tonnes. This means that the heaviest module is 2 at 151.3 tonnes, and the lightest is at 86.4 tonnes. Module 2 is one of the easier ones to extract, since it protrudes from the cryostat and is constrained only at its outboard perimeter. An overheat crane assisted with ground mounted manipulators will be able to perform the operation. An overhead crane will not be able to assist in

Table 5.4-IV.
Masses in Corner Cryostat (tonnes)

Coils	513
Intercoil structure	30
Blanket/shield	1,486
Cryostat	186
Total	2,215

Table 5.4-V.
Physical Parameters of SPPS Blanket Modules

Module no.:	1	2	3	4	5	6
First wall surface area (m^2)	37.31	36.47	32.43	27.70	21.88	21.05
First wall volume (m^3)	0.522	0.511	0.454	0.388	0.306	0.295
Blanket volume (m^3)	13.06	12.76	11.35	9.70	7.66	7.37
First wall & blanket mass$^{(a)}$ (tonnes)	8.922	8.719	7.754	6.624	5.23	5.033
Hot shield volume (m^3)	20.5	19.93	17.82	14.36	11.89	11.37
Hot shield mass$^{(a)}$ Li (tonnes)	146.68	142.60	127.5	102.71	85.10	81.37
Cold shield volume (m^3)	14.27	13.95	12.40	10.30	8.35	8.03
Cold shield mass$^{(a)}$ (tonnes)	105.74	103.37	91.88	76.29	61.90	59.49

(a) Without the Li coolant.

the replacement of modules 39-41 and 4-6 due to the overhang of the structural cocoon and the roof of the vacuum vessel. They will be entirely handled with ground mounted manipulators working inside the vacuum vessel.

5.4.6.2. Maintenance of Divertor Plates

The divertor plates suffer radiation damage at the same rate as the first wall elements and their radiation damage lifetime will be the same. However, these plates will be subjected to high particle fluxes, and depending on the particle energies, can sustain high rates of erosion. Further, because they will be high heat flux components, they are more vulnerable to failure than the first wall. For this reason, a mechanism for accessing the divertor plates for replacement, without moving any cryostats has been devised.

Figure 5.4-9 shows a top view of the fusion core with the vacuum vessel and over the top structure removed. The corner cryostat lying along the X axis has dotted lines outlining an access port on its outer perimeter. Figure 5.4-17 has several views of the corner cryostat, and the rear view shows an access port at the mid-plane. It is possible to locate an access port there, because the backlegs of the coils at that point are almost 8 m apart. The flange shown in Fig. 5.4-17 is attached to effectively a drawer reaching through the walls of the cryostat all the way to the blanket/shield. The cavity through which this drawer penetrates is totally enclosed such that the vacuum in the cryostat is unaffected. Withdrawing this drawer from the cryostat extracts with it that portion of the blanket/shield attached to it which is part of module 44 and 1. The aperture which is created this way is 5 m in the horizontal direction and 1.8 m in the vertical direction. Rails can be inserted into this port on which special remote handling machine can enter into the plasma chamber to disconnect and remove divertor segments.

It is conceivable that this operation can be performed through the vacuum vessel access port door using an airlock, such that the vacuum vessel can stay evacuated. This would enhance the process, however, at the expense of the complication of using an airlock.

5.4.6.3. Maintenance of Coils

The coils in SPPS are lifetime components and should not have to be replaced. However, should there be coil malfunction, a problem with intercoil structure, a cryogenic leak or a cryostat vacuum leak, it would be necessary to be able to get at all ports of the cryostats for repair or replacement. For this reason, the vacuum vessel and the support structure has been designed with the capability of extracting all of the cryostats.

Figure 5.4-16 shows how a corner cryostat is extracted and Fig. 5.4-19 shows how an adjacent cryostat is extracted. The adjacent cryostat on the other side can be extracted in the same way. The other three vacuum vessel ports can be used to access all of the other cryostats providing the capability of maintaining all the coils in the fusion core.

5.5. SUMMARY AND CONCLUSIONS

The SPPS reference blanket design is a liquid metal blanket with lithium as coolant and breeder and vanadium alloys as structural material. It also assumed that a suitable insulating coating (*e.g.,* CaO) can be developed to significantly reduce the MHD pressure drops. The use of the insulating coating has major impacts on the configuration as it allows one to develop an attractive first wall and blanket design by addressing mechanical, thermal hydraulic, and neutronics requirements in the most direct and simple way rather than by trying to minimize MHD pressure drop effects by utilizing more complex flow configurations. Because of high exit temperature of the coolant, an advanced Rankine cycle with an efficiency of 46% has been utilized.

The 35 cm thick blanket will provide tritium self-sufficiency for the SPPS stellarator design. An overall tritium breeding ratio of 1.12 seems adequate with provisions made for the presence of penetrations and divertor plates. The first wall and blanket should be replaced every 11 y due to radiation damage to the vanadium structure. Sufficient shield is placed behind the blanket to protect the magnets. For a peak neutron wall loading of 2 MW/m^2, the shield is 80 cm thick and is made of borated steel filler supported by V structure. A successful attempt was made to lower the cost of the shield while keeping the attractive safety feature of the design. A potential improvement to the present design is to employ the more efficient WC shield in the critical areas underneath magnets in order to reduce the radial standoff and thus the overall dimensions of the machine.

The unique advantage of the stellarator is that it can operate with a current-less plasma, thus avoiding the whole issue of disruptions. It does this by having all the current carrying elements external to the plasma which in turn complicates the coils required for confining the plasma. This coil system makes access to the fusion core components which need periodic replacement due to radiation damage more challenging. Power-plant designers working on modular stellarators have come to recognize early on that the only way to provide access for replacing first wall, blanket and shield components,

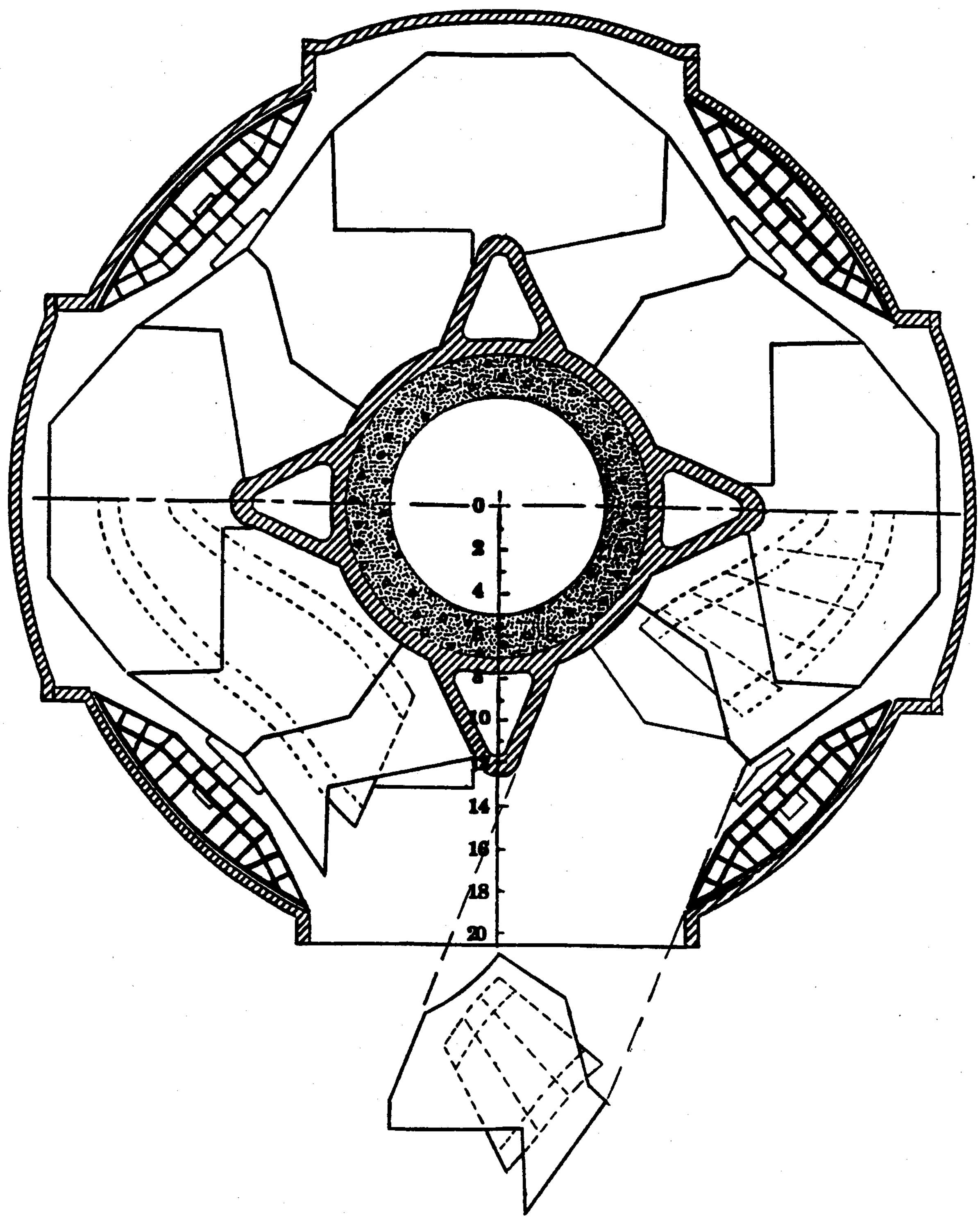

Figure 5.4-19. Top view of SPPS showing adjacent cryostat extracted from vacuum vessel.

and for maintaining the coils is by moving blocks of coils out of the fusion core enclosure. The best way for accomplishing this task is left to the innovativeness of the power-plant designers.

For SPPS, it has been determined that 16 of the 32 coils have to be displaced to provide maintenance capability for all the fusion core components. The coils are housed in discrete cryostats, four in corner cryostats and two in each adjacent one. The whole assembly of cryostats is surrounded with a cocoon of support structure and placed within the vacuum vessel. The vacuum vessel has four access ports located behind each of the corner cryostats and unobstructed by support structure. Adjustable pistons are used for transferring loads from the coils to the structure and for coil alignment. Extracting one corner cryostat through a vacuum vessel port provides access for maintaining 25% of the internal plasma chamber components which are divided into 44 modules, with the heaviest one weighing ∼150 tonnes. Because there are no seals between adjacent blanket/shield modules, the plasma chamber vacuum is shared with that of the vacuum vessel. An access port in the rear of the corner cryostat provides an opening for maintaining divertor segments independently from the blanket/shield modules. Finally, a capability is provided for extracting all the cryostats from the vacuum vessel in the event of a coil failure or a failure of any component within any of the cryostats.

REFERENCES

[1] C. Baker *et al.*, "Tokamak Power Systems Studies, FY 1985," Argonne National Laboratory report ANL/DPP-85-2 (December 1985).

[2] B. F. Picologlou, "Magnetohydrodynamics Considerations for the Design of Self-cooled Liquid Metal Fusion Reactor Blankets," *Fusion Technol.,* **8** No. 1, Part 2A (1985) 276- 282.

[3] D. K. Sze, R. F. Mattas, A. B. Hull, B. Picologlou, and D. L. Smith, "MHD Considerations for a Self-cooled Liquid Lithium Blanket," *Proc. of ANS 10th Top. Mtg. Technol. of Fusion Energy,* Boston, MA (June 1992), *Fusion Technol.* **21** (1992) 2099.

[4] J. H. Park, T. Domenico, G. Dragel, and R. W. Clark, "Development of Electrical Insulating Coatings for Fusion Power Applications," *Proc. of 3nd Int. Symp. Fusion Nucl. Technology (ISFNT),* Los Angeles, CA (June 1994), *ISFNT-3*, M. Abdou, M. S. Tillack, S. Tanka, P. J. Gierszewski, and A. R. Raffray, Eds., North-Holland, Amsterdam (1995).

[5] T. Q. Hua and Y. Gohar, "MHD Pressure Drops and Thermal Hydraulics Analysis for the ITER Breeding Blanket Design," *Fusion Eng. Des.,* **27** (1995) 696-702.

[6] L. Buhler and S. Molokov, "Magnetohydrodynamic Flows in Ducts with Insulating Coating," KfK report KfK-5103 (1993).

[7] R. N. Singh, "Compatibility of Ceramics with Liquid Na and Li," *J. Am. Cer. Soc.,* **59** (1975) 112.

[8] L. Barleon, K. J. Mack, R. Kirchner, M. Frank, and R. Stieglitz, "MHD Heat Transfer and Pressure Drop in Electrically Insulated Channels at Fusion Relevant Parameters," *Proc. 18th Symp. Fusion Technol. (SOFT),* Karlsruhe, Germany (Aug. 1994), *Fusion Technology 94*, K. Herschbach, W. Maurer, and J. E. Vetter, Eds., North-Holland, Amsterdam (1995) 1201.

[9] T. Q. Hua and B. F. Picologlou, "Heat Transfer in Rectangular First Wall Coolant Channels of Liquid-Metal-Cooled Blankets," *Proc. of ANS 8th Top. Mtg. Technol. of Fusion Energy,* Salt Lake City, UT (Oct. 1988), *Fusion Technol.* **15** (1989) 1174.

[10] D. L. Smith, *et al.,* "Blanket Comparison and Selection Study-Final Report," Argonne National Laboratory report ANL/FPP-84-1 (1984).

[11] V. A. Maroni, R. D. Wolson, and G. G. Staahl, "Some Preliminary Considerations of a Molten Salt Extraction Process to Remove Tritium from Liquid Lithium," *Nuclear Technol.,* **25** (1975) 83.

[12] S. D. Clinton and J. S. Watson, "Tritium Removal from Liquid Metals by Absorption in Tritium," *Proc. IEEE 7th Symp. on Eng. Prob. Fusion Res.,* Knoxville, TN, (October 25-28, 1977).

[13] R. E. Baxbaum, "The Use of Zirconium-Palladium Windows for the Separation of Deuterium from Dilute Solution in Lithium," *J. Phys. Chem.,* **79** (1973) 2386.

[14] E. Velekis and V. A. Maroni, "Thermodynamics Properties of Solutions of Hydrogen Isotopes in Metals and Alloys of Interest to Fusion Reactor Technology," Proc. Technology for Fusion Reactors, Gatlingburg, TN, (October 1975) 458-469.

[15] D. K. Sze, R. F. Mattas, J. L. Anderson, R. Haange, H. Yoshida and O. Kveton, "Tritium Recovery from Lithium, Based on Cold Trap," Tritium & Design **28** (1995) 220-225.

[16] O. Kveton, ITER Joint Central Team, Naka, Japan. Private Communication (1994).

[17] H. Attaya and M. Sawan, "NEWLIT – A General Code for Neutron Wall Loading Distribution in Toroidal Reactors," *Fusion Technol.,* **8** (1985) 608.

[18] M. A. Abdou *et al.,* "Deuterium-Tritium Fuel Self-Sufficiency in Fusion Reactors," *Fusion Technol.,* **9** (1986) 250.

[19] M. Z. Youssef and M. A. Abdou, "Uncertainties in Prediction of Tritium Breeding in Candidate Blanket Designs Due to Present Uncertainties in Nuclear Data Base," *Fusion Technol.,* **9** (1986) 286.

[20] M. Z. Youssef *et al.*, "The Prediction Capability for Tritium Production and Other Reaction Rates in Various Systems Configurations for a Series of the USDOE/JAERI Collaborative Fusion Blanket Experiments," *Fusion Eng. Des.,* **18** (1991) 407.

[21] R. O'Dell *et al.*, "User's Manual for ONEDANT: A Code Package for One-Dimensional, Diffusion Accelerated, Neutral Particle Transport," Los Alamos National Laboratory report LA-9184-M (1982).

[22] F. Najmabadi, R. W. Conn, *et al.*, "The ARIES-II and -IV Second-Stability Tokamak Fusion Power Plant Study—The Final Report," UCLA report UCLA-PPG-1461

(to be published); also, F. Najmabadi, R. W. Conn, *et al.*, "Directions for Attractive Tokamak Reactors: The ARIES-II and ARIES-IV Second-Stability Designs," *Proc. 14th Int. Conf. on Plasma Phys. and Controlled Nucl. Fusion Research,* Würzburg, Germany (Oct. 1992), International Atomic Energy Agency, Vienna (1993) 295.

[23] G. J. DeSalvo and R. W. Gorman, "ANSYS Engineering Analysis System Users Manual," Revision 5.0a, (December 1992), Swanson Analysis Systems, Inc.

[24] B. Badger *et al.*, "UWMAK-II, A Conceptual Tokamak Reactor Design," University of Wisconsin Fusion Technology Institute report UWFDM-112 (October 1975).

[25] C. C. Baker *et al.*, "STARFIRE–A Commercial Tokamak Fusion Power Plant Study," Argonne National Laboratory report ANL/FPP-80-1 (September 1980).

[26] W. R. Spears and R. Hancox, "A Pulsed Tokamak Reactor Study," UKAEA Culham Laboratory report CLM-R197 (1979).

[27] B. Badger *et al.*, "UWMAK-I, A Wisconsin Toroidal Fusion Reactor Design," University of Wisconsin Fusion Technology Institute report UWFDM-68 (November 1973).

[28] R. J. Roark and W. C. Young, *Formulas for Stress and Strain,* 5th Ed. McGraw-Hill Book Co. (1975).

[29] J. Junker (Ed.), "Proceedings of the 4th Workshop on WENDELSTEIN 7-X," Max-Planck-Institut für Plasmaphysik, Garching bei München, Schloss Ringberg, Bavaria (October 1991).